Simulation of a Hybridised Solar Gas Turbine System

Nicholas Joseph Quarta

A research report submitted to the Faculty of Engineering and the Built Environment, University of the Witwatersrand, Johannesburg, in partial fulfilment of the requirements for the degree of Master of Science in Engineering.

Johannesburg, 2012

Declaration

I declare that this research report is my own, unaided work, except where otherwise acknowledged. It is being submitted for the degree of Master of Science in Engineering in the University of the Witwatersrand, Johannesburg. It has not been submitted before for any degree or examination at any other university.

Signed this___day of_____2012

_____

Nicholas Joseph Quarta

Acknowledgements

I would like to express my sincere thanks to the following as it is through them that I was able to complete this research report.

First and foremost to Professor Sheer for his guidance, patience and mentoring through the duration of this research.

To Mr Thomas Roos of the CSIR for providing the opportunity to undertake this research as well as for his endless passion to see concentrating solar power become a reality in South Africa.

To Mr. Maurice Maliage of the CSIR as well as the staff at ESTEQ engineering for their assistance in Flownex.

To my parents, Domenico and Karin, as well as my brother Matthew for their endless support and guidance in times of need. To my grandfather for the many stories and talks we shared on Sunday afternoons.

To my colleagues, in particular Mr Andre Cachucho, Mr Steven Moss and Mr Prinal Naidoo who helped me through the good times and the bad, I express my thanks.

Finally I would like to mention the Institution of Wits University for providing me with an environment in which to mature and grow through the years in which I have been here. Many good memories within these walls will remain with me forever.

Abstract

This study involves the creation and analysis of a thermal-fluid network simulation model using a specified commercial software package (Flownex), as part of a larger solar power research programme at the Council for Scientific and Industrial Research (CSIR). The model was needed for performance simulation of a Concentrating Solar Power (CSP) system incorporating a Rover 1S/60 gas turbine engine with modified recuperator, to be used in a hybridised operation mode with a solar receiver and thermal storage unit. Full performance characteristics of the Rover 1S/60 gas turbine engine were required prior to the final model being created. Fuel leaks in the combustor resulted in unsustainable combustion, leaving the engine inoperable and testing results from Prinsloo (2008) were used as a means to validate the simulation results.

After the main components in the system had been characterised three simulation models were created using Flownex software, a standard Rover model – excluding recuperator, a modified Rover model – including recuperator and intake system, and a solar Rover model – including the solar receiver tower and thermal storage unit. Results of the models showed an increase in thermal efficiency, at the design operating point of 46000 revolutions per minute, from 10.5 % for the standard model to 12.8 % for the modified model and 14.1 % for the solar model. Furthermore the fuel usage was seen to decrease rapidly with an increase in solar power into the system. The thermal storage results were validated against testing results from Klein (2011). These were found to correlate well and yielded similar charging and discharging times. Further analysis showed that an increase in solar power input into the system as well as a larger-scale thermal storage unit would greatly increase the overall system performance and economic feasibility.

The model can be used to simulate other solar thermal systems of this type, with instructions provided in an appendix on how to do this. The program offers the ability to model combustion comprehensively with both reactants and products being

defined. It was recommended that Flownex is more than capable of modelling gas turbine systems of this type.

Additionally the program does allow the user to construct an interface environment which greatly simplifies the detailed network model into a manageable graphic interface to easily monitor performance parameters of the system. From a solar perspective while more advanced commercial software exists which allows for the sensitive modelling of the solar tracking aspect of a solar power plant combined with the power cycle, Flownex does allow the user to build custom defined power block components for incorporating solar heat inputs into any model and is a powerful tool for modelling thermal systems of this type.

The scientists of today think deeply instead of clearly. One must be sane to think clearly, but one can think deeply and be quite insane.

Nikola Tesla

Table of Contents

List of Figures

List of Tables

List of Abbreviations and Symbols

Abbreviations

CFD	Computational Flow Dynamics
CSIR	Council for Scientific and Industrial Research
CSP	Concentrating Solar Power
DNI	Direct Normal Irradiation
HE	Heat Exchanger
HTF	Heat Transfer Fluid
J.P.T.	Jet Pipe Temperature
kW_{th}	kilowatts Thermal
kW_{el}	kilowatts Electric
MW_{el}	Mega Watts Electric
NTU	Number of Transfer Units
PV	Photovoltaic
SANERI	South African National Energy Research Institute
TIT	Turbine Inlet Temperature
TOE	Ton's of Oil Equivalent
WITS	University of the Witwatersrand

Symbols

W_{in}	Work Input to Compressor [kW]
Q_{in}	Heat Input [kW]
W_{out}	Work Output from Turbine [kW]
$\dot{m}_{air}$	Mass Flow Rate of Air [kg/s]
$\dot{m}_{fuel}$	Mass Flow Rate of Fuel [kg/s]
C_p	Specific Heat [kJ/kgK]
T	Temperature [K]

P	Pressure [Pa]
W_{net}	Net Work Output for Cycle [kW]
η_{cycle}	Cycle Efficiency
η_{m}	Mechanical Efficiency
$Q_{HE,hot}$	Heat Exchanger Hot Side Heat Transfer [kW]
$Q_{HE,cold}$	Heat Exchanger Cold Side Heat Transfer [kW]
$\mathcal{E}$	Heat Exchanger Effectiveness
F/A	Fuel – Air Ratio
α_1	Inlet Stator Angle [°]
α_2	Exit Stator Angle [°]
β_2	Inlet Rotor Angle [°]
β_3	Exit Rotor Angle [°]
Pr	Prandtl Number
n	Engine Speed [rev/min]
k	Thermal Conductivity [W/mK]
h	Heat Transfer Coefficient [W/m^{2}K]
U	Overall Heat Transfer Coefficient [W/m^{2}K]
q	Heat Transfer Rate [kW]
ρ	Fluid Density [kg/m^3]
V	Volume [m^3]
v	Velocity [m/s]

1 Introduction

Climate and environmental impact studies over the past 30 years have created a growing concern as to how current growth and development is threatening the near, medium and long term future of the planet. Through this concern renewable energy development has leapt to the forefront of research topics in many developing and developed countries. One of the major conclusions made at the World Solar Conference in October 2009, held in Johannesburg, was that the global target of 100% renewable energies is both attainable and necessary by the middle of the current century, ISES (2009). It was further expressed at the conference that third world countries in particular cannot currently meet their energy demands and that this will not be solved by conventional power generation technologies in the near future but rather can be addressed cost effectively and in time by the use of renewable energy technologies. South Africa, in particular, has an abundant solar resource (discussed in Chapter 2) when compared to world standards and this resource has yet to be utilised for sustainable power generation or to address the fact that the country is the 12th largest CO_2 emitter and fossil fuel consumer and only the 32nd largest world economy, Roos (2006).

In an effort to research renewable energy and the solar resource potential for sustainable electricity generation in South Africa, the Council for Scientific and Industrial Research (CSIR) in Pretoria, funded by the South African National Energy Research Institute (SANERI) has undertaken a research investigation to analyse and construct a 100 kW solar thermal power plant of a central receiver tower configuration using a Brayton cycle. The plant is to be constructed at the CSIR in the near future and will be used for various research purposes. However prior to this construction an experimental test rig was to be analysed and tested using a 45 kW Rover 1S/60 gas turbine in order to develop and validate a simulation model which would be reusable for simulating the larger 100 kW system at a later stage. The solar component for this system was to come from a single 25 m^2 heliostat. The system was to use a technique referred to as “integrated thermal storage” in which energy is stored

thermally, and not electrically, in the form of heated pebbles. Thermal storage greatly increases the system's capacity factor. This is defined as the average power generated as a percentage of the total generating capacity of the plant. Storage allows the plant to generate power for longer. Due to ongoing modifications to the Rover 1S/60, as well as the age of the engine, dating back to the 1950's, very little information is available in terms of compressor and turbine maps as well as the effectiveness of the modified heat exchanger. Figure 1.1 shows the proposed system with the gas turbine unit and other components indentified. The workings of the system are discussed in Chapter 2.

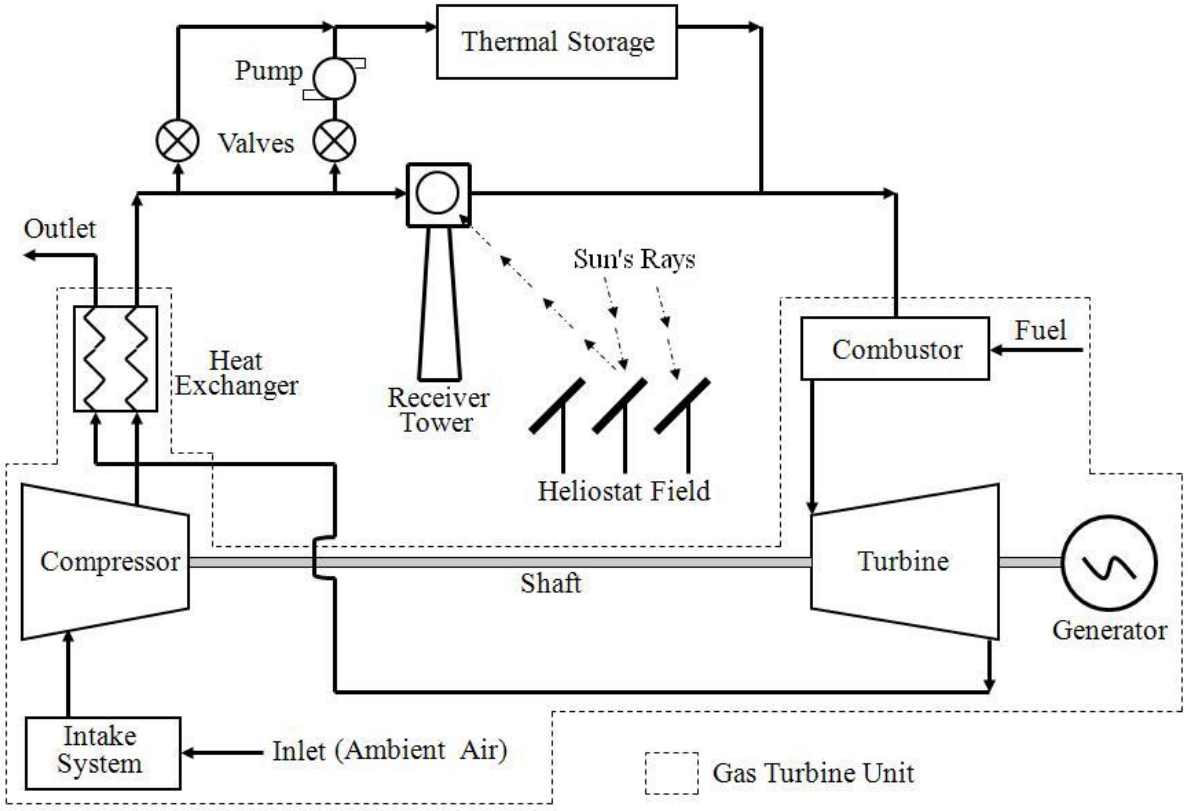

Figure 1.1: Hybridised Solar Gas Turbine System

The focus of the research described in this report is to explore the performance of the recuperative gas turbine engine used in a solar/fuel hybrid operation mode through the use of simulation software. Whereas work published to date (discussed in Chapter 2) examines the solar module of a solar thermal power plant with receiver tower and heliostat tracker, the work described here focused on the characterisation of an existing gas turbine unit and validating simulation software to be used to model a hybrid solar system for future research. The Rover 1S/60 gas turbine engine is currently inoperable and hence simulation was to be

used to provide a means for modelling specific components. These results will also aid in understanding the system's behaviour prior to future construction of the experimental system (which is outside the scope of this research report). The primary outcome involves assessing the suitability of the simulation model, to be used in modelling the larger 100 kW CSIR solar thermal power plant.

1.1 Objectives

1. The primary objective is to develop a computer simulation model of the 45 kW Rover 1S/60 gas turbine solar thermal power plant, with integrated thermal storage. This requires the generation of compressor and turbine maps as well as loss models for the ducting and heat exchangers and integrating these into the simulation model.

2. The model must be validated as far as possible, given that the Rover 1S/60 gas turbine would not be available for testing as part of this project.

3. The model must be applicable as a standard model for simulating Concentrating Solar Power (CSP) tower systems of this type, with the future objective of simulating the larger 100 kW CSIR system using the same model.

4. The Flownex software package, Flownex (2010), is to be used to develop the computer simulation model. This has been stipulated by the CSIR. The package was chosen for its ability to model network systems with turbine and compressor components, in particular the ability to specify detailed inputs for each of these components.

2 Literature Review

2.1 Solar Thermal Power

Solar thermal power involves replacing the heat input component of a conventional power station with solar heating. Thus instead of burning fossil fuels to generate the temperature levels required to run the specific cycle (Rankine, Brayton or Combined) the temperatures are attained through focusing incoming solar radiation onto a surface and heating the cycle's working fluid. This eliminates the need for fossil fuel during base load power generation and only in cases where the demand is very high or the incoming solar radiation, also referred to as insolation, is very low, then fossil fuels may be burnt in conjunction with the solar component to deliver the required power.

Solar thermal power plants utilise the direct normal irradiation (DNI) from the sun and concentrate it many times focusing all the irradiance onto a single relatively small area in relation to the plant size. This irradiance heats the working fluid used in the power generation cycle. This technology is referred to as Concentrating Solar Power (CSP).

Solar thermal power differs from photovoltaic (PV) power in that with solar thermal power the energy can be stored thermally through the use of heat absorbing media, whereas with PV electricity is only produced during daylight hours and the storing of electrical energy is expensive as large banks of batteries are needed. The storage of heat is hence a much easier and cheaper option. According to Solar Thermal Energy (2010) solar thermal power is currently the most cost effective solar technology when used in large scale applications such as the 11 MW PS-10 plant in southern Spain.

While solar thermal power allows for a more sustainable electricity supply, fluctuations do occur due to cloud movement as well as the diurnal cycle of the sun. These intermittencies are covered by the use of thermal storage and by supplementation with fossil fuels. Solar

technologies are best suited to areas which have a very high annual solar resource so as to minimise the degree of power fluctuation in the system from intermittencies such as cloud cover or bad weather conditions. In a study done by Romero et al. (1999) it is stated that by utilising the solar resource of less than 1% of arid and semi-arid areas it would be possible to supply the annual world demand for electricity today. The technology does however require a high initial investment as it has to compete with established, abundant and relatively cheaper coal technologies, Solar Thermal Energy (2010). A fully commissioned solar thermal power plant can be up and running within 25% of the time of a conventional power station. Along with this point the technology simultaneously addresses environmental, climate and fossil fuel depletion issues and by-products of the power generation process can be used for process heating and various other applications. Decentralisation is another major advantage as these plants are not dependent on large coal mines or gas reserves and small installations can be constructed in rural areas and used to power local communities.

The basic gas turbine operation remains unchanged save for the fact that the heat input occurs from the solar power, supplemented by the combustion of fossil fuel. This allows for less fuel to be used thus increasing the overall thermal efficiency of the system. For the type of system considered in the current research air is taken in and compressed before going through the recuperator where it is preheated using the exhaust gas of the turbine. Primary heating occurs either in the receiver tower or the combustor before the gases expand through the turbine blades to generate power. The thermal storage component allows the system to function at times of low insolation through the use of heat energy stored in ceramic pebbles (in the CSIR system). This heat is then discharged at night and provides a heat source for the system. For the charging of the thermal storage system the heated air from the receiver tower is cycled through the thermal storage tanks using a circulation pump until the desired temperature is reached. During this charging process the gas turbine does not run. Care must be taken to ensure that the turbine inlet temperature is always maintained. This means that when the solar fraction heat input decreases, combustion heat input must increase. If the turbine inlet temperature deviates too far from design temperature irreparable damage can be done to the turbine blades, Cohen et al (2001).

Of particular interest is how the P-v (Pressure-Volume) diagram of an ideal Brayton cycle is altered when integrated with a solar component. Figure 2.1 shows a schematic of a standard

Brayton P-v cycle that has been altered for solar/fuel hybrid operation (adapted from Fisher et al. 2004).

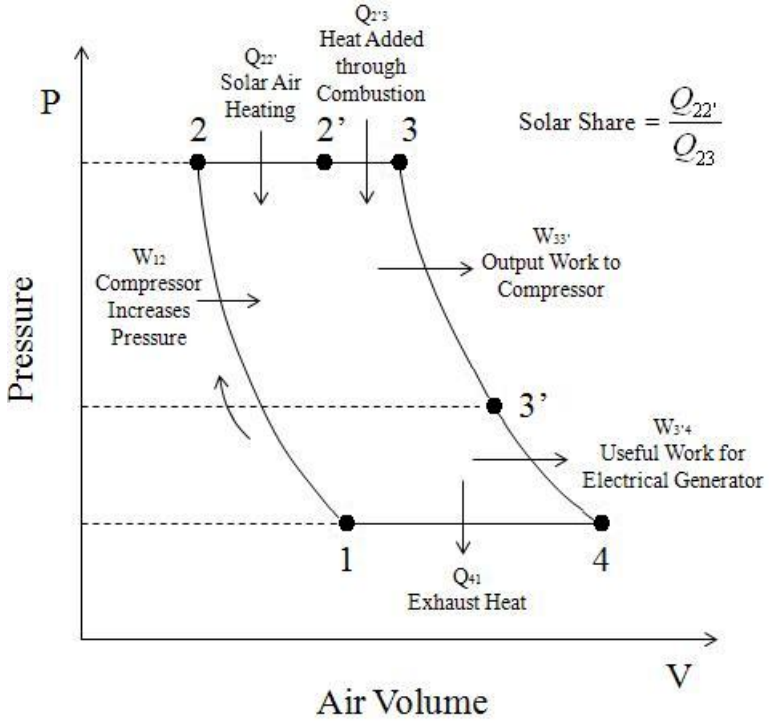

Figure 2.1: Brayton Cycle for Solar/Fuel Hybrid Operation (Fisher et al., 2004)

2.2 Various CSP Technologies

There are four major CSP technologies currently in operation with each technology using a different technique to concentrate the incoming solar radiation. These technologies are briefly described below.

Central Tower Receiver

This is the type of system with which this research report is concerned. It has a large array of heliostats which are mirrors mounted on supports that track the sun's motion and focus the sun's radiation onto a single point on a centrally located tower. A receiver mounted at this focal point absorbs this radiation and transfers it to the heat transfer fluid (HTF) that is used to drive the specific power cycle. This technology has higher efficiencies than the parabolic trough and linear Fresnel systems and can utilise a gas turbine instead of a steam turbine, thus

reducing the water demand for the system. The largest commercially operating central receiver tower plant is the Abengoa PS 10 plant in Spain, operating since 2007 and producing 11 MW_{el}, Fraunhofer (2009).

Parabolic Trough

The parabolic trough system uses a large array of parabolic mirrors which are set up linearly to track the sun's motion and focus the DNI onto the focal line where the absorber tube is located. This system is called a linear system. The absorber tube consists of a coated steel pipe surrounded by an evacuated glass tube and carries the HTF, usually thermal oil, molten salt or direct steam. For both thermal oil and molten salt a heat exchanger is required, however for direct steam generation no heat exchanger is required.

Linear Fresnel

The Linear Fresnel system is also classified as a linear system except that the reflectors concentrate the incoming solar radiation onto a stationary absorber tube mounted above the reflectors. Each reflector is a long, thin linear mirror which tracks the sun's motion. A secondary reflector in the form of a curved mirror is mounted just above the absorber tube and runs the length of the tube in order to capture any lost radiation from the linear mirrors on the ground and re-concentrate it onto the absorber tube. Again the absorber tube is a coated steel pipe surrounded by an evacuated glass tube.

Dish Stirling

The Dish Stirling system utilises a large parabolic dish mirror to focus all light onto a receiver mounted at the focal point of the dish. This concentrated beam radiation is used to heat a HTF. This fluid is then used to generate electricity in a small piston, Stirling or micro turbine engine mounted on the receiver. Temperatures can reach 500°C to 750°C and even higher depending on the mirror size. Individual systems can be 10 – 50 kW per unit and can be set up in remote areas, Fraunhofer (2009).

For each of the technologies mentioned, design variations exist which serve to increase the efficiency of each system as well make them economically feasible. These include hybrid

fuel systems like the system under investigation described in Chapter 1, integrated thermal storage to allow the system to operate outside of daylight hours and combined cycle applications utilising both gas and steam turbines in the same system.

2.3 CSP and South Africa

Solar thermal power technologies require a high level of DNI and it is of high importance that an area be characterised for its DNI and deemed suitable for implementing the technology. Figure 2.2 shows a study of South Africa's annual solar radiation, ignoring cloud pollution, conducted by the CSIR in cooperation with Eskom and the Department of Minerals and Energy.

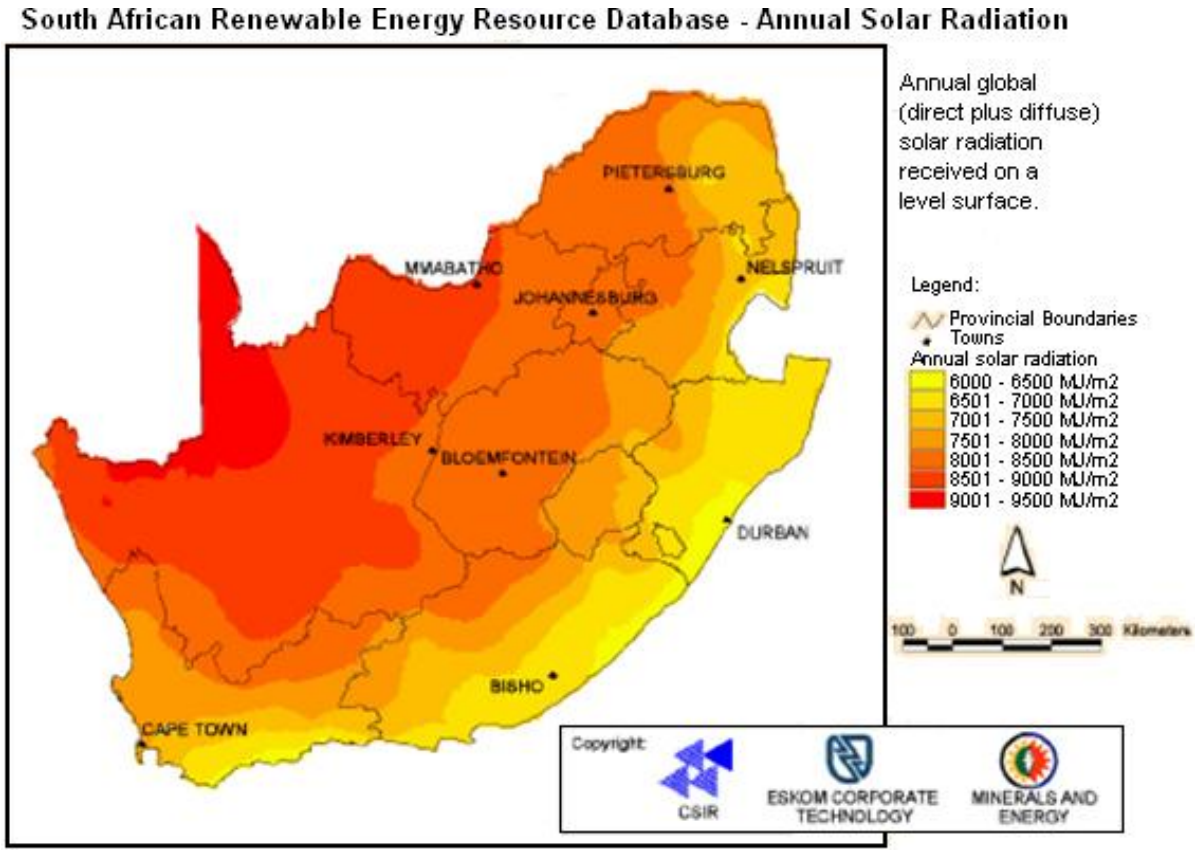

Figure 2.2: South Africa's Annual Solar Radiation (Roos, 2006)

From the study it can be seen that an average value of 7500 MJ/m^2 and a maximum of between 8500 MJ/m^2 and 9500 MJ/m^2 of solar radiation falls on South Africa each year. This converts to between 2361 kWh/m^2 and 2639 kWh/m^2 annually. According to Stine and Geyer

(2001) a suitable site for solar thermal power should receive an average of 1700 kWh/m^2 annually and ideal sites 2800 kWh/m^2 annually. Along with this the site should preferably be flat and arid desert or semi-desert so as to minimise cloud pollution and atmospheric humidity produced from vegetation and climate conditions.

Thus South Africa is ideally suited from a solar resource point of view to implement solar thermal technologies, and even in Pretoria where this particular research is being conducted the solar radiation is well above the minimum required value to make the technology viable. Other reasons for implementing this technology include its high potential to be decentralised as currently 27% of South Africans have no access to electricity, mainly due to infrastructure and capacity problems, as well as addressing the current energy crisis which the country has been facing since 2007, Roos (2008).

2.4 Simulation Approaches to CSP Systems

Much research has been done concerning the testing and evaluation of solar thermal power plants, in particular investigating turbine inlet temperature by measuring the outlet temperature of the solar receiver. Some studies also investigate modifications to gas turbine engines in order for them to be used in solar hybridised applications. With regard to the simulation of these systems, few studies have been reported that analyse the system in detail as most studies single out the solar portion of the power plant.

Separate studies done by Fisher, et al. (2004) and Heller, et al. (2006) look at the operation of the SOLGATE project, SOLGATE (2002), which is a solar hybrid gas turbine system of a central receiver tower configuration at the CESA-I tower facility in Plataforma Solar de Almeria (PSA), Spain. Here the volumetric/solar receiver consists of three 400 kW_{th} modules which deliver pressurised air at approximately 1000 °C to the main system, see Figure 2.3. The main “power block” of the system uses a Brayton cycle with a modified helicopter gas turbine engine (OST3) and a generator coupled to the grid. The combustor was modified slightly to handle higher temperatures and the control system changed to allow the heat supply to vary between fossil fuel and solar for hybrid operating conditions.

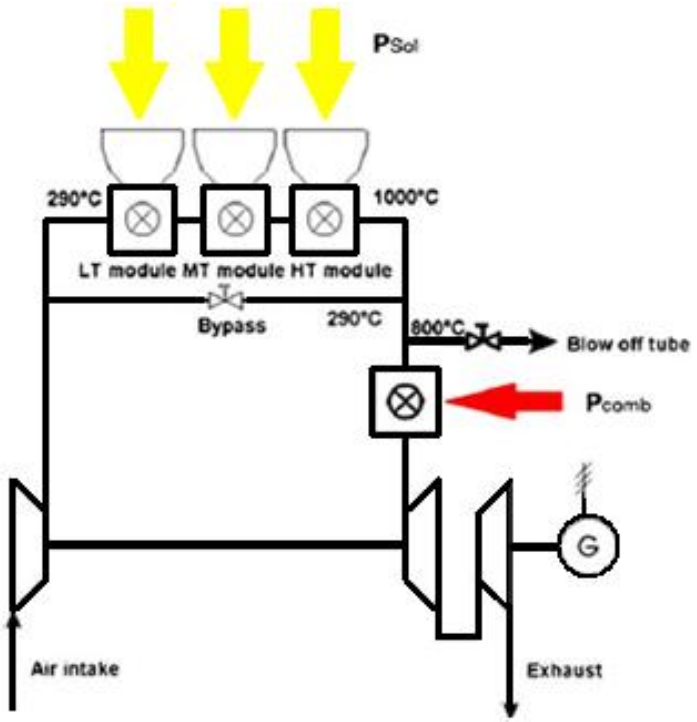

Figure 2.3: SOLGATE Test System Schematic (Heller et al., 2006)

The system consists of 55 heliostats delivering 900 W/m^2 of direct normal irradiation. Total gross heat input was found to be 1246 kW_{th} with 499 kW_{th} from fossil fuel and 747 kW_{th} from solar. An output temperature of approximately 960 °C was attained from the receiver tower. An electrical power production of 230 kW_{el} was attained. The gas turbine efficiency was around 20%. Figure 2.4 shows the gas turbine performance for design conditions.

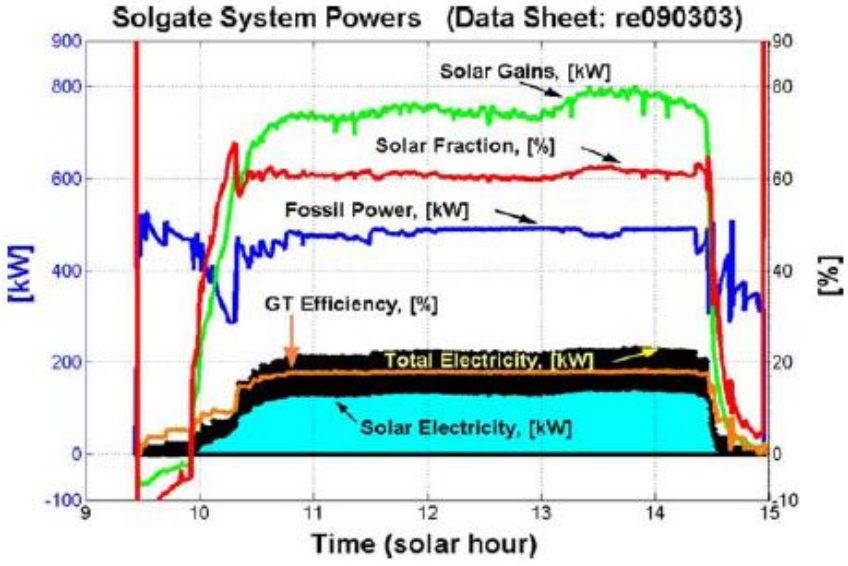

Figure 2.4: Gas Turbine Overall Performance (Heller et al., 2006)

These studies concluded that high temperatures of 1000°C were attainable in volumetric receivers with air as the heat transfer fluid and that a gas turbine engine could be successfully operated in solar/fuel hybrid installations.

From a simulation perspective, Berenguel, et al. (2005) considered a typical operating cycle of a Rankine system at the CESA-I solar plant in Plataforma de Almeria, Spain. The simulation was conducted using the thermo-fluid modelling frameworks of Modelica and Dynamola, two commercially available programs used to model complex physical systems. The model primarily considered the solar component of the plant and excludes typical components such as turbines and generators. The CESA-I plant uses a Rankine cycle to generate power, however air is the primary heat transfer fluid used in the solar receiver. The air then passes through a heat exchanger generating steam for the Rankine cycle. The plant makes use of thermal storage tanks in order to increase overall efficiency. The model of the plant is shown in Figure 2.5.

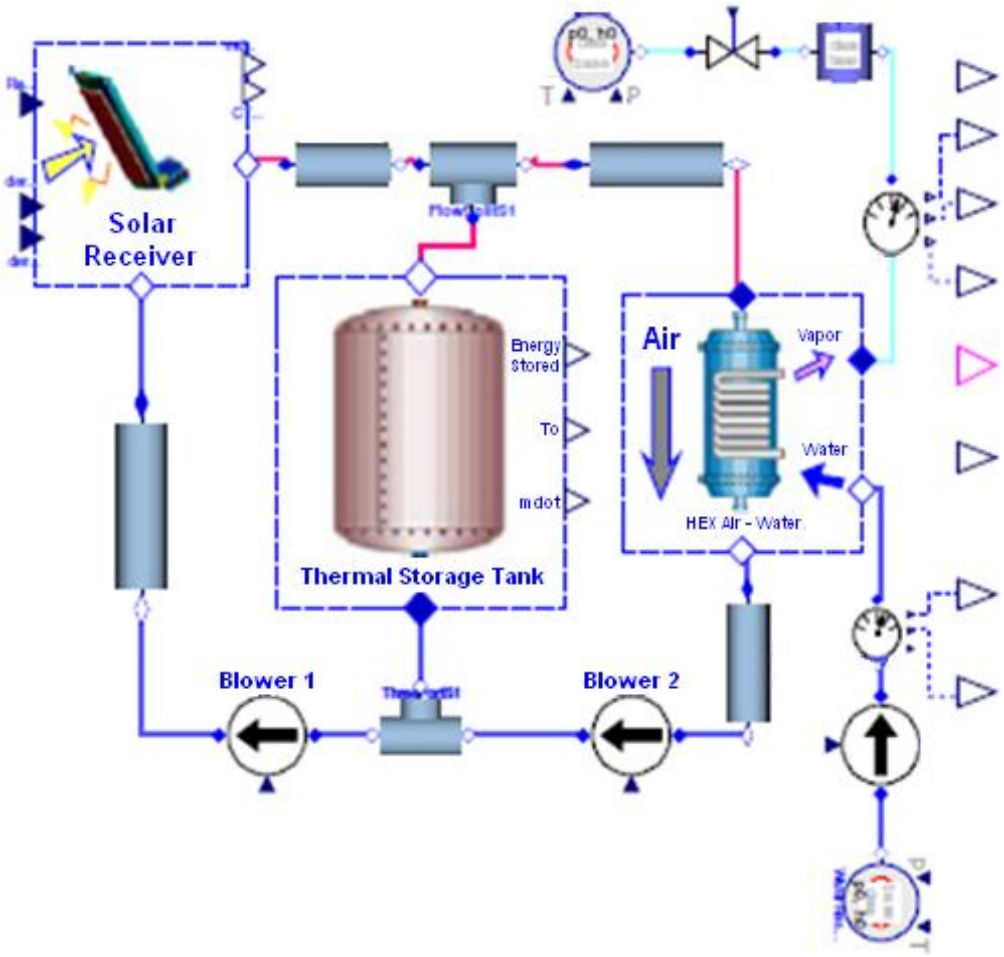

Figure 2.5: Modelica Model of CESA – I (Berenguel et al., 2005)

The study focuses on three specific elements of the plant in detail, namely the solar receiver, thermal storage tank and air-steam heat exchanger. For the solar receiver a known input radiation was used as an input into the model. The thermal storage tank was defined by three states: loading, unloading and standby. The states are controlled by varying the mass flow rates of the external blowers 1 and 2 seen in Figure 2.5 above. The heat exchanger is of a counter flow configuration with a helicoidal water/steam pipe and is modelled just as a pipe element of finite length. The simulation scenario involved an initial state where the storage tank is unloaded, incoming solar radiation is zero and ambient conditions hold for other components. At a time t = 0s the input power reflected is 10 MW in the receiver and the thermal storage tank begins to charge, no power is delivered to the heat exchanger at this time. At t = 2000s all energy from the solar receiver is sent to the heat exchanger in order to generate steam, the storage tank remains unchanged. When the time reaches 15000s zero power is sent to the solar receiver in order to simulate a passing cloud and all energy required by the heat exchanger comes from the storage tank. This method of simulating the energy input into the solar receiver can be used in a similar manner for the Flownex model. However with the system under investigation for this research report, fossil fuel will be used to supplement the solar power in the case of a passing cloud as discussed here. The thermal storage unit is primarily used during non-daylight hours to provide heat to the system.

Berenguel, et al. (2005) concluded that the model showed the accumulated energy in the storage tanks was sufficient to maintain the outlet superheated steam temperature when the incoming solar radiation dropped off.

Schwarzbozl, et al. (2006) discussed the design and performance of several prototype solar tower power plants ranging in size from 1 MW to 15 MW. For the optical part of the tower system an adapted version of the HFLCAL code developed in 1989 by Becker and Bohmer was used, along with simulation environment TRNSYS (2011) for the thermal power system and annual performance calculations. Schwarzbozl, et al. (2006) validated both models against measurement data from solar experiments at the PSA in Spain.
The study considered three industrial gas turbine systems.

- Heron H1 intercooled, recuperated two shaft engine with ISO rating 1.4 MW and thermal efficiency 42.9%
- Solar Mercury 50 recuperated single shaft engine with ISO rating 4.2 MW and thermal efficiency 40.3%

- PGT 10 simple gas turbine with combined cycle. ISO rating 11.1 MW (gas turbine) and 16.1 MW (combined cycle) with thermal efficiencies 31.3% and 44.6% respectively.

Two sites were considered, namely Seville in Spain and Dagget in California, USA for their solar potential and market perspectives. The simulations were created for the three systems each with three solar receivers, for high, medium and low flux regions of the focal spot created by the heliostat field, again similar to the SOLGATE (2002) system. The solar heat input was stipulated as an incoming radiation relative to the zone in which the receiver was situated.

The TRNSYS software allows the analysis of a typical meteorological year on an hourly basis for each simulation. The software produces results that describe the economical feasibility of the system as well as the system's performance. Of interest to the current research study are the results which showed how the capacity factor and solar share varied for each of the specific turbine engines (see Figure 2.6).

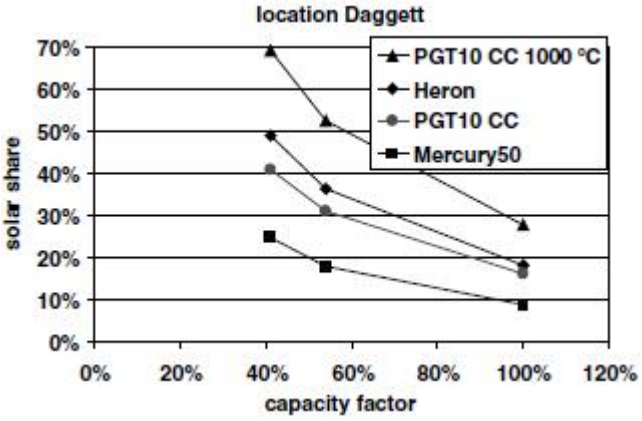

Figure 2.6: Solar Share Vs. Capacity Factor for Daggett (Schwarzbozl et al., 2006)

The figure explains that by reducing the capacity factor by limiting the plant operation to daytime only hours or sun hours, the solar share naturally increases. Maximum solar share is seen to be around 70% for the PGT10 combined cycle unit at 1000°C receiver outlet temperature.

From another perspective Romero, et al. (1999) investigated distributed power from solar thermal systems in a Modular Integrated Utility Systems or MIUS approach. The study considered various plant configurations as well as applications where the system can be used

to generate local power and tri-generation applications for domestic water heating and cooling. This particular approach is similar to the research being done at the CSIR. The outcomes of the final large scale solar thermal plant will have off grid applications in line with these mentioned by Romero, et al. (1999). A schematic diagram of the proposed idea is shown in Figure 2.7.

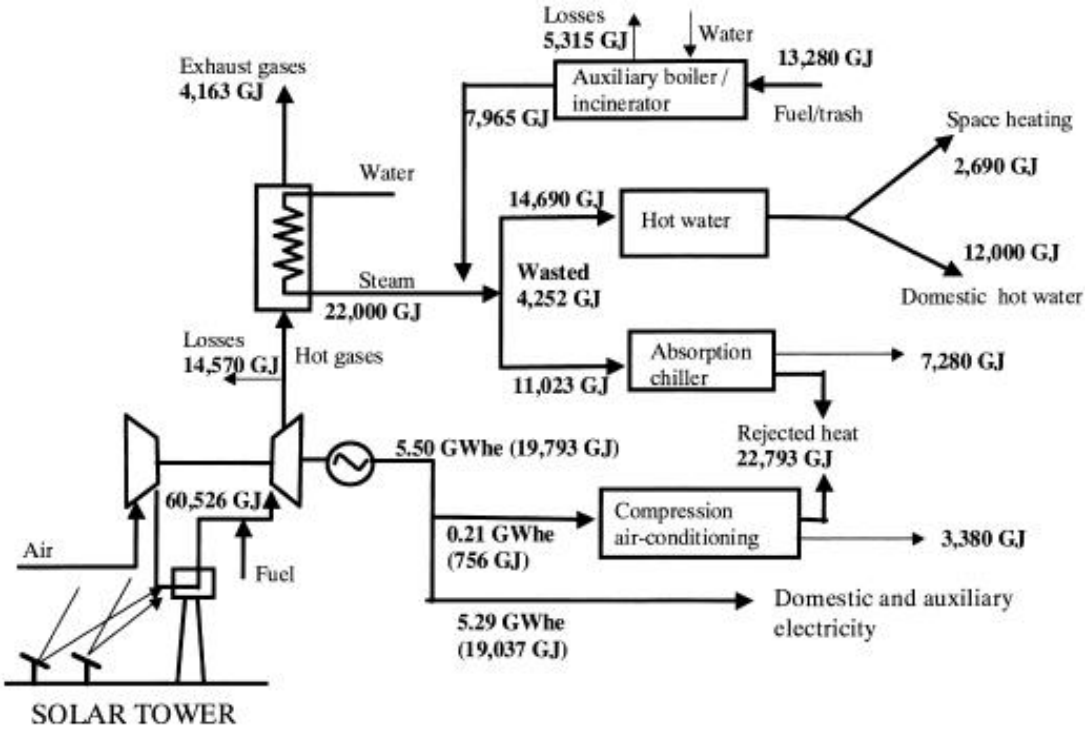

Figure 2.7: Schematic of a MIUS Approach (Romero et al., 1999)

For the study a central receiver solar thermal power plant was considered. The plant consists of a 1.4 MW Heron H-1 two shaft gas turbine with intercooling and two stage combustion. Thermal efficiency is 36.6% and turbine inlet temperature 860°C. Hybridisation of the engine was done by introducing hot air from the solar receivers in parallel to the high and low pressure combustors. During this fossil fuel operation mode up to 0.09 kg/s of fuel is added to the air.

Romero, et al. (1999) state that the pure solar mode of operation yields an electrical efficiency of 39.5% while the fossil fuel mode yields an electrical efficiency of 42.9%. This indicates that when the system operates in solar mode, more solar power is required in order for the same system efficiency to be reached. During standard combustion mode the fuel delivers 3280 kW to the system, hence in order for the solar operation mode to reach the

same efficiency the solar receiver would need to deliver 3440 kW. Figure 2.8 which follows illustrates the system involving the gas turbine with intercooler, recuperator, both combustors and various solar receivers. The solar tower's performance was analysed using TRNSYS (2011).

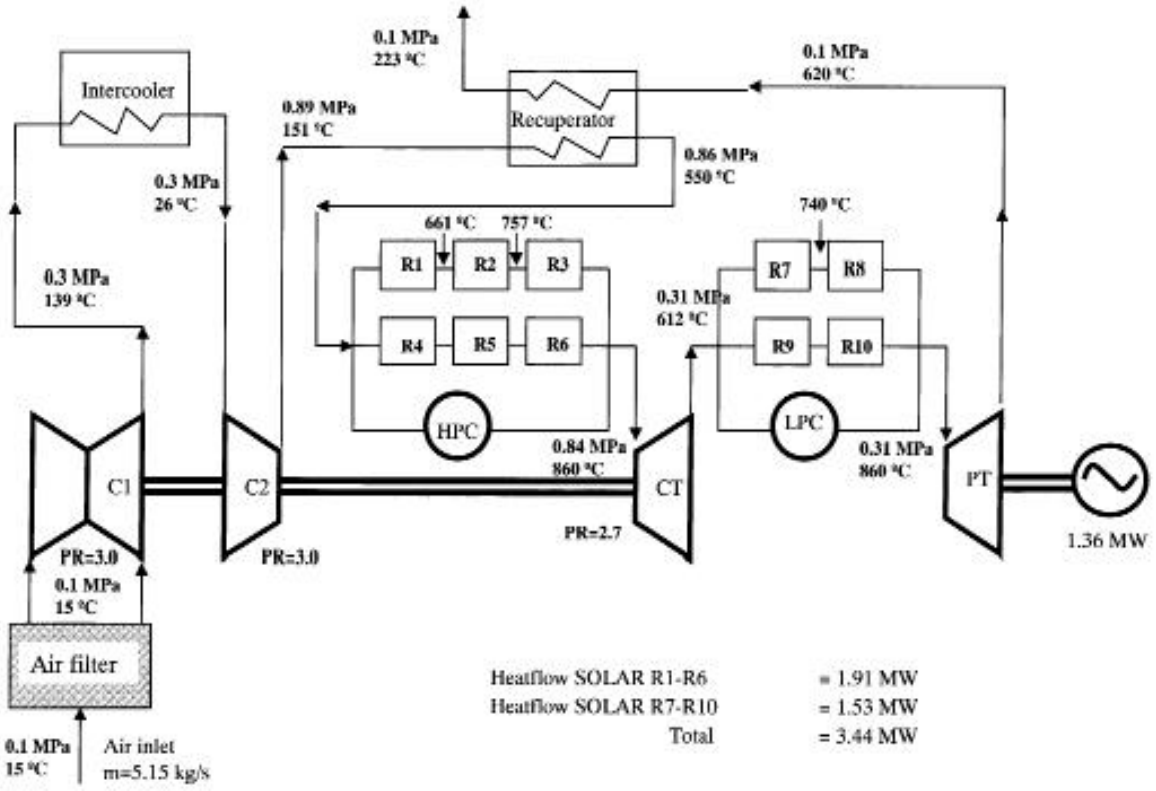

Figure 2.8: Hybridised Heron H-1 Gas Turbine System (Romero et al., 1999)

The system depicted in Figure 2.8 is very similar to the system with which this research report is concerned, save for the fact that the Heron H-1 has two shafts, intercooler and two stage combustion. A study was conducted for a case where the system would produce power and waste heat for a shopping centre in the south of Spain. Using a shopping centre for the study means that up to 85% of electricity demand is during daylight hours. The results of this analysis can be seen in Figure 2.9.

The peak electricity demand (shown by the thick dark line of crosses at the top of the graph in Figure 2.9) occurs during the summer months as expected due to the increased power needed for cooling of the centre; also the best results for the plant operation are seen during the summer months due to the increased daylight hours and DNI. The system runs in solar/fuel hybrid operation mode with the excess solar share also shown on the graph. Solar power

excess refers to the amount of DNI that was not used in solar power electric production at the particular time of the year.

Romero, et al. (1999) concluded that the solar system resulted in an energy saving of 687 TOE (tonnes of oil equivalent) per annum. Hence when solar thermal power technology is used in this approach the immediate useful potential can be realised.

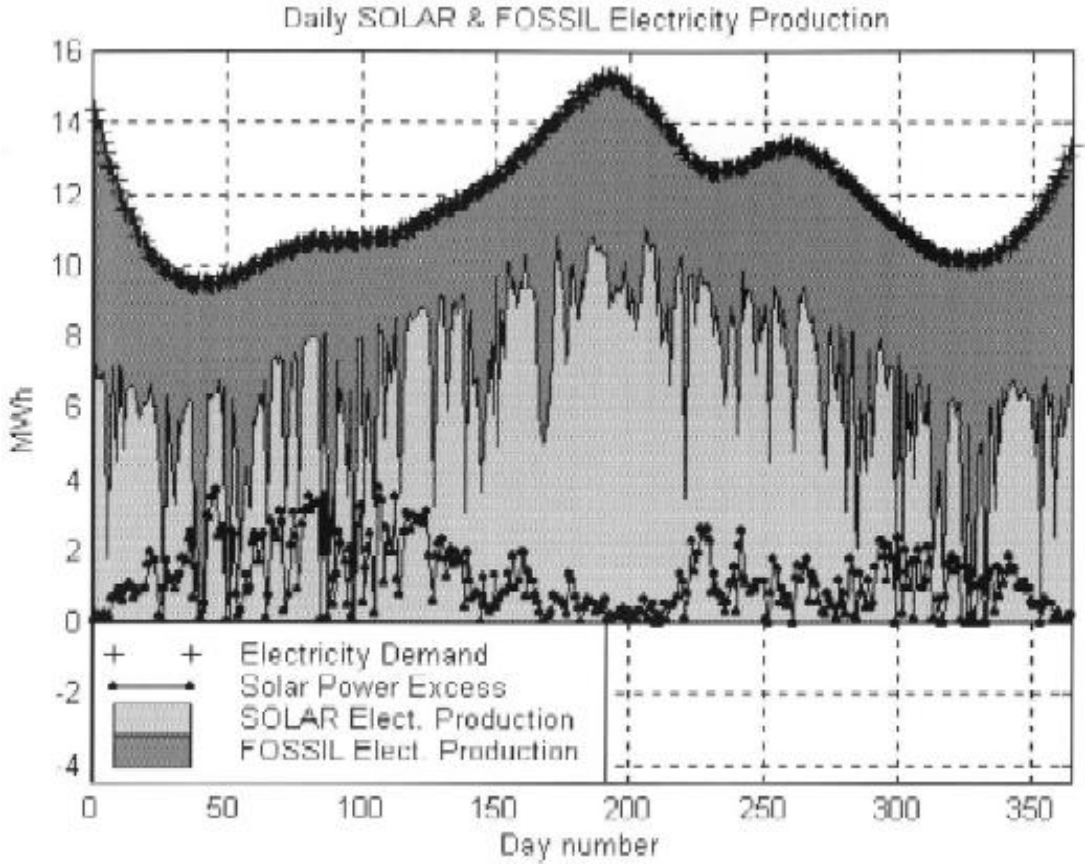

Figure 2.9: Annual Distribution of Electricity Demand for Shopping Centre, Southern Spain (Romero et al., 1999)

The models investigated with respect to this research report combine aspects of the solar system and thermal power system into one simulation model, looking in particular at the gas turbine system and its characterisation and operation. Specifics pertaining to the gas turbine concerned with this report are discussed in the following chapter.

2.5 Compressor and Turbine Maps

Turbomachinery components can be complex and difficult to understand due their fluctuating behaviour under varying operating conditions. In order to simplify their performance characteristic “maps” are developed for each component. These maps incorporate two specific parameters to describe the performance of the component, namely the corrected speed and corrected mass flow rate along with pressure ratio and efficiency data. Through the use of these parameters a particular compressor, pump or turbine can be scaled to any desired operating point. During standard operation the compressor runs at the operating point. This point moves on the graph relative to the conditions under which the compressor is working.

An important aspect as well as a crucial precaution to understand is the phenomenon known as compressor surging. This is when the forward flow through the compressor is no longer maintained due to a significant rise in pressure across the compressor; hence the flow is reversed momentarily. However as this occurs the downstream pressure is reduced while at the same time suction pressure increases and hence the flow moves forward once again. This repetitive effect of the flow continuously reversing and correcting itself is called surging. This will continue to occur until a change is made in the operating conditions of the compressor or until mechanical failure. With respect to the compressor map, surging occurs when the operating point moves outside of the surge line which is indicated on any standard compressor map supplied by the manufacturer. Examples of turbomachinery maps can be seen in Figure 2.10 below.

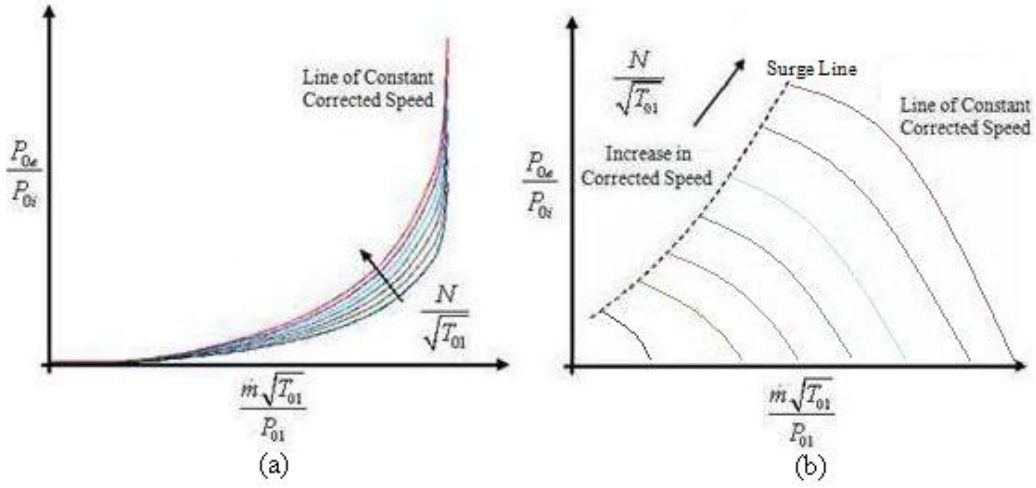

Figure 2.10: Compressor (a) and Turbine (b) performance maps (Flownex, 2010)

The parameters mentioned above are defined by the equations which follow.

P_{02}/P_{01} = total-to-total pressure ratio over compressor. (2.1)

$\dot{m}\sqrt{T_{01}}/P_{01}$ = corrected mass flow rate [$kg/s \times \sqrt{K}/bar$]. (2.2)

$N/\sqrt{T_{01}}$ = corrected speed [$rev/s/\sqrt{K}$]. (2.3)

Where:

$\dot{m}$ = mass flow rate through compressor [kg/s].

N = rotational speed of compressor [rev/s].

P_{02} = downstream total pressure [Bar].

P_{01} = upstream total pressure [Bar].

T_{01} = upstream total temperature [K].

3 Equipment and Previous Work Overview

This chapter details all equipment pertaining directly to the research being discussed. First the Rover 1S/60 gas turbine is introduced, its basic operation is described and standard operating conditions are stated. Following this all modifications and operational tests completed to date are listed. The section concludes with the components of the engine that were characterised and the experimental problems that were addressed.

3.1 Rover 1S/60 Gas Turbine

The Rover 1S/60 gas turbine engine dates back to the 1950's when the Rover Company developed the engine to compete with the conventional internal combustion engine. The company presented the very first public demonstration of a gas turbine automobile. The engine was extremely light in weight (140 lbs or 63 kg) and developed high power outputs for its weight. However the concept failed to achieve economic feasibility due to the significant fact that the fuel consumption was stated to be twice that of the conventional petrol engine of the time. Rover developed three variants of the gas turbine automobile. The third model in particular, the Rover T3, used a modified Rover 1S/60 gas turbine that was mounted on the rear chassis of the car and used to drive both the front and rear wheels, Judge (1960). The engine did however find use in auxiliary power generation applications as well as water pumping applications, again due to its small size and weight. Figure 3.1 shows the basic construction of the Rover 1S/60.

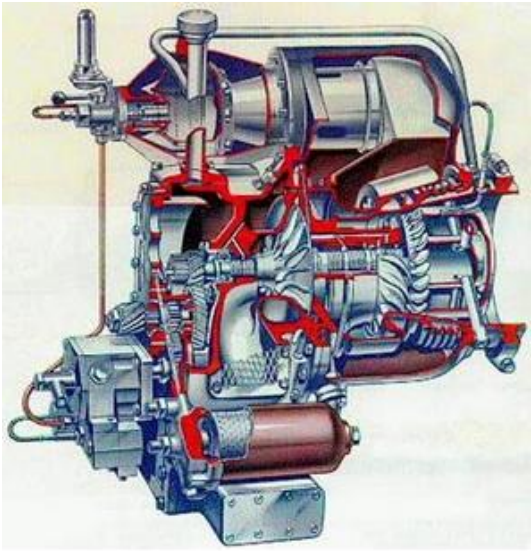

Figure 3.1: The Rover 1S/60 Gas Turbine Engine (IET, 2010)

The engine configuration is single shaft and makes use of a reduction gear; no free turbine is present. The major components include the single stage centrifugal compressor, one reverse flow can-type combustor and the single stage axial turbine. Other minor components are the exhaust cone, also known as the exit diffuser, fixed vane diffuser, component casings, and all piping for fuel delivery. The starter motor is located on the underside of the compressor housing and transmits drive through the oil pump gear as well as an intermediate gear to a pinion on the main shaft to start the compressor.

The flow of air through the system is illustrated in detail by the gas flow diagram of Figure 3.2, obtained from Rover (1966).

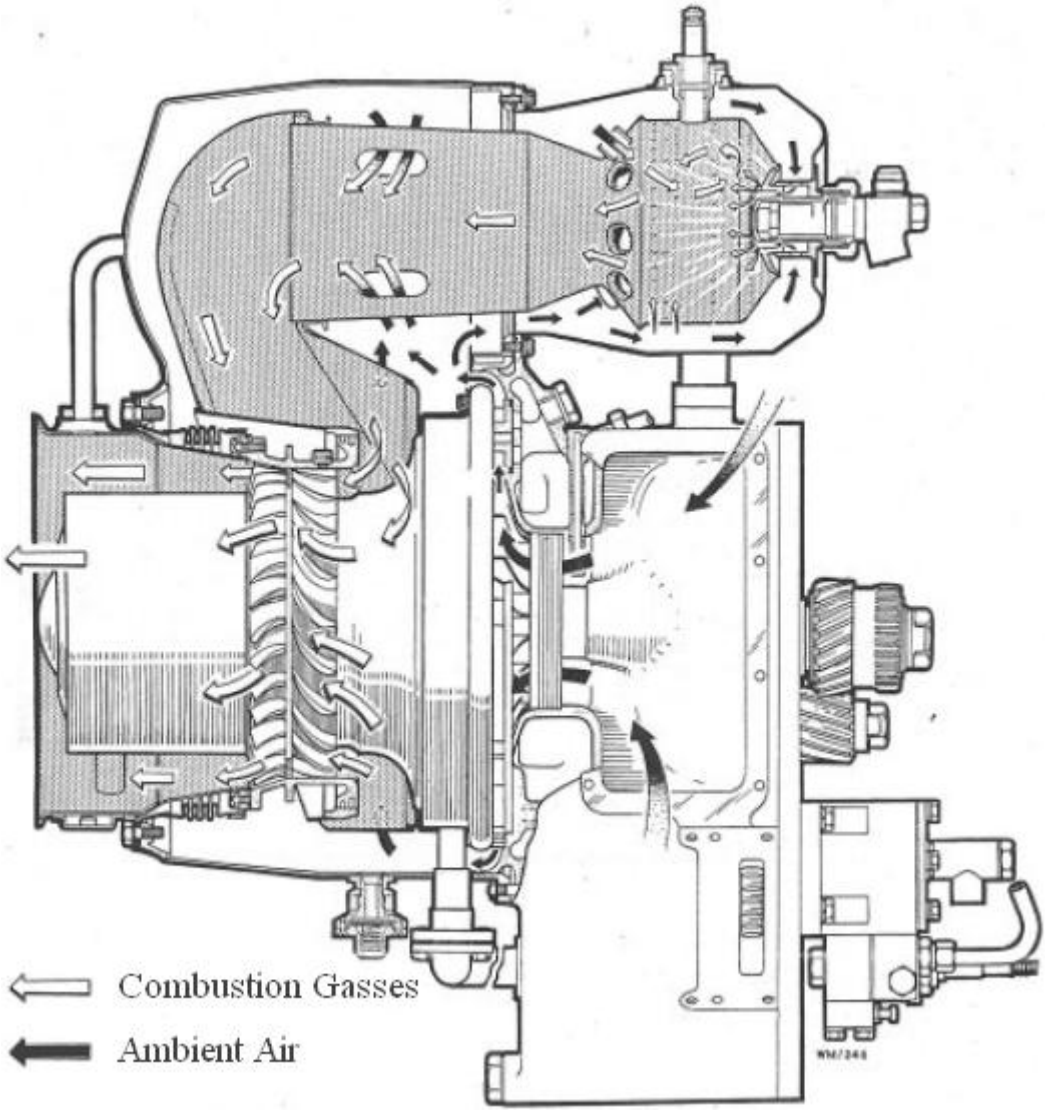

Figure 3.2: Gas Flow Diagram for the Rover Engine (Rover, 1966)

As illustrated the air enters the impeller of the centrifugal compressor through two inlets located either side of the compressor. The air is directed outwards by the impeller into the fixed diffuser vanes where the velocity is slowed and pressure increased. This pressurised air is then directed into the main air casing where it enters the can-type combustor at the rear end (top right side on the figure) and mixes with fuel from the sprayer atomiser. When the engine is run from start-up an electrical spark plug ignites the mixture with a continuous spark until operating speed is reached, at this point the combustion is self sustaining and no more spark is required. The combustion gases then expand down the combustor to the secondary zone where they are mixed with fresh air through large equally spaced swirl holes. This is done in order to ensure that the design inlet temperature of the turbine is not exceeded in the combustor. The resulting mixture now expands through the volute and enters the stator stage

of the axial turbine where the flow is guided onto the rotating rotor blades. The expanded gases then exit the turbine via the exit diffuser or exhaust cone.

The maximum speed of the engine is controlled via a centrifugal leaf spring governor that is part of the fuel pump rotor. The governor is constantly under centrifugal force and will spill fuel off from the high pressure side of the fuel pump until the predetermined speed is reached, whereby only enough fuel is fed into the sprayer to maintain this speed, Rover (1966).

All standard technical information pertaining to the Rover 1S/60 engine can be viewed in Table 3.1 which follows. It should be noted that the air mass flow rate specified is for sea level conditions, thus a new mass flow must be calculated for operation at altitude.

Table 3.1: Technical Data of the Rover 1S/60 Gas Turbine Engine (Rover, 1966)

Technical Data (Design conditions)	
Altitude	Sea Level
Barometric Pressure	101.325 kPa
Fuel	Diesel or Kerosene
Compressor	Single Stage, Centrifugal
Combustor	Reverse Flow, Can Type
Turbine	Single Stage, Axial
Main Shaft Speed (Governed)	46000 RPM
Air Mass Flow	0.603 kg/s
Pressure Ratio	2.8 : 1
Turbine Inlet Temperature	750 °C
JPT (Jet Pipe Temperature)	580 °C
Net Power Developed	45 kW (60 hp)
Fuel Consumption	0.476 kg/kWh

3.2 The Modified Rover 1S/60 Gas Turbine

The Rover 1S/60 gas turbine is currently housed in the Thermo-Flow laboratories at the University of Pretoria. Prior to being here it was located at the University of Stellenbosch in the Western Cape where it was used for research purposes, however it has been out of commission since the 1990's and only in 2008 was it run again when Prinsloo (2008) conducted an overhaul of the engine. Figure 3.3 depicts the current Rover 1S/60 gas turbine as it stands today.

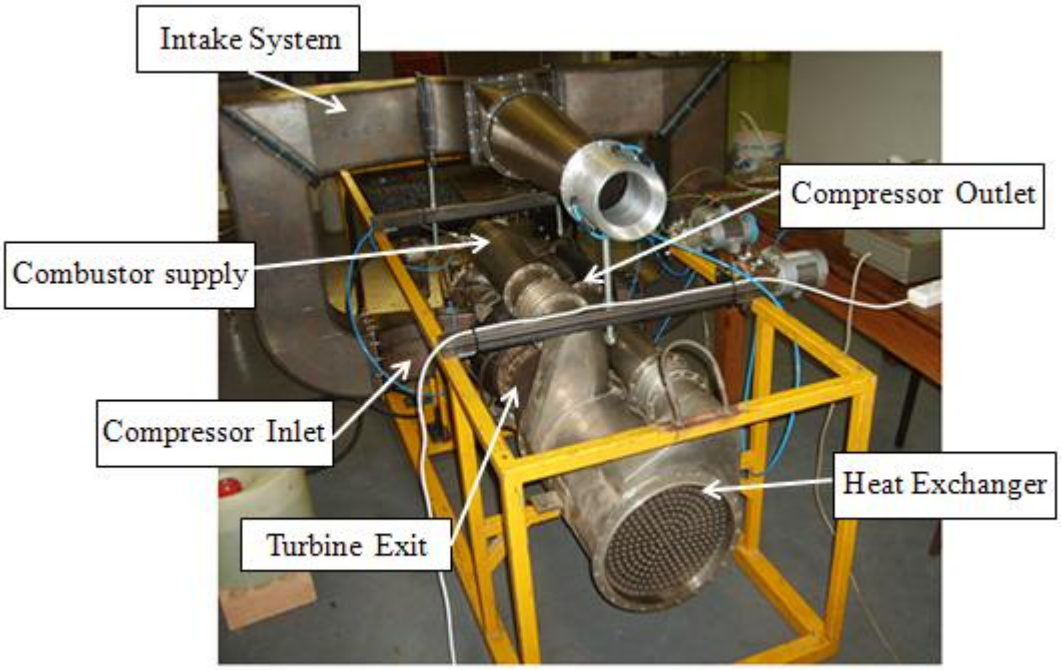

Figure 3.3: Current Rover 1S/60 Gas Turbine Engine

While the engine was at the University of Stellenbosch a cylindrical shell and tube counter-flow heat exchanger was added to the unit in order to increase the overall efficiency. This resulted in the original engine being converted from a simple Brayton cycle to a regenerative one and hence altered the configuration of the engine components. As far as the effectiveness and other performance characteristics of the heat exchanger go, no information regarding the modifications could be obtained. The modifications to the heat exchanger are indicated in the figure above as well as the modified compressor delivery and combustor supply lines to and from the heat exchanger.

Above and beyond these modifications Prinsloo (2008) installed an intake system onto the engine as labelled in Figure 3.3. The conical inlet of the intake system is instrumented with pressure transducers to measure the air mass flow rate and Mach number for the system. The intake system also ensures that the air is thoroughly filtered prior to entering the impeller.

3.2.1 Previous Testing Results

Solar research work using the Rover 1S/60 gas turbine from Stellenbosch University began in 2008 with Prinsloo (2008). His work consisted of dis-assembling and re-assembling the engine as well as establishing various properties and measurements through running operational tests in the Thermo-Flow laboratory at the University of Pretoria. Measurements were taken at various points on the engine through the use of pressure transducers and thermocouples, the most important of which are listed below.

- Air mass flow rate (measuring differential pressure at the conical inlet).
- Pressure drop across the intake system.
- Pressure rise across the compressor.
- Pressure loss across the hot and cold sides of the heat exchanger.
- Temperatures for the hot and cold sides of the heat exchanger.

Graphs of processed results attained by Prinsloo (2008) can be viewed in Appendix A. From the graphs the following points were concluded (note: The only resultant load present during the tests was that created by the gearbox and the generator):

- The intake system pressure drop measured, approximately 1.5 kPa (Figure A.4), was far in excess of the theoretical prediction of approximately 770 Pa for a mass flow rate of 0.5177 kg/s at an engine speed of 40 000 rev/min. Prinsloo (2008) attributed this to the fact that no information was available for the air filters, as well as manufacturing imperfections in the intake assembly.
- The performance of the compressor indicated that the original estimation of the isentropic efficiency of 71% at design point was feasible. The isentropic efficiency under no load was found to increase to a value of approximately 60% at 40 000 rev/min under no load, Figure A.6.

- The pressure ratio was found to increase with an increase in engine speed and mass flow until 40 000 rev/min, see Figure A.7. The pressure ratio reaches a value of 2 at an engine speed of approximately 40 000 rev/min, indicating that a pressure ratio of 2.8, as specified by the manufacturer, is indeed attainable for the design speed of 46 000 rev/min. Results also confirmed the predicted mass flow rate of 0.52 kg/s at operating point for the altitude of Pretoria to be feasible.
- The cold side percentage pressure drop was found to be just below 1.6% in Figure A.9. This was well above the theoretical approximation of 0.4% due to a number of refining assumptions used by Prinsloo (2008) in his calculations. The hot side heat exchanger pressure drop was found to be 0.7%.

Furthermore another Pretoria University student conducted a detailed investigation into the combustion problems that were experienced by Prinsloo (2008). Phakathi (2009) tested the fuel sprayer and fuel delivery system independently from the gas turbine unit. The following was concluded:

- During an overhaul of the Rover 1S/60 fuel system components it was concluded that both the fuel sprayer and fuel pump were in adequate condition.
- This resulted in the two components being tested and led to the discovery of a leak in the fuel sprayer at a pressure of 3.45 MPa. An O-ring was replaced on the sprayer and hence normal spray distribution results were achieved during further tests.

Beyond this no further testing was done since the work of Phakathi (2009). Full details with regard to all major components on the Rover 1S/60 gas turbine follow in Section 3.3.

3.3 Specific Engine Components

This section documents all major components of the Rover gas turbine engine. Each part is described and characterised before theoretical predictions and simulations can be performed.

3.3.1 Intake System

The intake system is responsible for delivering air to the compressor. The system filters the air and measures the air mass flow rate and Mach number by measuring the pressure differential using pressure transducers mounted at the conical inlet. The ducting system was designed by Prinsloo (2008) to British Standard *BS 848 Part 1: Fans for general purposes.* Figure 3.4 shows the system with a corresponding reference table and flow direction labels.

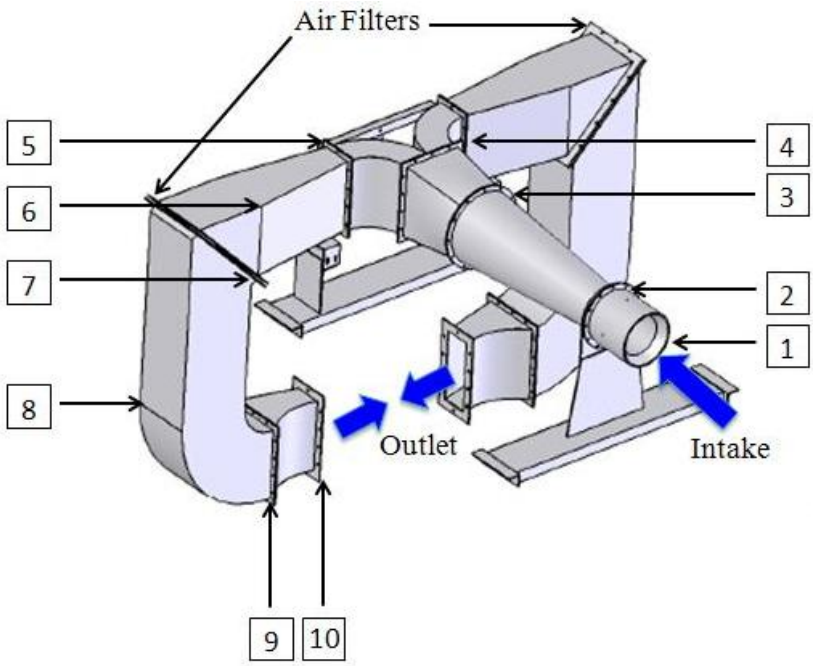

Reference Table	
Number	Description
1	Conical Inlet
2	Diffuser Inlet
3	Diffuser Exit
4	Round to Square Exit
5	Splitter Exit
6	Square Diffuser Exit
7	Filter Bend Exit
8	Bottom Bend Inlet
9	Bottom Bend Exit
10	Nozzle Exit

Figure 3.4: Intake Ducting with Reference Table, adapted from Prinsloo (2008)

A table was constructed which summarises all specific part geometries and other measurements. This can be viewed in Appendix B, Table B.1. The air filters are relatively large to assist in keeping the flow velocity and pressure loss to a minimum. These are standard automotive filters adapted into the ducting system. The conical inlet is elevated so as to be out of the way of the exhaust gases as these can drastically affect inlet conditions.

3.3.2 Centrifugal Compressor

As stated previously the Rover 1S/60 gas turbine uses a centrifugal compressor to impart energy to the working fluid. The velocity of the fluid is transferred into pressure energy partially by the impeller and partially by the diffuser. Figure 3.5 depicts the Rover's impeller and diffuser from the single stage centrifugal compressor.

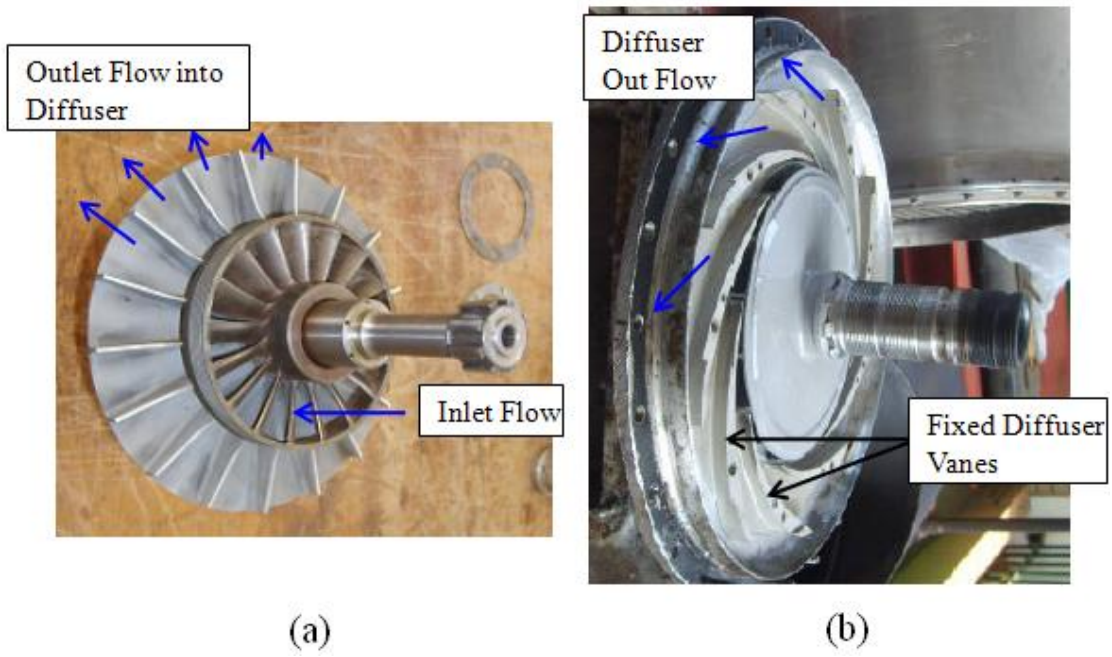

Figure 3.5: Centrifugal Impeller (a) and Diffuser (b)

The flow enters the rotating impeller in the axial direction and exits in a radial direction as indicated in the figure. The diffuser then slows the flow down and the pressure is increased. Geometric properties for the impeller and diffuser follow in Table 3.2.

Table 3.2: Rover 1S/60 Compressor Geometry

Geometry			
Impeller		**Diffuser**	
Number of Vanes	17	No. of Vanes	17
Diameter [m]	0.165	Diameter [m]	0.165
Vane Thickness [m]	0.00175	Radial Gap [m]	0.00175
Peripheral Depth [m]	0.00845	Exit Area [m^2]	0.00191

3.3.3 Combustor

The Rover 1S/60 utilises a single can-type combustor which is fed pressurised air from the compressor. In the combustor a fine spray of fuel (kerosene) is injected and ignited with the air. This rapid burning of the fuel heats the air to a temperature high enough so that the gaseous mixture can expand through the turbine blades. The combustor from the Rover 1S/60 can be seen in Figure 3.6.

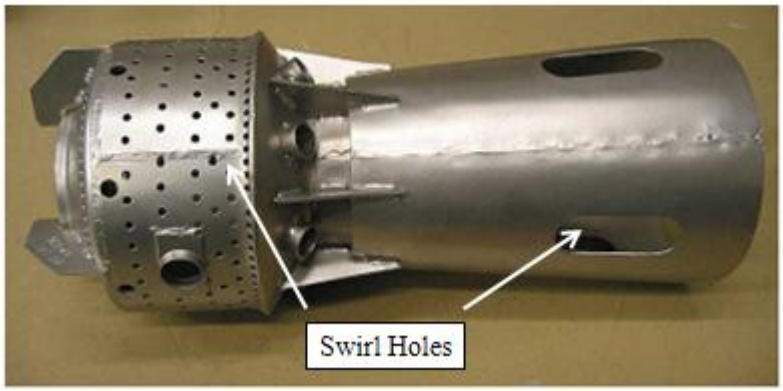

Figure 3.6: Combustor Liner for the Rover 1S/60.

3.3.4 Axial Turbine

A close-up view of the Rover's single stage axial flow turbine is shown in Figure 3.7 below. There is one set of stator blades and one set of rotor blades with all flow moving in an axial direction through the blades.

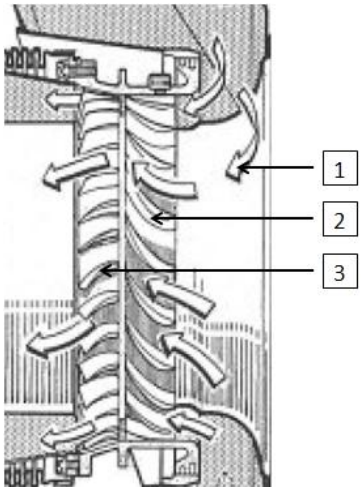

Figure 3.7: Close-up View of the Rover 1S/60 Axial Turbine. (Rover, 1966)

Where:

1 – Flow direction (I.e. From right to left, axially through the stator and rotor).

2 – Stator Blades or Nozzle Guide Vanes (NGV) Non – Rotational.

3 – Rotor Blades (Rotational part of the turbine driven by the expanding gas).

Putting this into context with respect to the actual parts of the engine, Figure 3.8 depicts the Rover parts using the same numerical correlation used in Figure 3.7 above. Here the rotor is mounted inside the housing of the stator and again the flow expands from right to left through the blades.

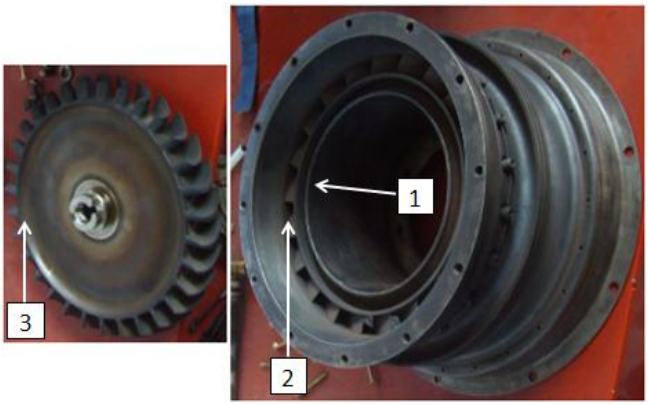

Figure 3.8: Rover 1S/60 Turbine Rotor and Nozzle Guide Vanes (Prinsloo, 2008)

These gases which expand through the turbine are a direct result of the combustion process and hence must be at a certain temperature (firing temperature) for the turbine to function efficiently. The higher the turbine firing temperature is, the higher the thermal efficiency of the engine will be. Material limitations in terms of strength and blade coatings prevent turbine inlet temperatures from being excessively high, hence this limits the thermal efficiency of the gas turbine unit from a turbine inlet temperature perspective. The maximum turbine inlet temperature for the Rover 1S/60 gas turbine is not specified by Rover (1966). It is assumed the inlet temperature is in the range of 750 - 800 °C, Roos (2008). Specific turbine geometries and data can be viewed in Table 3.3 and Table 3.4 respectively. Point 1 denotes the point just before the stator, point 2 is between the stator and rotor and point 3 is after the rotor.

Table 3.3: Turbine Cross Section Geometry

Turbine Cross Section Geometry			
	Point 1	Point 2	Point 3
Root Radius [m]	0.076	0.076	0.076
Tip Radius [m]	0.0881	0.0887	0.0943

Table 3.4: Turbine Data

Turbine Data		
	Stator	Rotor
Number of Blades	21	31
Pitch [m]	0.0246	0.173
Chord [m]	0.0410	0.236
Mean Blade Height [m]	0.124	0.155
Trailing Edge Thickness [m]	0.0008	0.0008
Tip Clearance [m]	0	0.0005

The turbine blades have a plain clearance and are not shrouded. Similar to the compressor, the turbine map is unavailable and one was generated from carrying out simulations based on the above geometries, see Chapter 4. The predicted efficiency was also ascertained from these simulations. The turbine exhausts into an exit diffuser which lowers the flow velocity and minimises the pressure loss. The geometries for the standard and modified exit diffusers can be seen in Appendix C.

3.3.5 Heat Exchanger

The shell and tube heat exchanger is of a counter-flow configuration, where the hot and cold streams flow in opposite directions to one another. This is shown in Figure 3.9. The red and blue arrows depict the temperature and flow directions of the hot and cold streams respectively. Heat transfer resultantly occurs through the tube walls from the hot exhaust gases to the cold pressurised air.

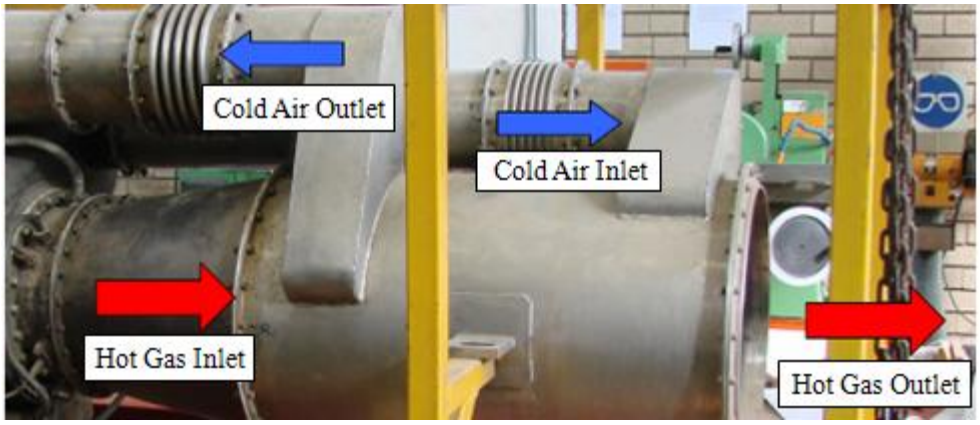

Figure 3.9: Shell and Tube Heat Exchanger Mounted on the Rover 1S/60

The hot gas inlet temperature is in the region of the continuous jet pipe temperature of 580 °C while the cold air inlet temperature is around 160 °C - 170 °C. Specific data pertaining to the heat exchanger can be seen in Table 3.5.

Table 3.5: Hot and Cold Side Data for Rover 1S/60 Heat Exchanger

Heat Exchanger Data			
Hot Side – Tubes		Cold Side – Shell	
Number of Tubes	271	Number Shell Passes	4
Tube Inner Diameter [m]	0.0106	Shell Diameter [m]	0.305
Tube Length [m]	0.5	Shell Length [m]	0.5
Tube Roughness [μm]	40	Shell Roughness [μm]	40
Wall Thickness [m]	0.00175	Shell Thickness [mm]	3
Material	Copper	Material	Steel
Thermal Conductivity [W/m.K]	401	Thermal Conductivity [W/m.K]	43

The actual effectiveness of the heat exchanger is unknown as during the design phase no documentation was completed and no information can be found on the design. However from the previous testing results (Appendix A) the effectiveness was in the region of 35% at 40000 rev/min. Full geometries for the heat exchanger can be seen in Appendix D.

All information with regard to the specific components presented in this section was used to build a model of each component in an attempt to simulate the entire gas turbine system.

3.4 Experimental Problems

As mentioned in section 3.2.1 Prinsloo (2008) conducted testing on the Rover 1S/60 gas turbine in 2008. Prinsloo (2008) re-commissioned the entire gas turbine engine by disassembling all components for examination and then reassembling them to conduct operational tests. Numerous problems were encountered during these tests and are listed below:

- The fuel sprayer nozzle was found to not be atomizing the fuel correctly.
- The throttling valve leaked excess fuel and was found to deteriorate continuously through testing. This resulted in the engine dying off due to the lack in fuel pressure.
- The original Rover engine was designed to run a simple cycle without heat exchange and due to the modifications of adding a heat exchanger and creating a regenerative cycle, the combustor inlet temperature was significantly higher which may have had a negative effect on the combustion process.
- The starter motor overheated and fuel would build up in the turbine exhaust due to numerous failed starts. The fuel build up was caused due to the addition of the heat exchanger which resulted in explosive combustions during startup.
- Total testing time was limited to 30 seconds due to over speeding and the aforementioned fuel problems.

In 2009 Phakathi (2009) performed a research investigation into the fuel system of the Rover 1S/60 gas turbine. As previously stated in Section 3.2.1, the fuel system was removed, which included the fuel nozzle and sprayer assembly as well as the fuel pump, and testing was conducted. A separate test rig was constructed and the fuel system components were tested such that they were isolated from the Rover 1S/60 gas turbine engine. Phakathi (2009) concluded that the fuel sprayer as well as the fuel pump were both in adequate working condition and proposed that a detailed investigation be conducted on the combustor. This detailed investigation was to be conducted by the CSIR during 2010. However no investigation has been conducted. The works of Prinsloo (2008) and Phakathi (2009) remain the only available documentation pertaining to the Rover 1S/60 overhaul.

An effort was made to conduct stand alone tests on the heat exchanger component of the Rover 1S/60 gas turbine in order to determine its effectiveness. The heat exchanger was

detached from the gas turbine and a support stand was designed and manufactured on which to place the heat exchanger for testing. The test setup was planned to consist of standard sections of detachable threaded pipes in conjunction with a gas burner to make up the heating circuit responsible for playing the role of the combustor. Further piping as well as a small fan would provide the air mass flow rate through the test rig. Figure 3.10 shows a CAD representation of the proposed setup. However due to time limitations and equipment availability no testing was conducted.

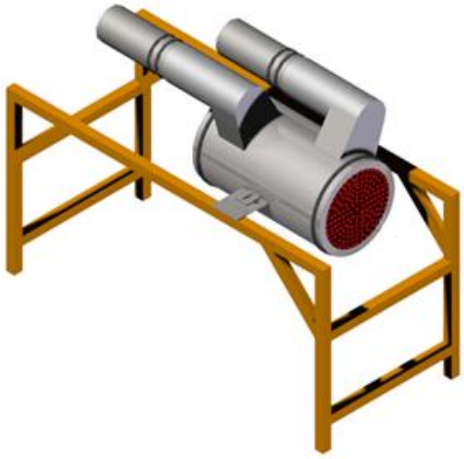

Figure 3.10: CAD Representation of the Heat Exchanger Test Setup

It was then thought to test the Rover 1S/60 in its original configuration without the heat exchanger. This required some modifications to reset the changes created by the addition of the heat exchanger. Along with these necessary changes was the uncertainty that the combustor had still not been investigated.

Thus due to the aforementioned combustor issues, and no investigation ever being conducted on the combustor, as well as the fact that the overhaul of the engine was not within the scope of this research, the Rover 1S/60 gas turbine remains inoperable. Furthermore no testing was completed due to the abovementioned unforeseen constraints, funding issues and time limitations imposed by the CSIR.

4 System Modelling for Simulation

This chapter begins by describing the software package used for the numerical simulations and follows by outlining a broad simulation methodology. Detailed simulation methods are then discussed for the specific modelling of individual components within the system. The chapter concludes with overall simulation models for each of the various systems.

4.1 Software

Numerous simulation software packages are available which are specifically designed to model solar thermal power plants. These packages are targeted at the solar part of the power plant which involves simulating the heliostat tracking system and the amount of solar radiation which is captured. The actual power block component, Rankine or Brayton cycle, is also addressed but in less detail. An example is a package such as TRNSYS (2011) discussed in Chapter 2 and used by Romero, et al. (1999) to analyse the performance of a solar receiver.

For the current research it was not necessary to simulate the solar tracking part of the system but rather to characterise the gas turbine cycle and peripheral components. Thus a software package was required that had the capability to thoroughly analyse turbomachinery components while at the same time allowing the user freedom to add and analyse additional components into the system, such as thermal storage and solar receiver. After outlining the various characteristics of the simulation packages available for the study and looking in particular at their ability to handle turbomachinery components, the following was discovered. The ‘Flownex’ simulation package, Flownex (2010), provided a network approach of interconnected elements joined together to create a flow system. Particular turbine and compressor components are available to allow any power generation network to be created in great detail. Thus Flownex was chosen by the CSIR to best answer the research question as it allowed for a more comprehensive analysis of the gas turbine part of the system

while still providing the necessary freedom to custom-define the solar components in the system. Flownex is discussed in further detail in the following section.

4.1.1 Flownex Simulation Environment

The Flownex simulation package was provided by ESTEQ (2009). Flownex is a systems CFD (Computational Flow Dynamics) code which allows for the design, analysis and optimisation of various thermal-fluid systems. The term “Systems CFD” refers to the methodology where multiple components of varying degrees of complexity are connected together in a network to represent a complex system, Flownex (2010). The version of Flownex that was used for this research report was version 8.0.13.

The software is locally developed in South Africa by M-Tech Industrial (2008). The model’s solver uses the governing equations of both thermodynamics and fluid dynamics along with empirical formulae for specific components to allow the user to build and solve complex thermal-fluid networks. The actual construction of the network is done via elements and nodes, the former being the actual components involved in the system while the latter are the links used to connect these various components together. Boundary conditions are used to specify temperatures and either pressures or mass flow rates at inlets and outlets of the system. Figure 4.1 illustrates a basic Flownex network.

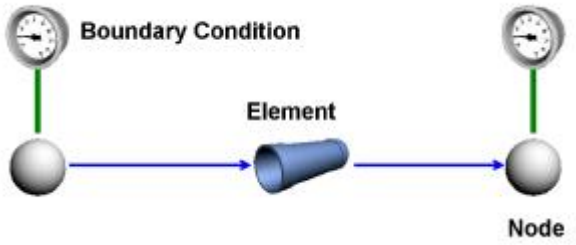

Figure 4.1: Example of Flownex network. (Flownex, 2010)

The solver is based on an implicit pressure correction method (IPCM) which solves the conservation of momentum at each element as well as continuity and energy equations at each node. Hence the code is described as having a pseudo CFD capability in that it can predict temperature and pressure gradients, Landman and Greyvenstein (2004). Flownex can perform both steady state and transient analyses, thus allowing the user to first develop a

stable model of the system and then run a transient simulation where the user can physically interact with the system while it is running. This allows for endless scenarios which the user can initiate, such as the turning on/off of a pump, the closing of a valve, increasing/decreasing a fuel flow rate etc. Flownex has built-in component libraries which include many types of thermal fluid components such as piping, ducting, valves, fans, compressors, turbines, pumps, heat transfer elements and heat exchangers. The package also incorporates a variety of different control elements, such as PID controllers which can be used in a complex transient network to create feedback loops in order to control various outputs and inputs. Results of simulations can be viewed using interactive graphs, dials and gauges as well as colour coded result layers. Figure 4.2 shows an example of a thermal fluid network with multiple components.

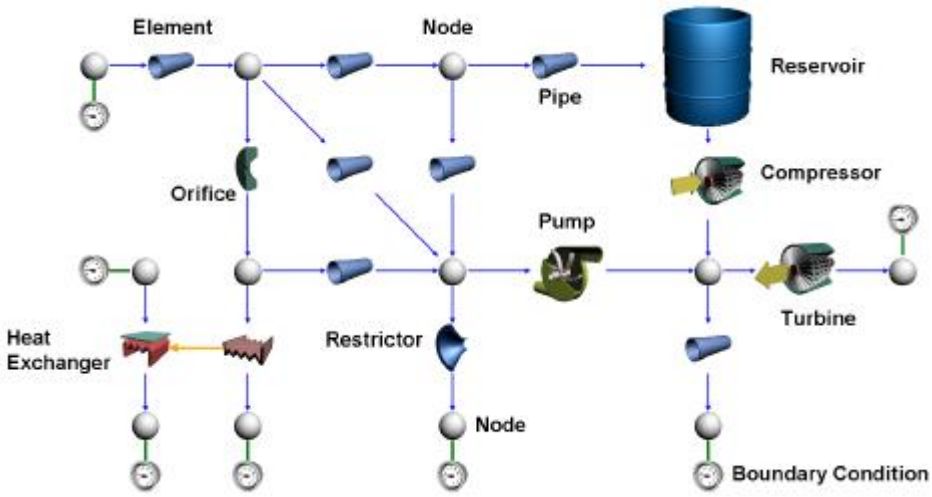

Figure 4.2: Schematic representation of a thermal fluid network (Flownex, 2010)

Industry applications for Flownex include power generation, gas and oil industries, mining, shipping, aerospace, air conditioning and water reticulation systems.

For the current study the following options were used in Flownex: the ability to create user-defined characterisation maps for the turbine and compressor components, the built-in shell and tube heat exchanger component with user defined specifications in order to compare and characterise the actual Rover1S/60 heat exchanger, and finally the conductive and convective heat transfer components to be able to model the thermal storage. Flownex also has the ability to define fluids and create mixtures of multiple fluids, such as air, kerosene and carbon dioxide for combustion applications.

4.2 Simulation Methodology

4.2.1 General Gas Turbine Model

In order to understand the design point (steady state) operating conditions of the Rover 1S/60 gas turbine, spreadsheets were created of the basic Brayton cycles for both the standard Rover engine and the modified engine with recuperator. Table 4.1 displays the relevant data used in generating the spreadsheet results.

Table 4.1: Relevant Data for Spreadsheet Models

Relevant Data			
Compressor Pressure Ratio	2.8	Compressor Eff. (Isentropic) [%]	70.5
Gas Constant [J/kgK]	287.05	Turbine Eff. (Isentropic) [%]	84.8
Air Mass Flow Rate [kg/s]	0.518	Combustor Eff. [%]	99
Fuel/Air Ratio (Standard)	0.01604	Mechanical Eff.[%]	99
Fuel/Air Ratio (Modified)	0.01223	Fuel Heating Value [MJ/kg]	43.1
Combustor Pressure Loss [%]	6.1	HE Hot Side Pressure Loss [%]	2
HE Cold Side Pressure Loss [%]	2	HE Assumed Effectiveness	0.30

Standard atmospheric pressure and temperature were taken as 87.6 kPa and 20 °C for conditions in Pretoria. The air mass flow rate was recalculated for Pretoria and found to be 0.518 kg/s. The continuous JPT (Jet Pipe Temperature) is stated as 580 °C (850 K), (Rover, 1966), and this resulted in a necessary TIT (Turbine Inlet Temperature) of 756.15 °C (1030 K), for the assumed first estimate of turbine efficiency of 84.8%. The turbine efficiency was found using the known turbine blade geometries and a method set out in Cohen et al (2001) (discussed further in Section 4.2.4). Calculations are based on empirical formulas for gas turbine cycles from Cohen et al (2001). The heat exchanger effectiveness of 30% was attained from Prinsloo (2008) whereby an iterative approach was followed using effectiveness values of 30%, 40% and 50% and calculating the system's thermal efficiency and net power output based on empirical calculations. Prinsloo (2008) found that an effectiveness of 30% yielded a thermal efficiency of 12.6%. This was confirmed through the

analysis described in Figure 4.3 and Figure 4.4 which illustrate the basic Brayton cycle layout for the standard and modified Rover 1S/60 engine respectively. Temperature and pressure data for each of the points numbered in the figures can be seen in Appendix E.

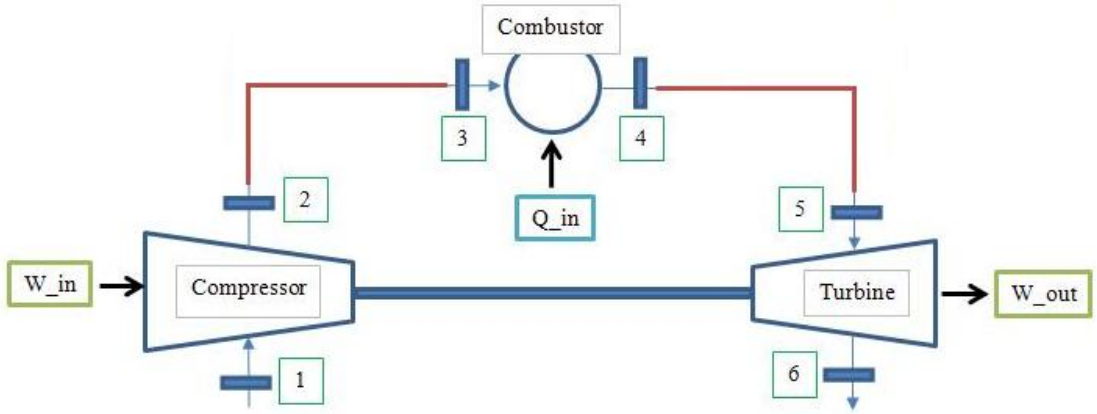

Figure 4.3: Brayton Cycle Layout of Standard Rover 1S/60.

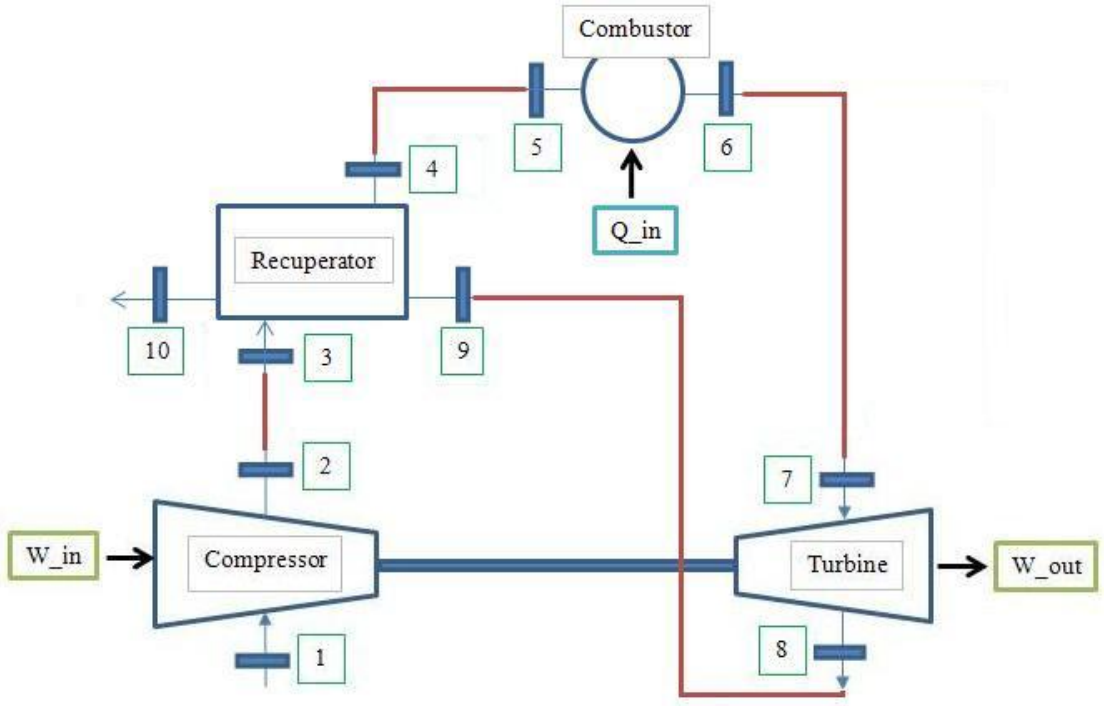

Figure 4.4: Brayton Cycle Layout for Modified Rover 1S/60 Engine.

The standard Rover 1S/60 yields a net work of 37.59 kW and thermal efficiency of 10.61%. For the modified Rover engine a recuperator was introduced with an assumed first approximation effectiveness of 30%. The modified engine gives a net work output of 34.99 kW and thermal efficiency of 12.94%. The overall net work is seen to be lower than the rated

45 kW as this analysis assumes operation at altitude. The thermal efficiency is slightly higher for the modified engine which is expected due to the presence of the recuperator.

These first approximation results give a preliminary idea as to the running of the engine in terms of temperatures and pressures at different points. This assisted in error checking for the more complex models to understand when a variable was outside the limits of a realistic value.

4.2.2 Intake System Model

The intake system consists of multiple steel ducts of varying inlet and outlet cross sections. These are best modelled in Flownex through the use of pipe elements. Standard circular parts are modelled using direct dimensions for their inlet and outlet diameters, while for the non-circular sections hydraulic diameters are used for the respective inlets and outlets. There are three bends in the design where the air flow changes direction (Figure 3.4). These are modelled using the bend component and specifying a mean bend radius as well as a bend angle. However it was decided that the bend where the automotive filter is present is best modelled by two variable area diffusers in the form of pipe elements. This was done to avoid using two bend components of 45° each and incurring unwanted secondary losses from the bend component. Hence the upstream diffuser would have a smaller inlet area and larger outlet area equal to that of the frontal area of the automotive filter. The downstream diffuser would then have an outlet diameter equal to the size of the next ducting section.

The difficulty was in obtaining a correct pressure drop correlation for the automotive filter so that simulation results would accurately depict experimental ones as the system mass flow rate varied. As the automotive filter was obtained from a local mechanic no pressure drop data were known and no curve could be obtained from the manufacturer. To address this issue a graph of pressure drop across the intake system was obtained from the results of Prinsloo (2008) bearing in mind that the intake system was only instrumented with pressure transducers at the conical inlet and just before the compressor inlet. From this graph, data for a curve was fitted using a program called GetData (2011). The original graph and corresponding GetData plot are shown in Figure 4.5.

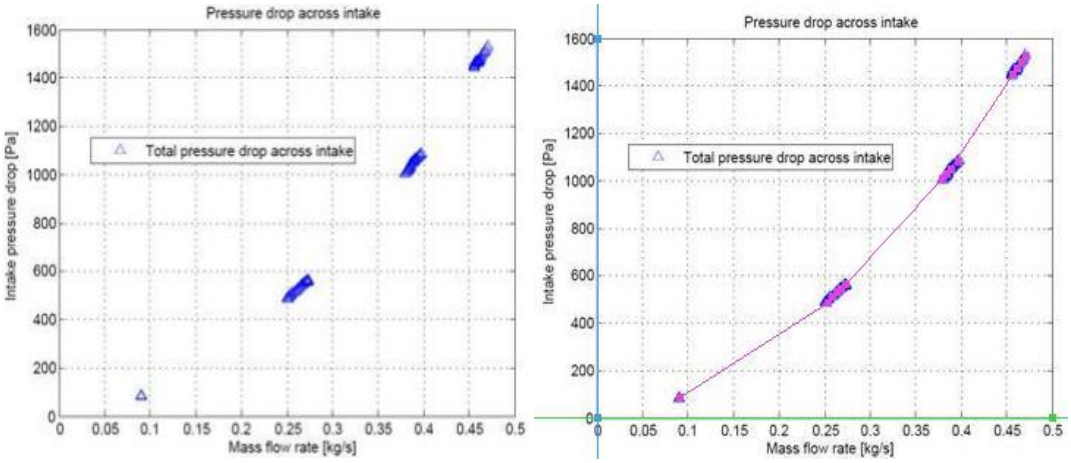

Figure 4.5: Pressure drop correlation curve for intake system.

Following this a Flownex model was created of the intake system excluding the air filter. The model was run at steady state conditions for all the air mass flow rate values from Figure 4.5 and the total pressure drop through the system was recorded via an Excel component and displayed on the screen. The model is shown in Figure 4.6 below.

With this data a first idea of the pressure drop through the air filter could be attained by subtracting the no filter, Flownex model pressure drop from the intake pressure drop in Figure 4.5. These results are illustrated in Figure 4.7. Pressure drop results for each air mass flow rate can be seen in Appendix F, Table F.2.

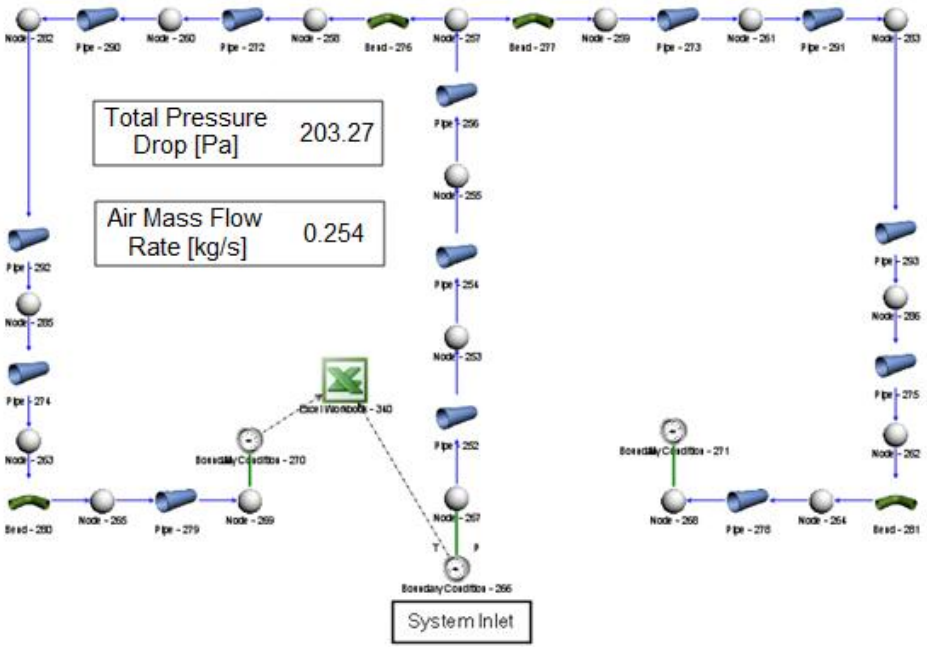

Figure 4.6: Flownex Intake System, No Air Filter

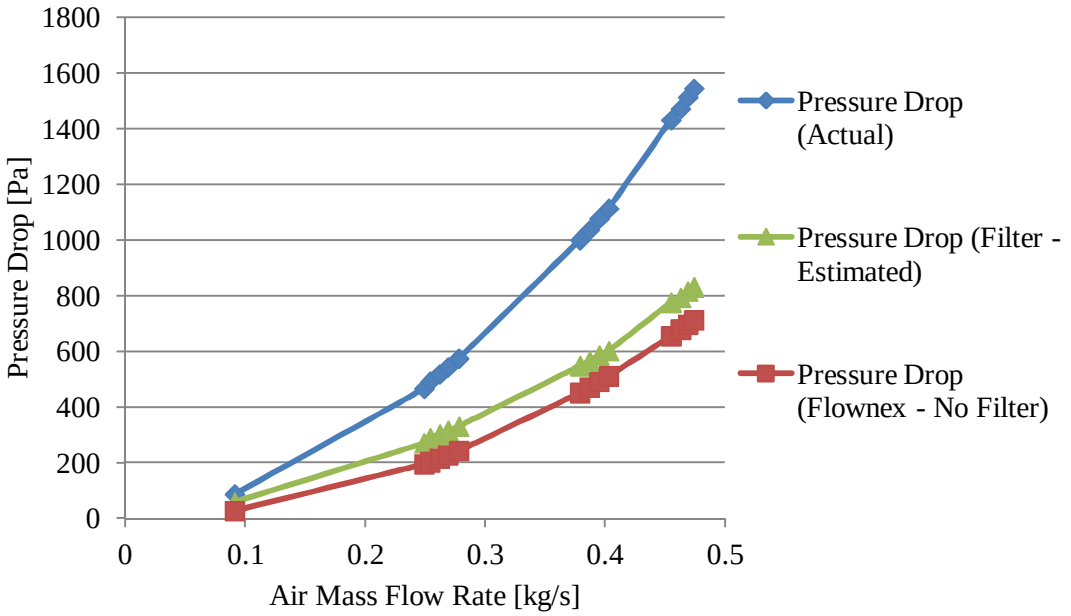

Figure 4.7: Pressure Drop Variants vs. Air Mass Flow Rate

In order to simulate the air filter a pipe element was used. The pipe element in Flownex allows both forward and reverse loss coefficients to be specified. Hence using the data from Figure 4.7 a forward loss coefficient was calculated and specified for the Flownex air filter so that it correlates with the pressure loss through the actual air filter.

From the mass flow rates of Figure 4.7 volumetric flow rates were calculated. Engineering drawings of the intake system allowed for the frontal flow area of the automotive filter to be calculated at 0.047 m^2. Hence using this and the volumetric flow rate an air velocity could be obtained. Combining the air velocity and the pressure drop formula of $\Delta P = K\frac{1}{2}\rho V^2$ the $\Delta P/V^2$ term was found using the filter pressure drop from Figure 4.7. Next the actual pressure drop through the filter, ΔP, was calculated by taking the $\Delta P/V^2$ value for the highest air mass flow rate of 0.474 kg/s and multiplying it by the square of the air velocity. This results in a theoretical pressure drop through the air filter, found using the highest air mass flow rate. This means that the pressure drop at lower mass flow rates will be overestimated, however the system runs primarily at the higher air mass flow rates. The technique explained above is used only as a check to see how the percentage error between the two pressures varies with mass flow rate. Table F.1 in Appendix F displays the two pressure drops as well as the percentage error between them. Note how the percentage error at higher mass flow rates is much lower due to the high mass flow rate correlation used.

A loss coefficient (K value) was attained using the same $\Delta P = K\frac{1}{2}\rho V^2$ formula. This calculated to be 19.83. This loss coefficient was then incorporated into a second Flownex model of the intake system and steady state tests were once again run. Figure 4.8 shows an example of the Flownex system including the air filters.

The total system pressure drop and air mass flow rate was displayed on the screen and then compared with the original pressure drop through the intake system from Figure 4.5. Table F.3 in Appendix F shows the two pressure drops as well as their percentage error from one another. Again it can be seen at medium to high mass flow rates the percentage error is very low (<1%) and the two pressure drops correlate closely. This is illustrated in Figure 4.9 where the Flownex results correlate well with the measured pressure drop results of Prinsloo (2008). The deviation between the two curves is slightly greater at the lower air mass flow rates, however these low flow rates only occur during start up conditions thus this discrepancy is not highly important.

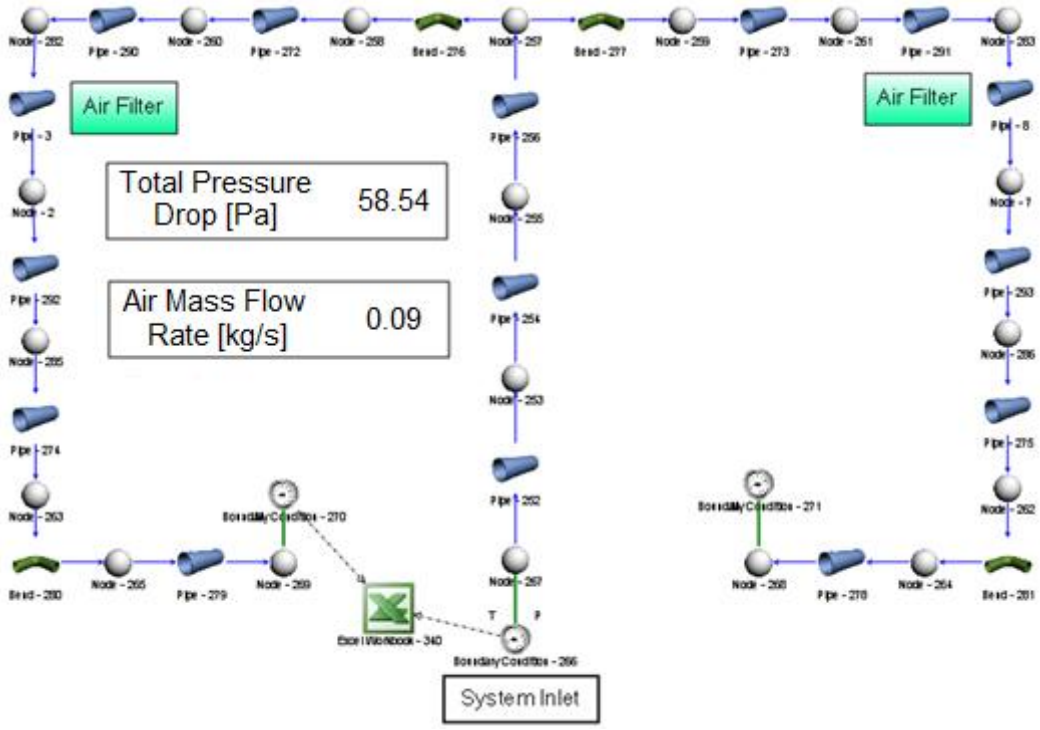

Figure 4.8: Flownex Intake System with Air Filter

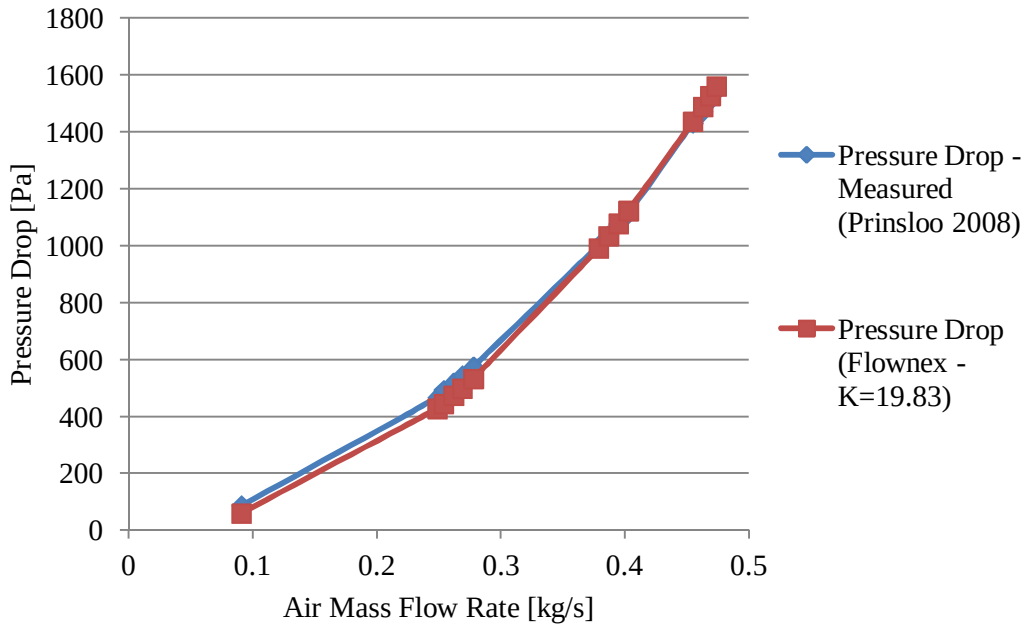

Figure 4.9: Actual and Simulation Pressure Drop vs. Air Mass Flow Rate

A second approach to the determining the pressure difference across the intake system involves the use of the General Empirical Relationship element in Flownex. This element is governed by the equation $\Delta P = C_k \rho^{\beta} Q^{\alpha}$. Where C_k, β and α are pressure drop constants, ρ is the mean density at static temperature and pressure and Q is the volumetric flow rate.

As a first approximation for a selected volumetric flow rate and known pressure drop, take $\beta = 1$ and $\alpha = 2$ and calculate the C_k value. Following this the β and α terms can be varied and knowing the density of the air, the pressure drop can be attained for each corresponding volumetric flow rate. However this approach was not used due to the first approach providing satisfactory pressure drop results across the intake for each flow rate with only insignificant errors apparent at lower flow rates.

It should be noted that when using the General Empirical Relationship the following is assumed:

- One dimensional flow exists at the inlet and the outlets.
- No work is done on the fluid.
- Thermal and mass inertia is neglected.
- The actual volume contribution of the element is assumed to be negligible compared to the volume of the system.

4.2.3 Combustor Model

In order to model the combustion process for the gas turbine system the Adiabatic Flame element was used in the Flownex Program.

The adiabatic flame element calculates the off-gas composition and maximum temperature for a chemical reaction of a specified chemical mixture. The off-gas mole fractions and maximum temperature is calculated by a secondary program NASAGlenn chemical Equilibrium Program CEA2, also known as the Gordon McBride Program. Flownex populates the input file by retrieving the reaction pressure, inlet temperature, mass fractions and reactant names of the reactants for the upstream node. The Gordon McBride program then uses this Flownex generated input file to generate an output file. Flownex then retrieves the mass fractions of the reaction products as well as the off-gas temperature and returns these values to the downstream node, Flownex (2010).

When using the Adiabatic flame element the following assumptions apply:

- The combustion takes place at constant pressure
- There are no radiation effects.

Additional to these assumptions it should be noted that the Gordon-McBride program does not account for the geometry of the combustion chamber, hence the off-gas temperature is calculated by assuming radiation and heat transfer affects are negligible. However the adiabatic flame element is used in such a way that it is connected in parallel with a pipe component. This allows the combustor geometry to be modelled using this pipe component. Figure 4.10 shows a simplified version of the combustion model. The acronyms MSF located next to each of the inlet boundary condition denote Mass Source Fractions for the air and fuel inlets respectively. This system shows the air boundary condition for simplicity reasons, but in reality this boundary condition does not exist as this comes from the exit of the cold side of the recuperator.

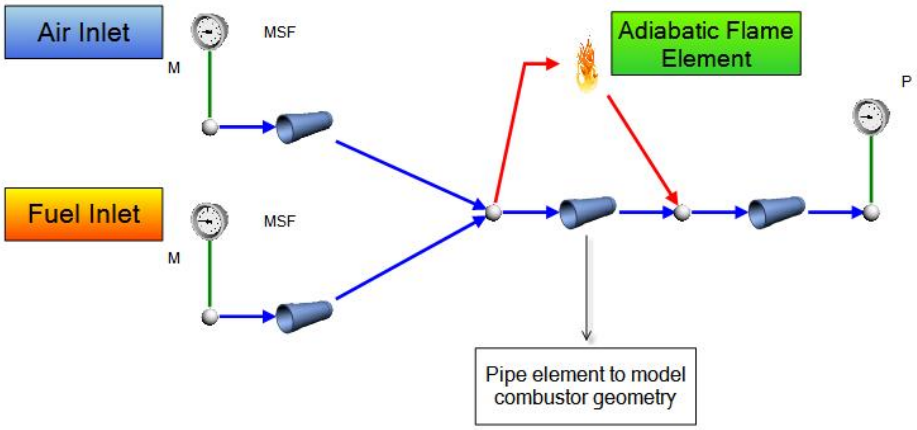

Figure 4.10: Flownex Combustion Model with adiabatic flame element

As in reality with any gas turbine unit air is compressed and enters the combustor, fuel is added to the air, the mixture combusts and exhaust gases expand through the turbine. The model shown in Figure 4.10 uses two separate boundary conditions to simulate the air inlet and the fuel inlet. A mixture is defined which incorporates all reactants and products necessary for the combustion to occur. These include Air, Argon, Carbon Dioxide, Water Nitrogen, Oxygen and Kerosene as the fuel. All the necessary elements and compounds were selected from built in libraries in Flownex. Initially kerosene was defined as a liquid, however a problem was encountered in that Flownex was not able to accommodate a mixture of fluids in different phases hence the kerosene had to be modelled based on an ideal gas. This option was available within the program to specify the fluid to behave as an ideal gas with the user defined properties of the fluid's viscosity, conductivity and specific heat based on tables from Cohen et al (2001). As this approach was not ideal in terms of defining Kerosene as an ideal gas another approach was chosen and suggested by ESTEQ (2009). This was to use propane as the fuel for the combustion process as this has proven examples and accurate results. Hence this approach was selected. Finally the reaction products from the combustion process are determined by the NASAGlenn Chemical Equilibrium Program CEA2 as mentioned previously.

4.2.4 Turbine Map

A number of steps were taken in order to develop a suitable turbine map that could be used in the Flownex program. The first undertaking involved using the known geometries for the

turbine blades and following a method outlined in Cohen et al (2001). The method estimates the performance based on flow conditions at the mean diameter of the annulus and allows the theoretical turbine stage efficiencies to be calculated. The turbine of the Rover 1S/60 is a single stage unit and hence the polytropic and isentropic efficiencies are the same. The efficiency was found be around 85.7 %, full calculations for this can be seen in Appendix G. The method also provides a means of calculating the outlet gas angle for the stator and rotor. These angles are necessary inputs for a one-dimensional solver code developed by the Northern Research Engineering Corporation, NREC (1972), currently known as Concepts NREC. There are two separate parts to the NREC code which are used, the first being called Turbine Design Mean Line (TDML) and the second, Turbine Performance (TPERF). The codes are used in unison by taking outputs from TDML and using them as inputs in TPERF to generate speed lines and turbine maps.

The TDML code was used in an iterative manner in order to obtain the correct stator exit angle, calculated as α_2 in Appendix G. This was done by varying the inlet swirl velocity and then running the program to ensure that the output for the stator exit angle matched the value computed in Appendix G. The next step involved changing the stage power developed in order to match the relative rotor exit angle (β_3) to the one determined from the same method above. Once these two parameters had been correctly matched, and the code run again, the results file then yielded the inlet rotor angle (β_2). This angle was then entered as an input into the TPERF program and once the program was run it generated speed lines at various engine speeds. For each respective code the input data can be seen in Appendix H.

Result data for each speed line was viewed in a text file. For each speed line there are various factors calculated such as total mass flow rate, pressure ratio and efficiencies. Flownex requires four main types of data in order to create a turbine map. These are the pressure ratio, efficiency, corrected mass flow ($\dot{m}\sqrt{T_{01}}/P_{01}$) and corrected speed ($N/\sqrt{T_{01}}$). Extracting these data from the text file and entering them into the turbine chart editor reveals the following two graphs seen in Figure 4.11 and Figure 4.12. Note that the efficiency and pressure ratio data have been split onto separate graphs as this is how they are utilised by Flownex. These turbine maps were then used in the Flownex model.

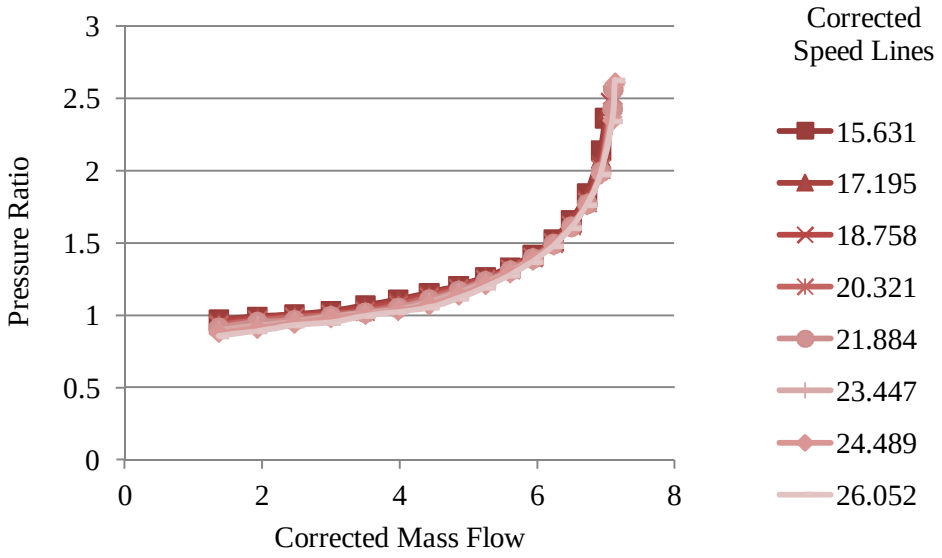

Figure 4.11: Corrected Mass Flow vs. Pressure Ratio, Rover 1S/60

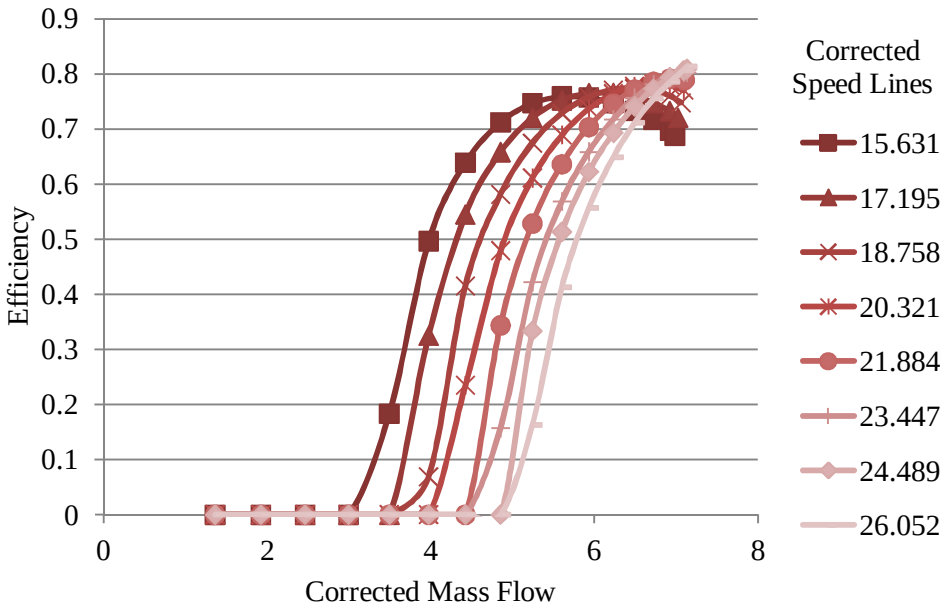

Figure 4.12: Corrected Mass Flow vs. Efficiency, Rover 1S/60

Further to the development of the turbine maps, compressor maps had to be created to incorporate into the model. However unlike the turbine there was no code available, other than detailed CFD modelling in a package such as NUMECA, which allowed for the creation of compressor maps from the compressor geometry. Due to initial time constraints the detailed CFD modelling could not be completed and alternate methods were pursued.

A set of spreadsheets were obtained from M-Tech Industrial (2008) that contain imaginery turbine and compressor characteristics that can be scaled in the case that no turbomachinery geometries are available. The Excel spreadsheet is specifically designed to generate turbomachinery maps in a Flownex compatible format. The spreadsheet was created from empirical formulae and generates compressor maps based on user inputs for corrected speed, corrected mass flow, pressure ratio, efficiency and inertia. Input values for these spreadsheet maps were calculated from Equations (2.2) and (2.3) and the results are shown in Table 4.2. Note: the corrected speeds and mass flow rates were calculated for the engine operation in Pretoria.

Table 4.2: Compressor Input Values

	Compressor Input
Corrected Speed	44.77
Corrected Mass Flow	10.19
Pressure Ratio	2.8
Efficiency	0.71

It should be noted that while this approach is not ideal, as these spreadsheets allow for the Rover 1S/60 compressor to be scaled based on an imaginary compressor using the operational parameters listed in Table 4.2 rather than based purely on the compressors geometry, the method does allow the Rover's compressor to be represented with reasonable accuracy in order to provide results for the simulation.

In order to create these compressor maps from the aforementioned M-Tech Industrial (2008) spreadsheet, it was necessary to know the compressor efficiency, shown as 0.71 in Table 4.2 previously. This efficiency was calculated for design point operation, using the measured geometric properties of the impeller (Table 3.2) as well as the known air mass flow rate and pressure ratio from Rover (1966) along with empirical formulae from Cohen et al (2001). Firstly from Cohen et al (2001) the work done on the air by the compressor is given by $W = \psi\sigma U^2$ where ψ represents the power input factor, set as 1 in this case thus neglecting compressibility effects and disc friction or "windage" losses around the impeller vanes, σ is the Stanitz slip factor for the impeller and U is the tangential velocity at the periphery of the impeller. The Stanitz slip factor (σ) was found using the formula $\sigma = 1 - 0.63\pi/n$ where n

represents the number of impellor vanes, found in Table 3.2. The tangential velocity *U* at the periphery of the impeller was found using the known impeller diameter from Table 3.2. Since no energy is added to the air in the diffuser, the stagnation temperature rise across the whole compressor is equal to the temperature rise across only the impeller. Thus $T_{03} - T_{01} = T_{02} - T_{01} = W/c_p$, with c_p denoting the specific heat of air and T_{01} the ambient temperature of the air at the compressor inlet. This then reduces to $T_{03} - T_{01} = \psi\sigma U^2/c_p$ where T_{03} was calculated to be 153.42 °C. Finally from Cohen et al (2001), Chapter 4 equation (4.5), the overall pressure ratio is given as:

$$\frac{P_{03}}{P_{01}} = \left(1 + \frac{\eta_c (T_{03} - T_{01})}{T_{01}}\right)^{\frac{\gamma}{\gamma - 1}} \tag{4.1}$$

Thus knowing that the pressure ratio (P_{03}/P_{01}) at the design point is 2.8, an iterative approach was taken by guessing the compressor efficiency (η_c) until the above equation yielded a pressure ratio of 2.8. The compressor efficiency which yielded this was calculated to be 70.93 %. This efficiency was then used to generate compressor maps from the M-Tech Industrial (2008) spreadsheet in order describe the compressor's behaviour in the Flownex network. The Compressor maps are shown in Appendix I.

Finally a value for the shaft inertia was required as an input in Flownex on the shaft component which connects the turbine and the compressor. This was obtained from a CAD model created from neutron tomography tests done on the rotating parts of the turbine. The neutron tomography was done by RLQDesign (2009). Figure 4.13 shows the shaft and rotor assembly of the Rover 1S/60 as well as the neutron tomography image created of the shaft.

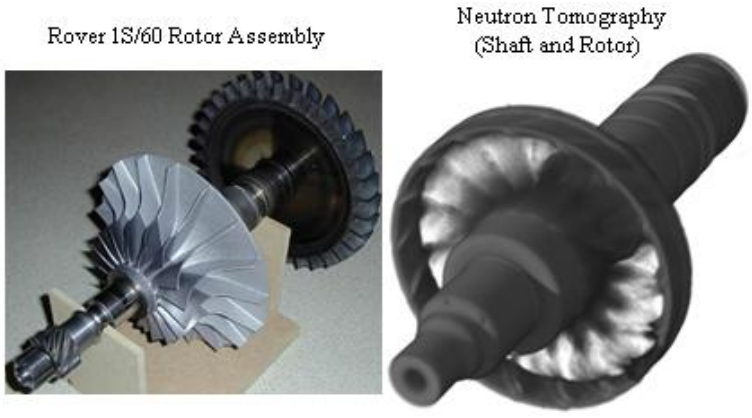

Figure 4.13: Rover 1S/60 Shaft and Rotor Assembly with Neutron Tomography Image (Bennet, 2011) and (RLQDesign, 2009)

During steady state simulations the shaft speed was specified so that other parameters such as mass flow rates and overall system behaviour could be analysed at a specific operating point. However during transient simulation the shaft speed was unspecified and the system just left to run, hence the engine speed was determined directly from throttling the fuel flow rate.

4.2.5 Heat Exchanger Model

The first step taken to simulate the heat exchanger involved calculating how much heat transfer would occur between the exhaust gases and the compressed air as well as attaining a theoretical effectiveness. The effectiveness-NTU method was chosen. Specific calculations can be seen in Appendix J. For the turbulent internal flow, inside the hot exhaust tubes, the Dittus Boelter correlation was used, while for the external flow of the compressed air over the tube bank a correlation was used from Incopera and DeWitt (2002) for flow across tube banks. Results yielded the heat exchanger effectiveness to be 34.97% and the heat transfer 76.99 kW, see Table 4.3. Figure 4.14 describes the shell side flow over the tube bank arrangement of the heat exchanger.

Following this a model was created in Flownex using a basic heat transfer element and two separate pipes, shown in Figure 4.15. The top pipe carries the hot exhaust gases and the bottom pipe the cold compressed air. The pipes were modelled based on the geometries of their respective heat exchanger components. The pipe component which represented the hot exhaust gases was given the geometry and material properties of a single tube in the heat exchanger and then specified to have 271 tubes in parallel so as to simulate the entire tube.

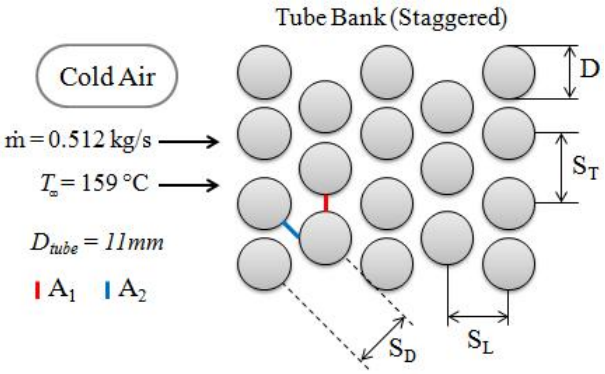

Figure 4.14: Tube Bank Arrangement Sample

Similarly the pipe component representing the cold compressed air was given material properties and geometries of the shell side of the heat exchanger. Inputs for the heat transfer component were set as follows. For conduction the upstream pipe areas were used (those of the exhaust gases) and geometry and material data were entered. The flow configuration is set to counterflow. For convection criteria, the downstream convection area was specified to that of the external area of the tubes and the heat transfer coefficient was set to 115 W/m^2K, matching the heat transfer coefficient calculated from empirical formulae given in Appendix J. The effectiveness was found to be 34.3 % and the heat transfer between the fluids 81.44 kW. The results are given in Table 4.3.

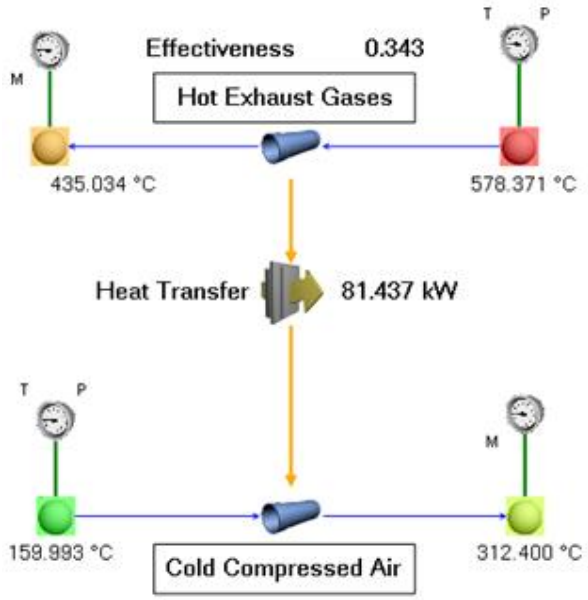

Figure 4.15: Heat Exchange with Heat Transfer Element

Following this a second model was developed in Flownex for comparison with the first model (Figure 4.14), this time using the built-in shell and tube heat exchanger components. The component has two parts, namely the shell side component and the tube side component. Inputs for the shell and tube component included material data which was selected from a database, geometric data such as number of passes, number of tubes per pass, as well as the tube length and diameter. Shell side data included the shell diameter and shell length, void fraction and shell inlet position. The model is shown in Figure 4.16 below. Again here a result layer was used to give a graphic representation in the form of colours to represent the various temperature differences at each node.

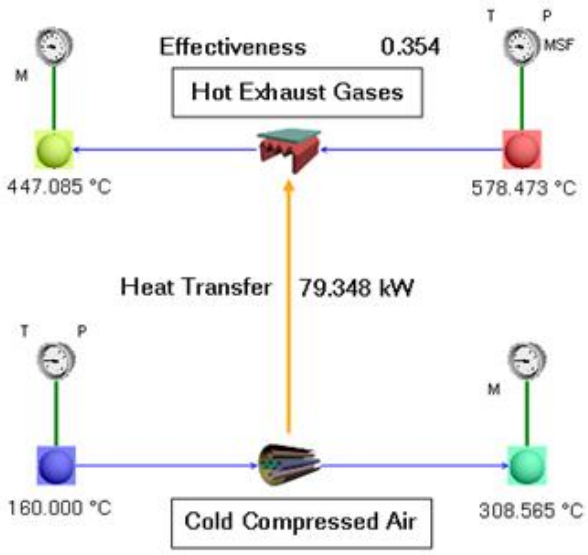

Figure 4.16: Heat Exchange with Shell and Tube Heat Exchanger

For the shell side component the shell inlet position was set using the Flownex help files such that the component would behave in a counterflow manner as it is with the heat exchanger in reality. The heat transfer area was specified as is seen in Appendix I as well as the heat transfer area ratio. The material was selected to be plain carbon steel and the mass specified. The mass was calculated based on the volume of material present and material density. Flownex specifies a wall heat transfer co-efficient and heat capacity depending on this.

However due to the unusual nature of the tube bank layout of the modified Rover's heat exchanger, correlations were created in order to best suit the Rover's tube bank layout with one available in Flownex. Firstly geometric measurements were taken for geometries of the Rover's heat exchanger, these can be seen in Appendix D Figure D.2. Next the Flownex heat transfer and friction factor data for the tube bank layout from Kays and London (1984) were measured and categorised according to the following geometric factors: tube inner diameters, mean-line spacing between tubes, area ratio (tubed area to non-tubed area) and tube density. This is shown in Appendix D, Table D.1. The measurements were necessary as the curves and tube geometries from Kays and London (1984) are staggered in their orientation, whereas the tube arrangement for the modified heat exchanger is in a concentric circle layout as seen in Appendix D, Figure D.2. Looking at the measurement results from Appendix D, Figure D.2 and Table D.1, it was found that the *s1.5 -1.0* tube set had the closest correlation in area ratio as well as almost identical mean-line spacing; hence this data set was selected to be used in the shell and tube heat exchanger in Flownex.

The model in Figure 4.16 yielded an effectiveness of 35.4 % and heat transfer of 79.35 kW. Table 4.3 shows the summarised heat exchanger results for the various models. When comparing the shell and tube model results to the results of the heat transfer element model in Figure 4.15 it is evident that both the effectiveness and heat transfer results correlate well. With regard to the empirical formula calculation in Appendix I both the effectiveness and heat transfer values correlate very closely to the results seen from both the Flownex models. Slight differences in the results between the Flownex models (Figure 4.15 and Figure 4.16) are attributed to the way the geometries were set in each of the models, in terms of the 271 tubes stipulated in parallel for the pipe element used in Figure 4.15 to model the tube bank arrangement, versus the pre-selected tube bank layout and heat transfer data from Kays and London (1984) used in the shell and tube element of Figure 4.16. Similarly variations seen in the results for the NTU calculations are caused from these geometry differences. For all models the same heat transfer coefficient was used and the air mass flow rate was 0.518 kg/s to simulate the design speed (46000 rev/min) operating conditions in Pretoria. The decision was made to use the shell and tube model for the overall system for simplicity reasons as well as the fact that the inputs to the shell and tube component allow the user to best represent the geometry of the actual heat exchanger.

Table 4.3: Summarised Heat Exchanger Results

	Effectiveness	Heat Transfer
NTU Calculations	34.97 %	76.99 kW
Heat Transfer Element Model	34.3 %	81.44 kW
Shell and Tube Model	35.4 %	79.35 kW

4.2.6 Solar Receiver

The solar receiver consists of a single 25m^2 heliostat that will track and reflect incoming solar radiation onto a volumetric receiver mounted above the hot gas test facility (HGTF) on the CSIR campus. The compressed air from the compressor passes through the volumetric receiver and in doing so is heated by the incoming solar radiation. The hot air then leaves the volumetric receiver and is used in the combustion process. Due to the air already being pre-

heated, only 70% of a conventional gas turbine's fuel requirements need to be added to attain the correct combustion temperature. This process, outlined above, describes the solar heat input for the pilot system, concerning the Rover 1S/60 gas turbine. Figure 4.17 (a) shows the $25m^2$ heliostat and Figure 4.17 (b) shows the focal spot developed by the mirror panels.

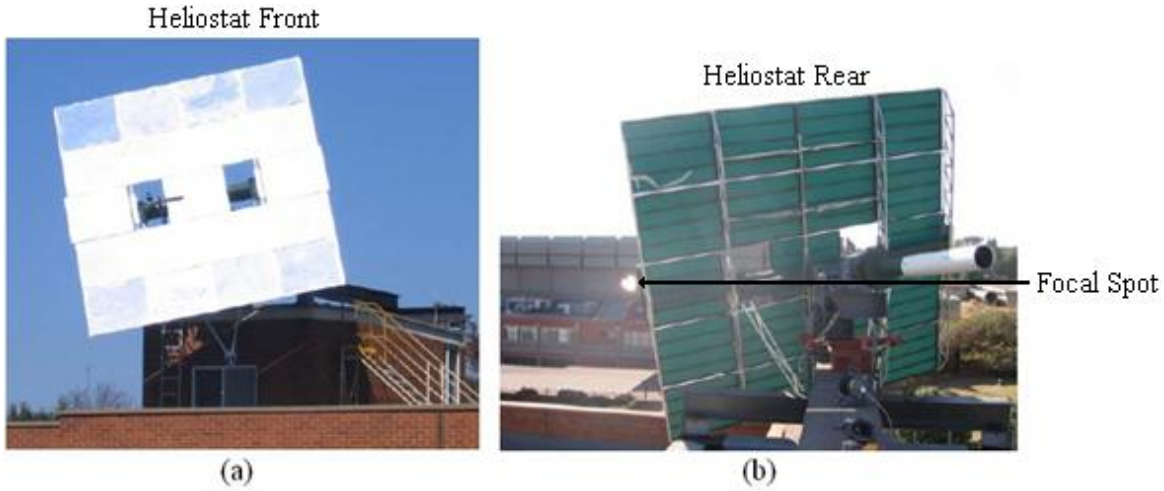

Figure 4.17: (a) Target Aligned Heliostat (front), (b) Heliostat with Focal Spot.

Currently the design of the volumetric receiver is the PhD topic of Roos (2008). The design is highly complex in its geometries and testing still remains to be be conducted on it. Thus for simplicity reasons the volumetric receiver was modelled using a pipe element so that basic geometries could be entered in order to best mimic the actual receiver as well as allow for a heat input value to be specified that would denote the solar heating. The simulation of the solar portion of the system was concerned with the actual heat input that occurs in the volumetric receiver. The heat input was measured by du Plessis (2010) by aiming the heliostat's focal spot onto a cone shaped cold water calorimeter mounted on the roof of the building where the focal spot is shown in Figure 4.17 (b) and then measuring the heat flux through a number of water filled tubes and hence throughout the focal spot. The maximum heat input was found to be 18 kW. This value was then simply specified as an input parameter for the solar model. Thus for the solar receiver a heat input in the form of kilowatts is merely specified on the pipe element responsible for simulating the volumetric receiver (see Figure 4.19) as a Q_{in} to the system. This Q_{in} can then be varied for different operating conditions/times of the system.

In order to vary the heat input to the volumetric receiver, in the case of cloud cover or malfunction, the “action” function in Flownex was used. This function allows the user to choose a target property on any component within the system, and vary this property based on the outputs of other properties or via a preset timing function that the user defines. Thus similar to the methodology used by Berenguel, et al. (2005) mentioned in Chapter 2, the heat input can be set to drop off gradually after a certain amount of time has elapsed to simulate daylight hours fading or conversely be set to increase gradually until a preset time to simulate morning hours. Figure 4.18 illustrates this concept. Total loss of heat input can also be simulated such as in the case of the solar system malfunctioning. Region 1 reflects the ramp up of energy during morning hours, followed by region 2 being the stable cloud-free region where the solar input fraction is at a maximum and finally region 3 denoting a decrease in incoming solar energy during late afternoon to evening hours.

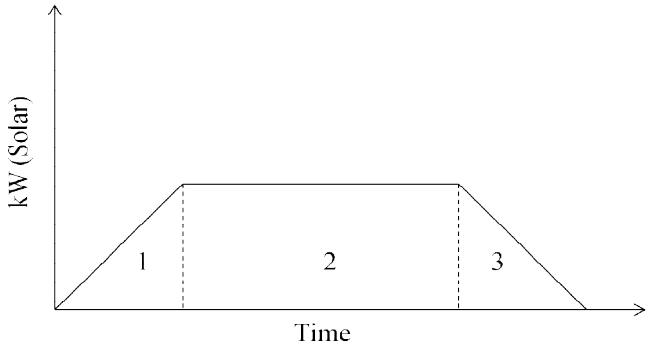

Figure 4.18: Incoming solar kilowatts vs. time (Typical Day Profile)

Additional components to supplement the volumetric receiver simulation are shown in Figure 4.19. These include valves that were added to assist in directing the air flow from the receiver to the thermal storage unit during the charging and discharging cycles. The valves allow for the isolation of a particular component during a specific mode of operation.

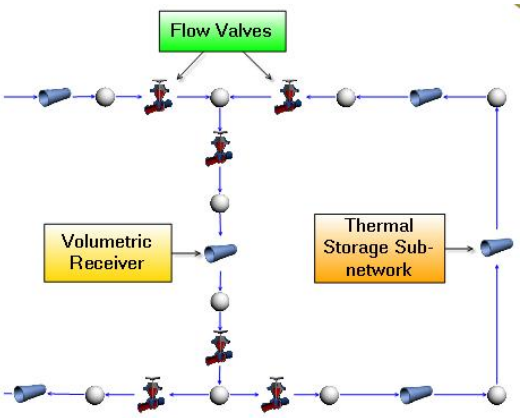

Figure 4.19: Solar Receiver with Supplementary Components

4.2.7 Thermal Storage

The thermal storage system was modelled as a sub-network and then incorporated into the volumetric receiver loop as seen in Figure 1.1 (Chapter 1) and Figure 4.19 above. The sub-network consists of a fan, solar receiver tower, thermal storage container and heat transfer element. Figure 4.20 shows the thermal storage circuit as well as an interactive progress bar which indicates when the storage is charged or running low.

It should be mentioned that the detailed analysis and modelling of the thermal storage component of the CSIR research project is currently ongoing and is the MSc (Eng) research topic of Klein (2010). Hence the purpose of this research report is not to develop a full thermal storage model but rather to create a model for simulation purposes in Flownex, only as a first attempt and basic approximation of how the thermal storage component should work within the system.

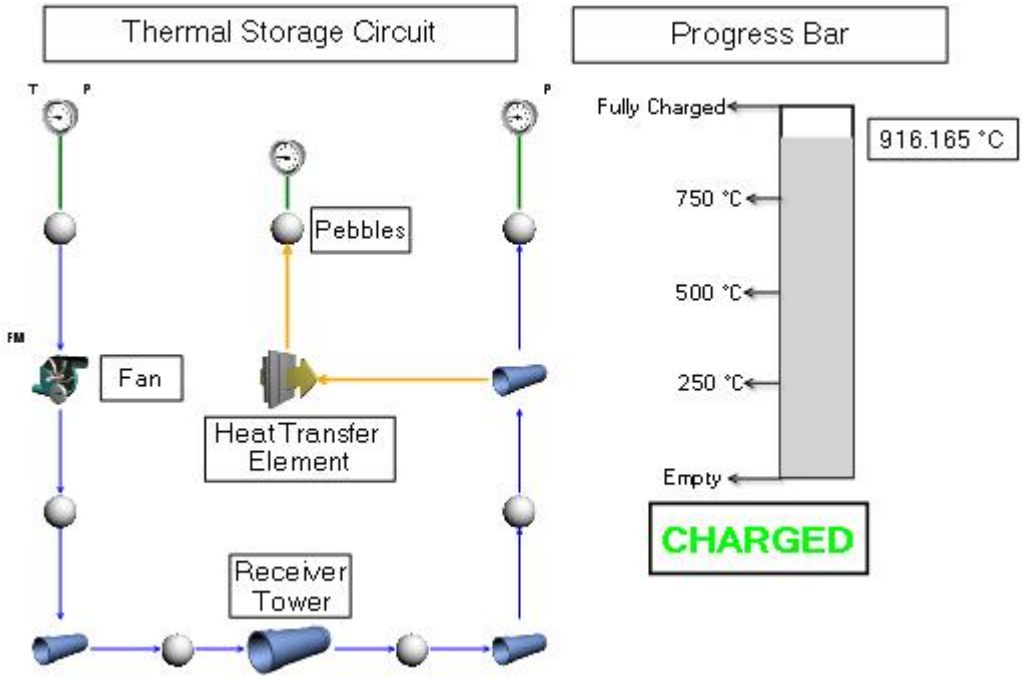

Figure 4.20: Depiction of Thermal Storage Circuit with Charging Bar Indicator

The sub-network is separate from the main network and thus requires a fan in order to create the required air flow within the system. This fan is shown in Figure 4.20 and merely provides the required air mass flow rate within the model. The air passes through the receiver tower

which is identical to the receiver tower in the main model but is only used to provide the solar heat input for the charging of the thermal storage in the sub-network. The heated air then flows through the thermal storage container and exits the system. The heat is stored in ceramic pebbles, packed in a random arrangement in a cylindrical vessel. The pebbles were taken to have an average diameter of 19 mm. The heat transfer that occurs from the heated air to the pebbles was calculated with the heat transfer element component. This component allows for the modelling of both conductive and convective heat transfer given the respective inputs. The pebbles are located downstream of the heat transfer element as seen in Figure 4.20. The heat transfer element is responsible for determining the rate at which heat is transferred from the fluid to the solid pebbles. The temperature of the downstream node from the heat transfer element (pebbles seen in Figure 4.20) rises until a specified maximum value is reached; it is this value which is depicted in the progress bar. This value is then fed back into the main network using an Excel component. During discharging heat transfer occurs in the reverse direction as cool air is passed through the pipe and the stored heat from the pebbles heats this cool air until the pebbles are completely discharged. A simplified resistor model of the heat transfer between the hot air and the pebbles can be described as shown in Figure 4.21. Here convection occurs until the hot air comes into contact with a pebble at which point conduction occurs to the centre of the pebble until thermal equilibrium is established between the hot air and the pebbles the process essentially repeats for each layer of pebbles.

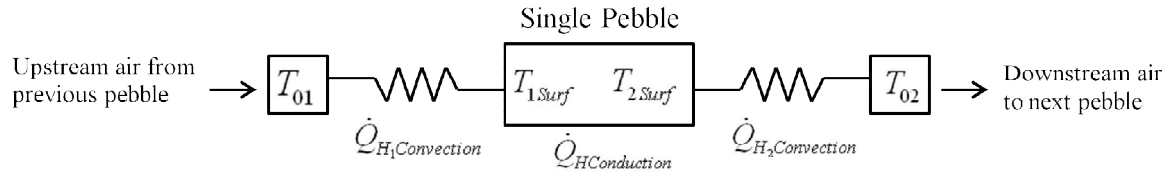

Figure 4.21: Heat Transfer Circuit Diagram for Hot Air and Pebbles

In reality the thermal storage container is stacked with multiple layers of pebbles in a random configuration as the pebbles are poured in vertically from the top of the container; Figure 4.22 (a) illustrates this. The Flownex heat transfer component allows for multiple conduction layers to be defined in case the user wishes to model heat conduction through a number of different materials in series. Similarly multiple convection layers can be defined in between the conduction layers. This was employed with the current model as all the pebbles are identical in shape and material properties, as well as there being air spaces between the pebbles inside the container. Thus a number of conduction and convection layers were

created within the heat transfer component. Each conduction layer was created having a thickness equal to the diameter of a pebble (±19mm). This is shown in Figure 4.22 (b).

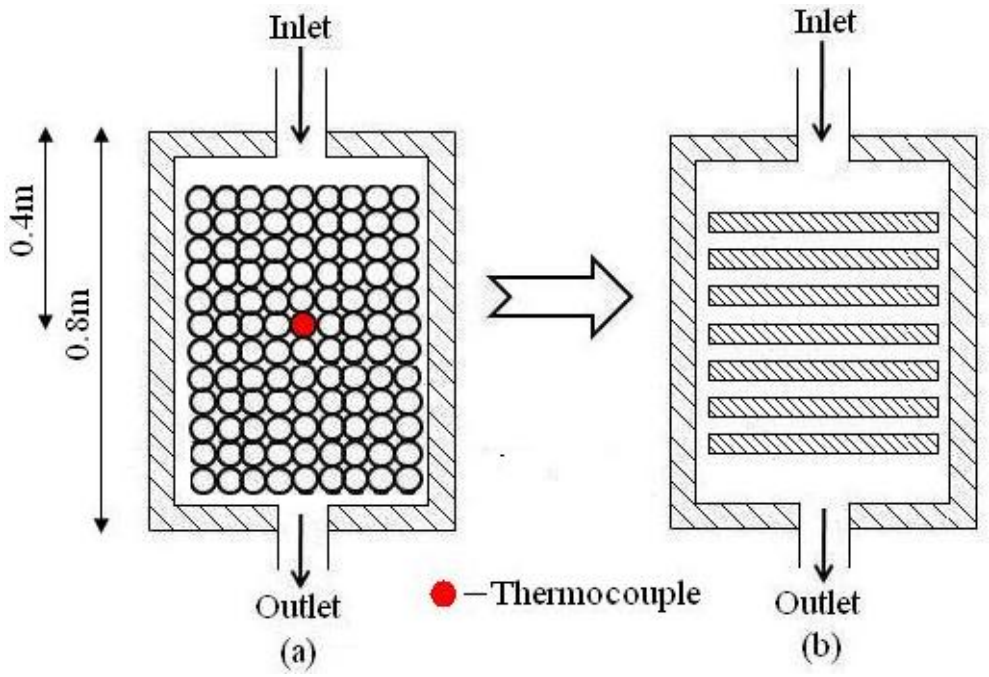

Figure 4.22: Thermal Storage Modelling Transformation

Similarly with each conductive heat transfer layer being defined in the model, convection effects, both upstream and downstream of each conduction layer were created. It was assumed that heat transfer to the surroundings was negligible as the thermal storage container was well insulated. The conduction heat transfer rate was assumed to be as well as thermal conductivity properties for a pebble. A simplified schematic of the heat transfer problem (charging scenario) is shown in Figure 4.23. Further properties for the pebble and the air not listed in the figure are defined in Appendix K.

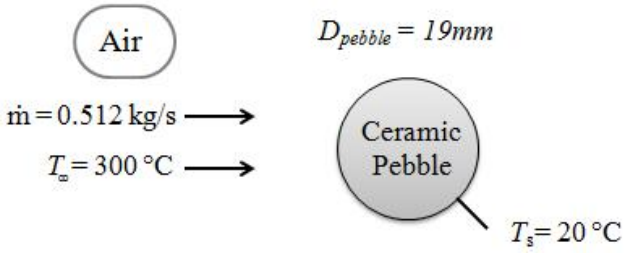

Figure 4.23: Heat Transfer Problem (Charging Scenario)

The inputs for the heat transfer component include the pebble surface areas, material thickness, material conductivity, conductive heat transfer coefficient and thermal capacitance as well as the convective heat transfer coefficient. For conduction the surface area was

specified as the total surface area of one layer of pebbles. The thickness of the conduction layer was specified to be 19 mm, equal to the diameter of an actual pebble. Standard values for the thermal conductivity and specific heat of the ceramic pebble material were used, these were 29 W/mK and 907 J/kgK respectively, (MatBase, 2011). The heat transfer coefficient was calculated in a similar manner to that of the heat exchanger in Appendix J. A Nusselt number correlation for packed beds was obtained from Wakao and Kaguei (1982) that would best represent the heat transfer for a random configuration of packed spherical pebbles and from this the heat transfer coefficient was found to be 15.73 W/m^2K for each layer of pebbles. The convective heat transfer coefficient was calculated using a Nusselt number correlation from Incopera and DeWitt (2002), this was found to be 165.49 W/m^2K, which fell within the acceptable range for forced convection heat transfer coefficients in air. (See calculations in Appendix K). Finally the maximum temperature which the pebbles can attain is directly related to the temperature of the air leaving the receiver tower. This is governed by the equation $Q = \dot{m}c_p(T_{out} - T_{in})$, where the heat input Q and mass flow rate $\dot{m}$ are known.

4.3 Final Simulation Networks

Specifications for three models are discussed in this section. The first model considers just the standard Rover engine without recuperation. The second model includes the modified heat exchanger and intake system and finally the third model integrates the solar receiver with thermal storage into the system. Each of the models was simulated for engine speeds of 22000, 26000, 30000, 34000, 38000, 42000 and the design point of 46000 revolutions per minute. For the solar system a case was attempted to look at cloud interference and the interaction between the combustor and solar receiver to ensure the turbine inlet temperature was maintained.

4.3.1 Standard Rover 1S/60 Model

The network consists of only those components comprising the standard gas turbine engine, namely the small intake ducts, compressor, combustor and turbine. For each of the models shown an interface diagram is also depicted of the system. The Flownex network for this model is shown in Figure 4.24. (Note: this is a screen shot taken of the system at a specific operating point) The screenshot of the interface follows in Figure 4.25.

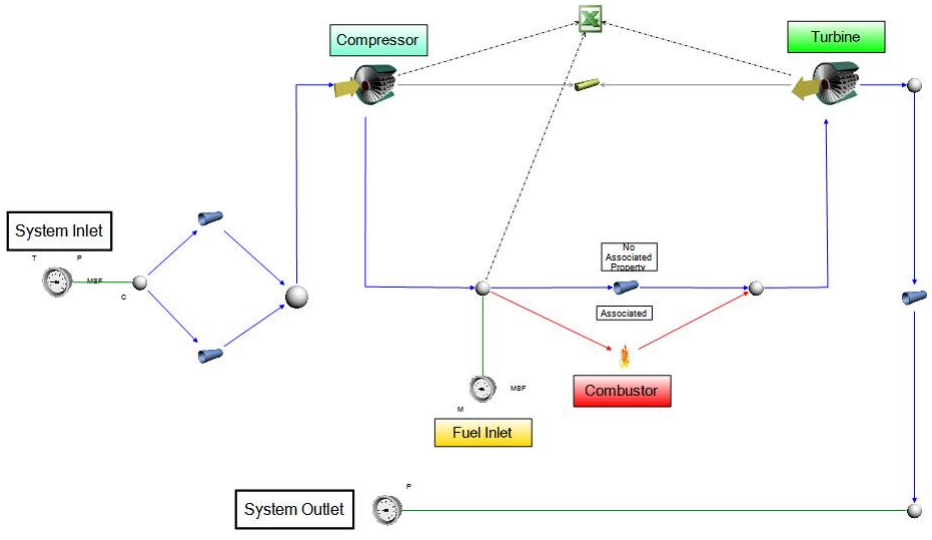

Figure 4.24: Flownex Model, Standard Rover 1S/60 Engine

These interfaces were created for each of the systems in order for the user to better understand the workings of the model and of the specific components within it. They allow the tracking of real-time changes in temperature, pressure and mass flow rate throughout the system as well as any other desired parameters.

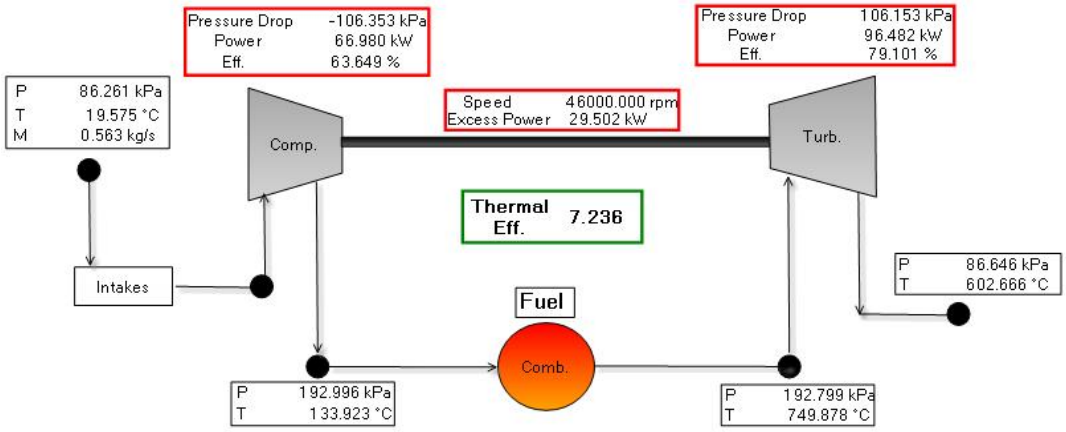

Figure 4.25: Interface Screen for Rover 1S/60 Model

4.3.2 Modified Rover 1S/60 Model

Figure 4.26 shows the model for the modified Rover engine. This includes the full intake system as shown in Section 4.2.2 as well as the modified shell and tube heat exchanger from Section 4.2.5.

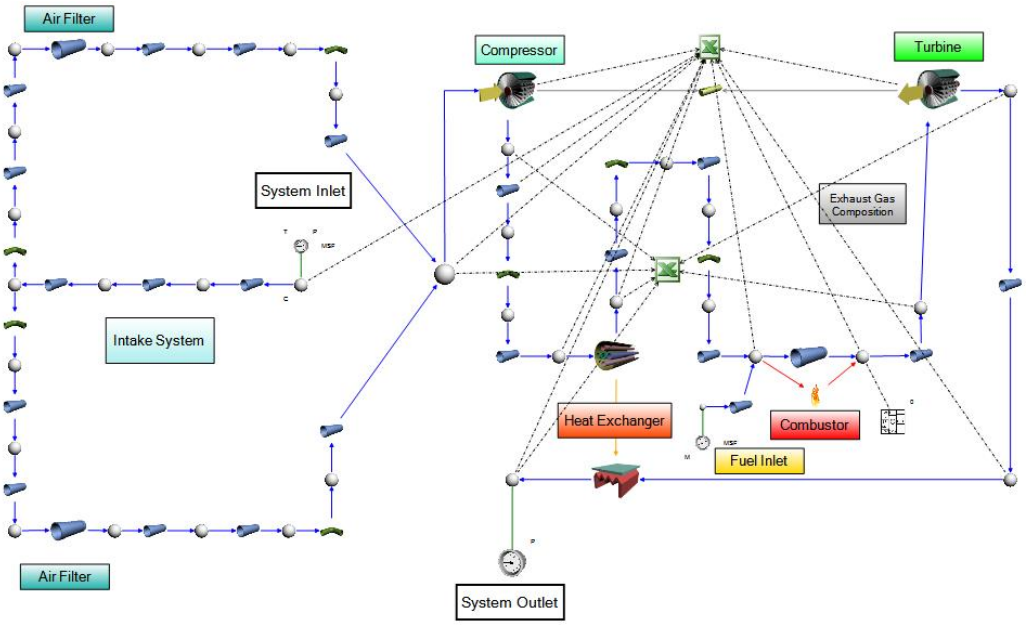

Figure 4.26: Flownex Model, Modified Rover 1S/60 Engine

The interface screen for this model differs slightly in that a tracking bar has been included which allows the user to interact with the system. The bar (bottom right of the figure) controls the fuel flow rate into the combustor. This gives the feel as if the actual gas turbine engine was running and the throttle was controlled manually.

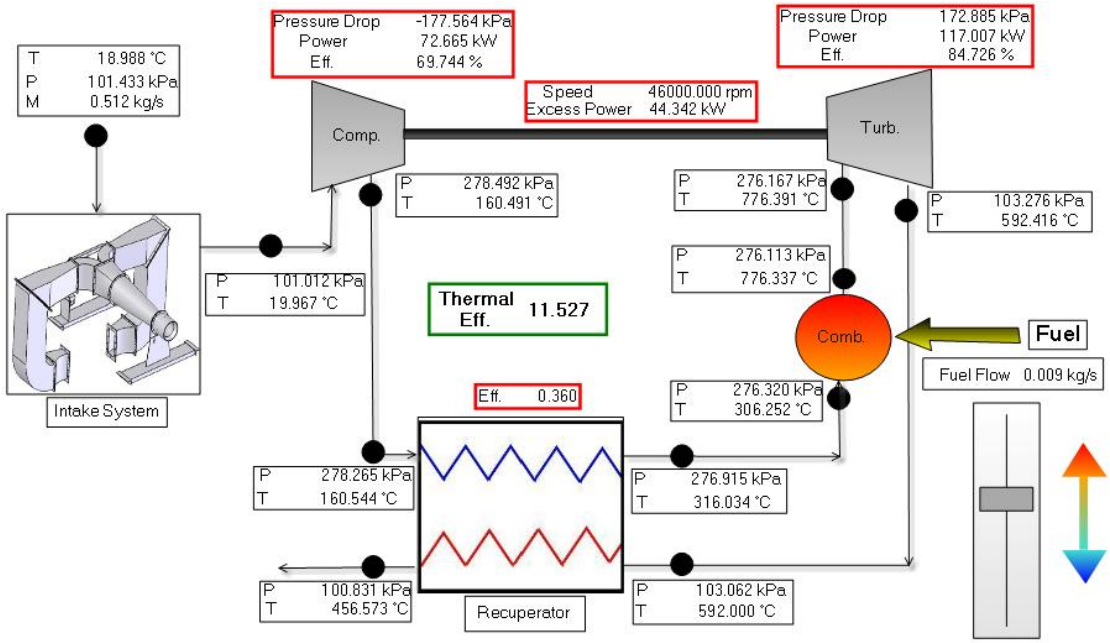

Figure 4.27: Interface Screen for Modified Rover 1S/60 Model

4.3.3 Solar Rover 1S/60 Model

This final model includes the solar receiver tower as well as the thermal storage component of the system, Figure 4.28. All valves are also included which direct the air flow through the necessary components during different operating modes. Each valve can be manually opened or closed in the interface screen. The final automated system is to have various modes available as seen in Figure 4.29. Day mode operation would allow for normal operation through the receiver tower during sunlight hours. During night mode the air cycles through the thermal storage tank and the system runs normally with the thermal storage discharging. Finally during charging mode operation air is circulated through the receiver tower and the thermal storage tank in an effort to “charge” the tank to high temperatures in order for it to be used during the night mode operation.

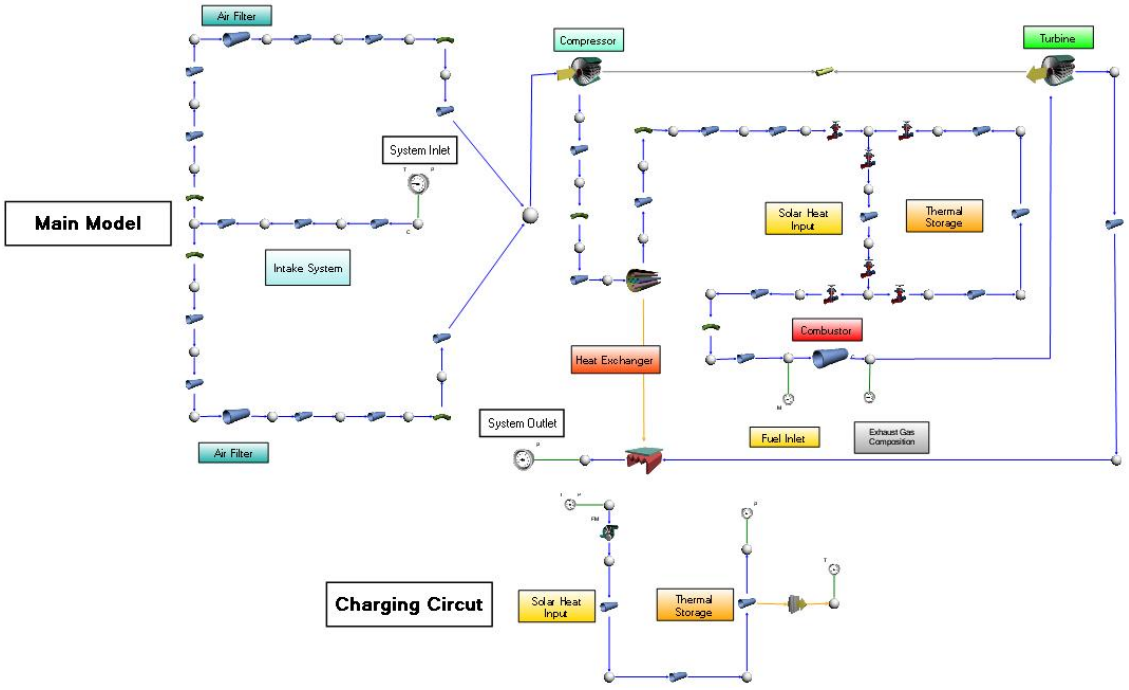

Figure 4.28: Flownex Model, Solar Rover 1S/60 Engine

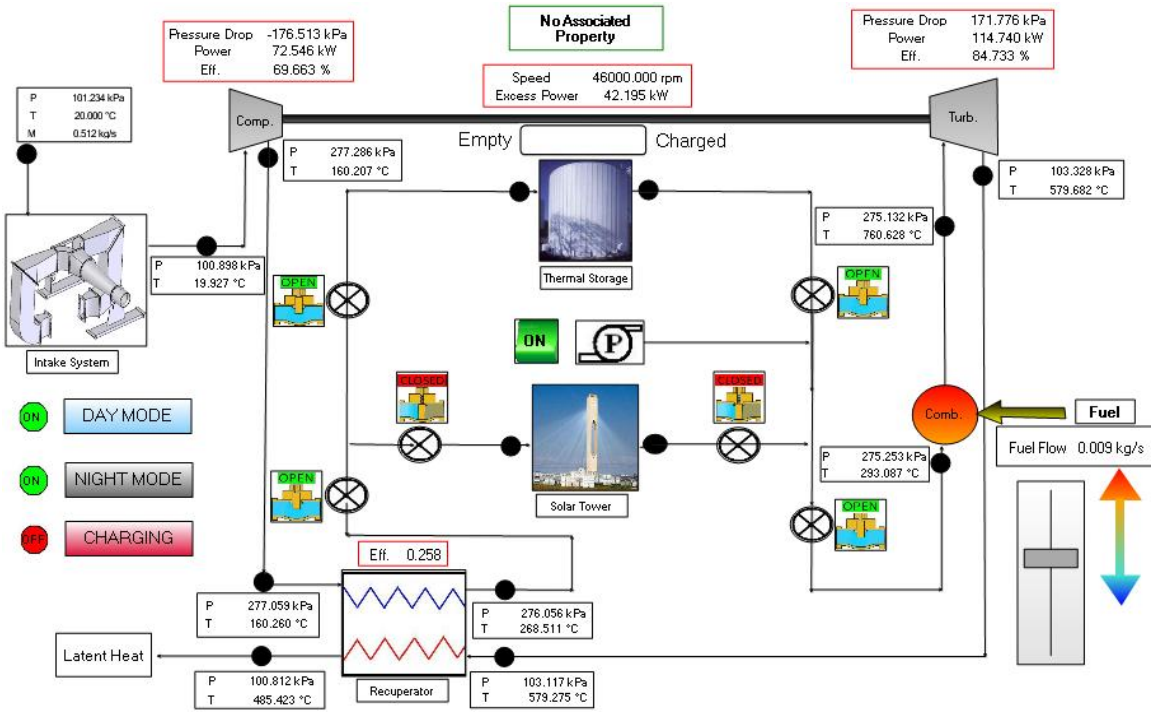

Figure 4.29: Interface Screen for Solar Model

For all models the only inlet conditions specified are the ambient inlet pressure and temperature as well as the system exit pressure back to ambient.

5 Results and Discussion

The numerical and experimental results from the Flownex simulations and Prinsloo (2008), respectively, are presented here. The experimental results of Prinsloo (2008) were used as a means of validating the simulation results attained from the Flownex software and as such the two sets of results are presented together wherever logical.

The three models investigated include the standard Rover 1S/60, the modified Rover 1S/60 and the Solar model. Each model is discussed separately with regard to its performance characteristics and overall comparisons are made between the three models where neccesary. The thermal storage performance is also discussed with regard to its integration into the solar model.

Steady state conditions were attained for all simulation models prior to the data collection for the results. With regard to the results from Prinsloo (2008), only single datum points were plotted on each of the respective comparison charts (Figure 5.4 to Figure 5.7), as Prinsloo only gathered data for specific engine speeds (discussed in Sections 3.2 and 3.4). Complete experimental results from Prinsloo (2008) can be seen in Appendix A.

The fuel flow rate was kept the same for the standard Rover 1S/60 and Modified Rover 1S/60 models in order to evaluate the change in performance characteristics such as thermal efficiency. However for the solar model the turbine inlet temperature was matched to that of the modified Rover and standard Rover models, for each respective engine speed, so that the change in fuel flow rate could be evaluated with the addtion of a solar heat input. Furthermore the solar model was evaluated based on a varying solar input (Figure 5.16 to Figure 5.19) to analyse the change in fuel mass flow rates and thermal efficiencies with a varying solar share.

Particular concerns with regard to Flownex's ability to model systems of this type as well the accuracy attained and specific issues encountered within the simulaitons are discussed at the end of the Chapter.

5.1 Simulation Results

5.1.1 Standard Rover 1S/60 Model

For the standard Rover 1S/60 model only basic parameters were considered such as the air mass flow rate through the system, Figure 5.1, and the thermal efficiency of the engine, Figure 5.2, to serve as a base line understanding of the engine's performance. The dashed line in each of the figures represents the engine's design speed of 46000 rev/min.

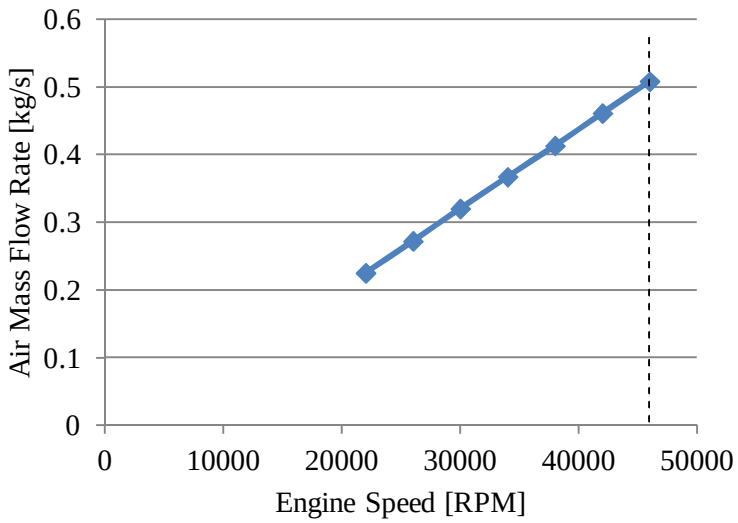

Figure 5.1: Air Mass Flow Rate vs. Engine Speed (Standard Rover)

The air mass flow rate increases linearly with an increase in engine speed. At the operating point of 46000 revolutions per minute the air mass flow rate is approximately 0.51 kg/s. This is slightly lower than the assumed air mass flow rate, from Section 4.2.1, of 0.518 kg/s for operation in Pretoria, however the difference is very small and the Flownex model correlates closely to the air mass flow rate for the standard Rover 1S/60.

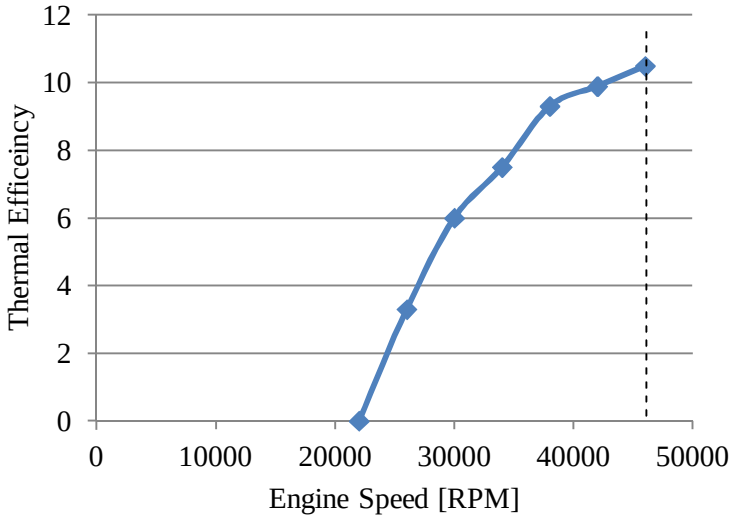

Figure 5.2: Thermal Efficiency vs. Engine Speed (Standard Rover)

The engine's thermal efficiency also increases with an increase in engine speed as expected, and then begins to plateau as the engine reaches its design operating point of 46000 revolutions per minute. From Figure 5.2, at this operating point the thermal efficiency is seen to be approximately 10.5 %. This correlates very closely with the empirical formulae used in Section 4.2.1, which yielded a thermal efficiency of 10.61 % for the Standard Rover 1S/60 engine. Further comparisons of the thermal efficiencies of all three main models can be seen later in this chapter in Figure 5.11.

5.1.2 Modified Rover 1S/60 Model

The modified Rover 1S/60 model encompasses the intake system discussed in Section 3.3.1, as well as the addition of the heat exchanger from Section 3.3.5. Figures 5.3 to 5.10 show results from the Flownex simulations of the modified Rover engine, along with datum points obtained from the experimental results of Prinsloo (2008) for specific operating speeds.

Figure 5.3 shows the air mass flow rate versus engine speed for the modified Rover engine. A slight difference is apparent at 40000 revolutions per minute where the Flownex air mass flow rate is lower than the testing result by approximately 0.06 kg/s. The figure also shows that the air mass flow rate of the modified Rover is slightly less than that of the standard Rover for the lower engine speeds, however closer to the design point both models are seen

to have similar air mass flow rates. This deviation of the modified Rover's air mass flow rate from that of the standard Rover can be explained by the addition of the recuperator and intake system which are present in the modified Rover's model. The addition of these two components increases the pressure drop through the system which would in turn decrease the air mass flow rate through the system. This is evident in Figure 5.3.

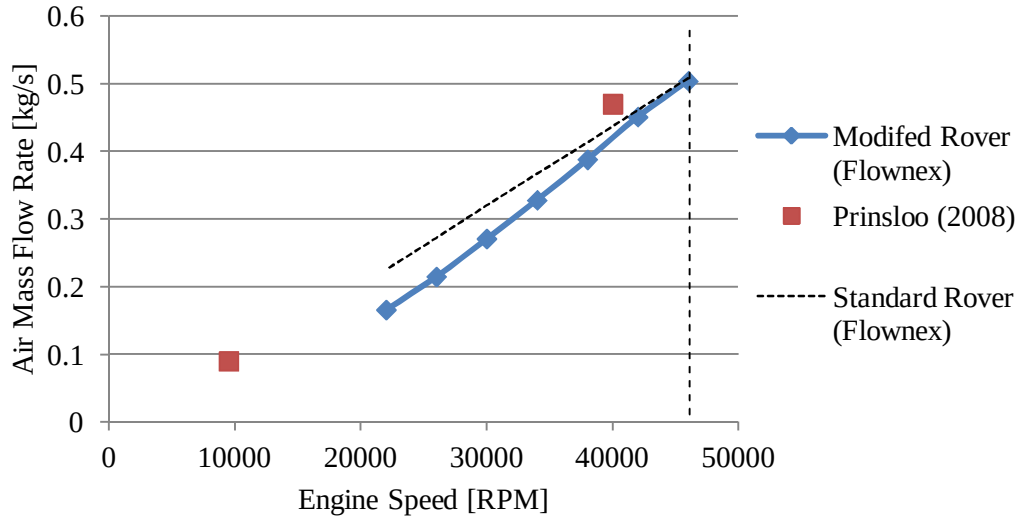

Figure 5.3: Air Mass Flow Rate vs. Engine Speed (Modified Rover)

Figure 5.4 depicts the pressure drop through the intake system. Again the Flownex pressure drop is lower than the testing results by approximately 300 Pa, this follows directly from the Flownex air mass flow rate being lower than the testing results as mentioned in Figure 5.3 above, hence at a lower flow rate the pressure drop will be less as is evident in Figure 5.4.

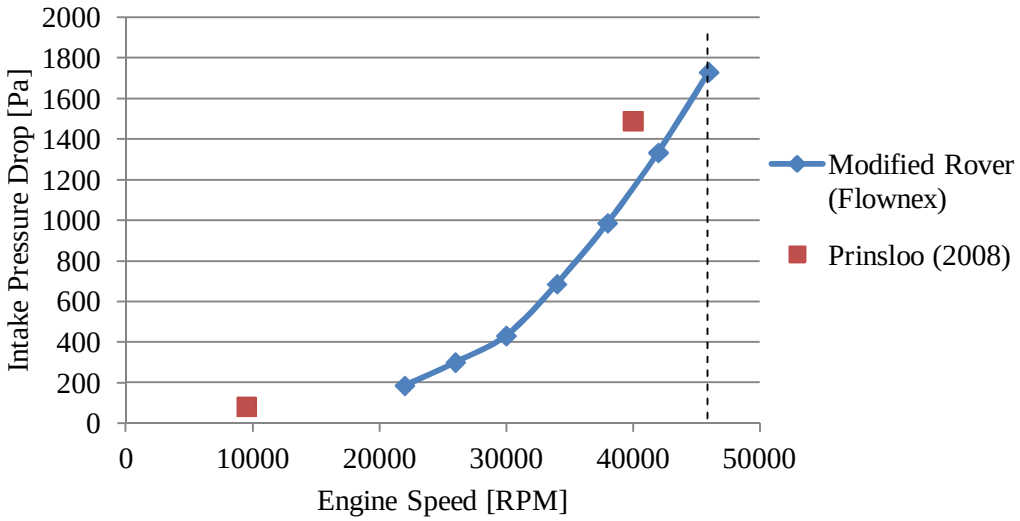

Figure 5.4: Intake Pressure Drop vs. Engine Speed (Modified Rover)

Figure 5.5 depicts the pressure drop through the cold side of the heat exchanger. Both the simulation results and the testing result of Prinsloo (2008) correlate very closely as is seen in the figure. However further data points could not be obtained from Prinsloo (2008) due to the engine problems mentioned in Section 3.4 restricting the data collection. Similarly Figure 5.6 illustrates the pressure drop through the hot side of the heat exchanger. There is a 200 Pa difference apparent at an engine speed of 40000 revolutions per minute. A linear relationship also exists between both parameters, hence the 200 Pa difference would hold for all engine speeds, however the difference is extremely small when compared to the overall pressure within the system at each respective speed. This difference may be corrected by increasing the loss coefficient in the simulation model on the hot side intake of the shell and tube heat exchanger component.

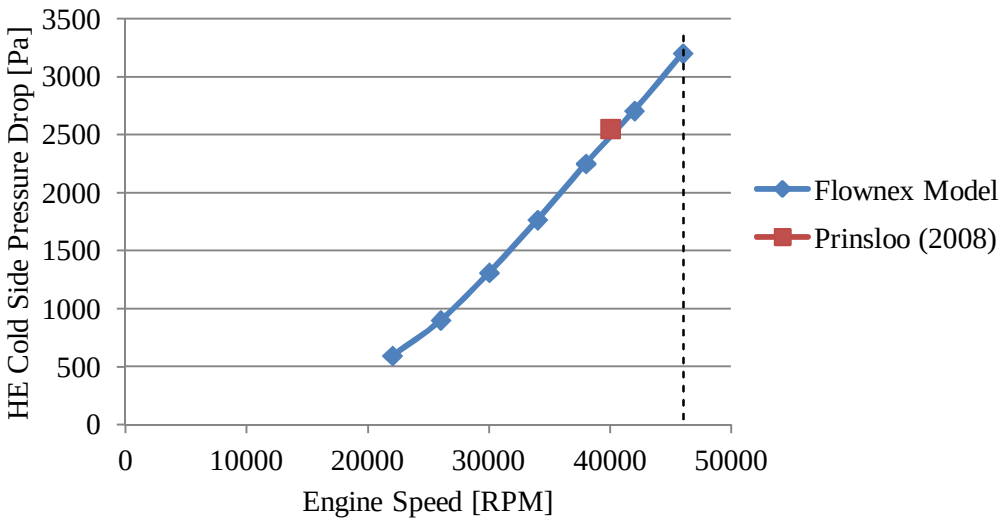

Figure 5.5: HE Cold Side Pressure Drop vs. Engine Speed (Modified Rover)

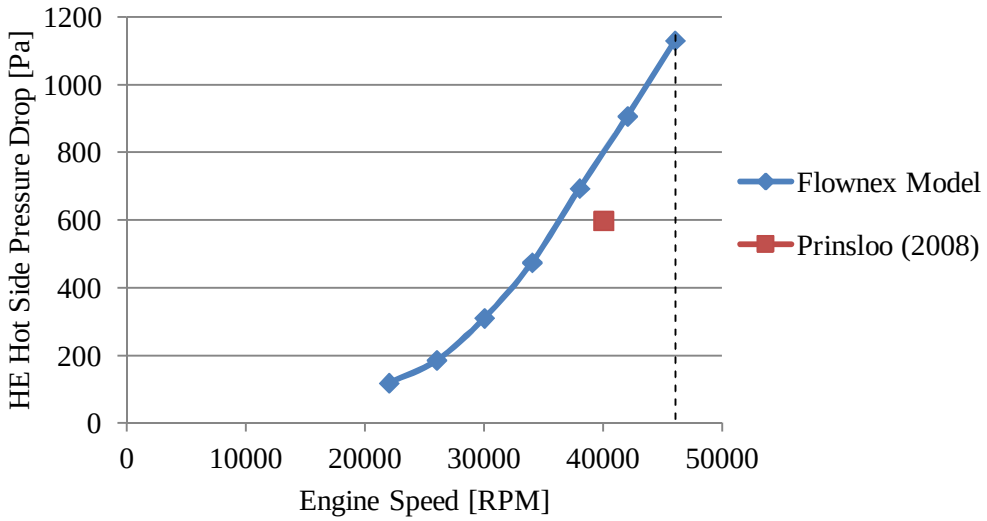

Figure 5.6: HE Hot Side Pressure Drop vs. Engine Speed (Modified Rover)

From Figure 5.7 the heat exchanger effectiveness remains fairly stable for a range of operating speeds between 30000 and 46000 revolutions per minute. The simulated effectiveness is seen to be 36 % at 40000 revolutions per minute, versus the experimental effectiveness of 35 % at the same engine speed.

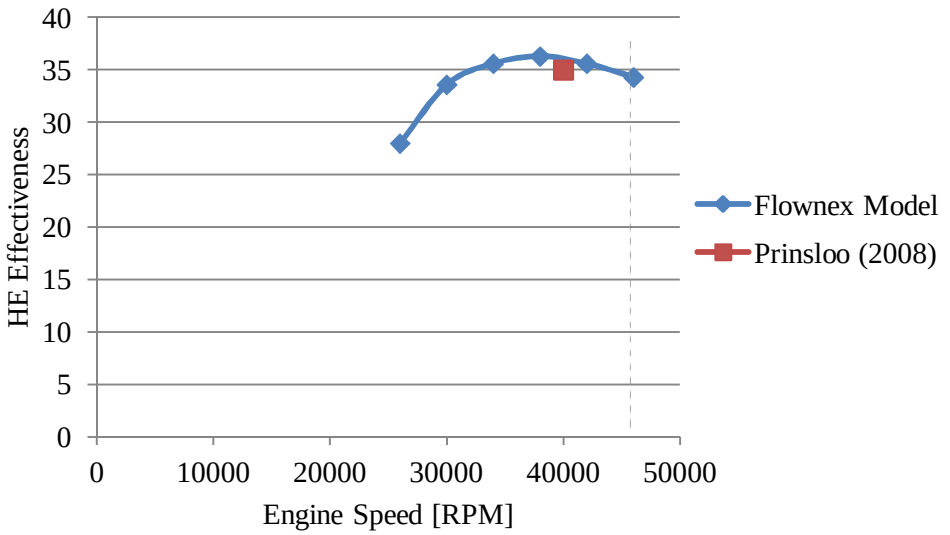

Figure 5.7: HE Effectiveness vs. Engine Speed (Modified Rover)

Figure 5.8 illustrates the system temperatures attained from the Flownex simulation while Figure 5.9 shows a reformatted graph of the same system temperatures from Prinsloo (2008). These figures were created purely as a visual comparison to check the temperature results of

the Flownex system against the temperature results of Prinsloo (2008). The figures represent a steady state scenario for a time of 10 seconds after which the engine cut out, Prinsloo (2008). Both sets of temperature readings correlate well for all points in the system with little or no differences apparent between the two sets of results. No experimental data were available for the heat exchanger's hot side outlet as the Rover engine was not instrumented at this point. However results from the Flownex simulation show the heat exchanger hot side outlet temperature to be in the range of 435 °C.

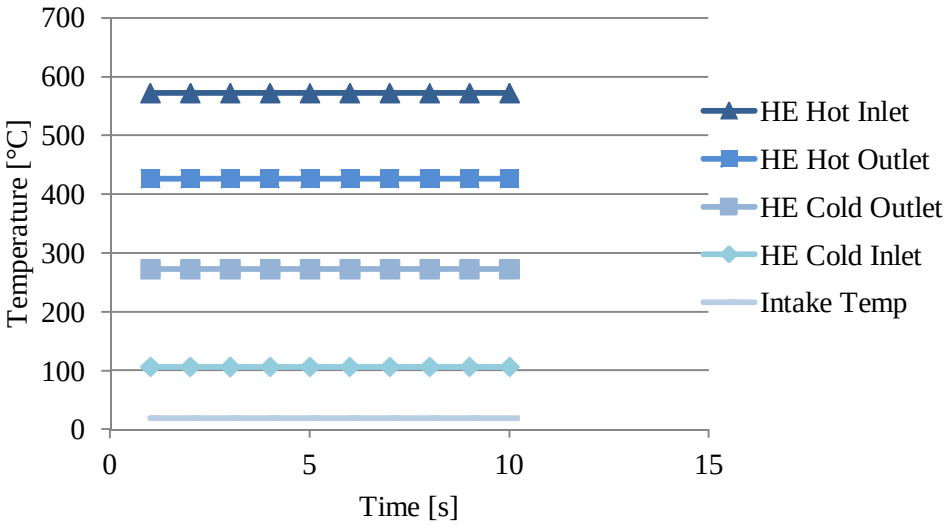

Figure 5.8: System Temperatures at 30000 RPM (Flownex)

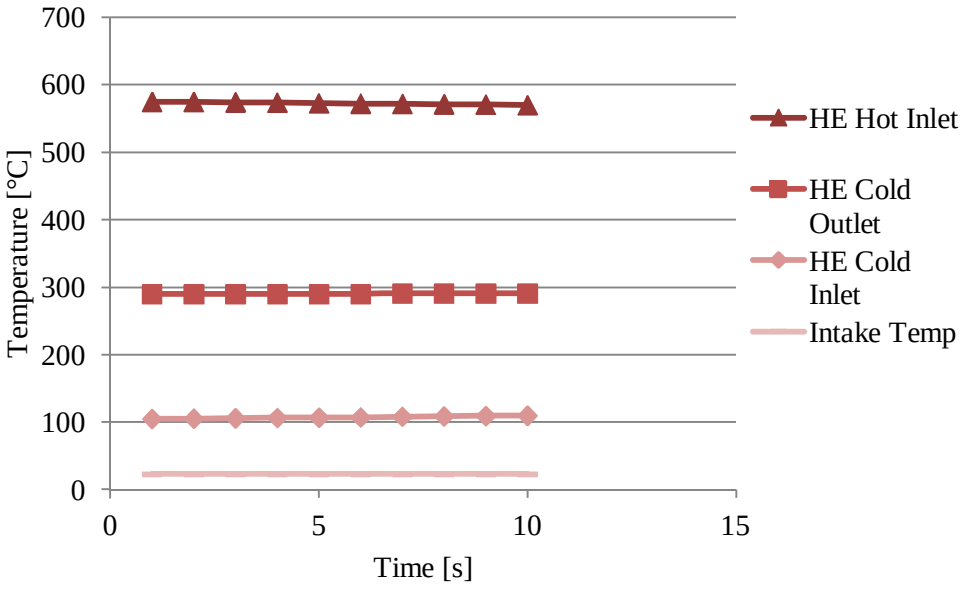

Figure 5.9: System Temperatures at 30000 RPM (Prinsloo, 2008)

Figure 5.10 illustrates the thermal efficiency of the modified Rover 1S/60 engine. The curve follows a similar trend to that of that standard Rover and a thermal efficiency of 12.76 % is attained at 46000 revolutions per minute. Again this is comparable to the numerical calculation for the first approximation of the thermal efficiency, done in Section 4.2.1, of 12.94 %.

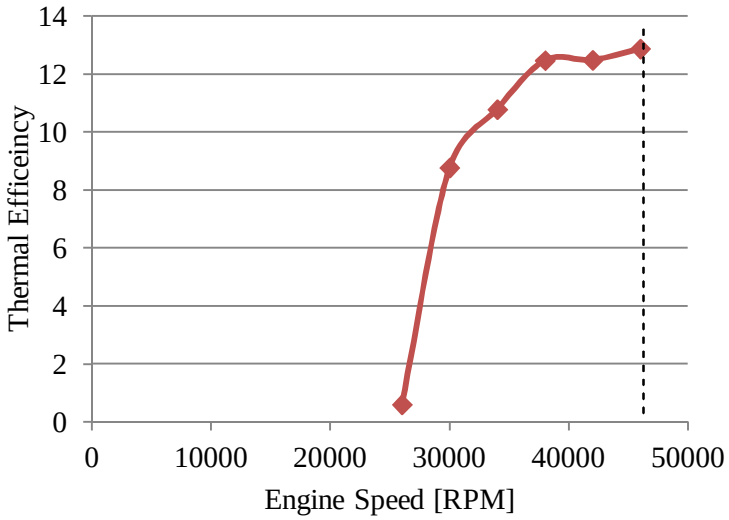

Figure 5.10: Thermal Efficiency vs. Engine Speed (Modified Rover)

5.1.3 Solar Rover 1S/60 Model – Constant Solar Heat Input

As stated at the beginning of this Chapter, the solar Rover 1S/60 model was first analysed with a constant solar heat input of 18 kW in order to simulate day time operation without any solar interference. 18kW is the nominal power that is provided by the heliostat discussed in Section 4.2.6.

Figure 5.11 shows the variation in thermal efficiency for each of the three systems analysed. The results show an increase in thermal efficiency with each respective system as expected. The standard model has the lowest thermal efficiency at the operating point as discussed earlier in Figure 5.2 with the modified Rover model showing a slight improvement on this due to the addition of the heat exchanger. Finally the solar model depicts the best thermal efficiency of 14.11 % at the design point. This is expected due to the additional solar heat input of 18 kW occurring before the combustor, hence reducing the amount of fuel required

in the combustor to reach the correct turbine inlet temperature and thus improving the overall thermal efficiency of the system.

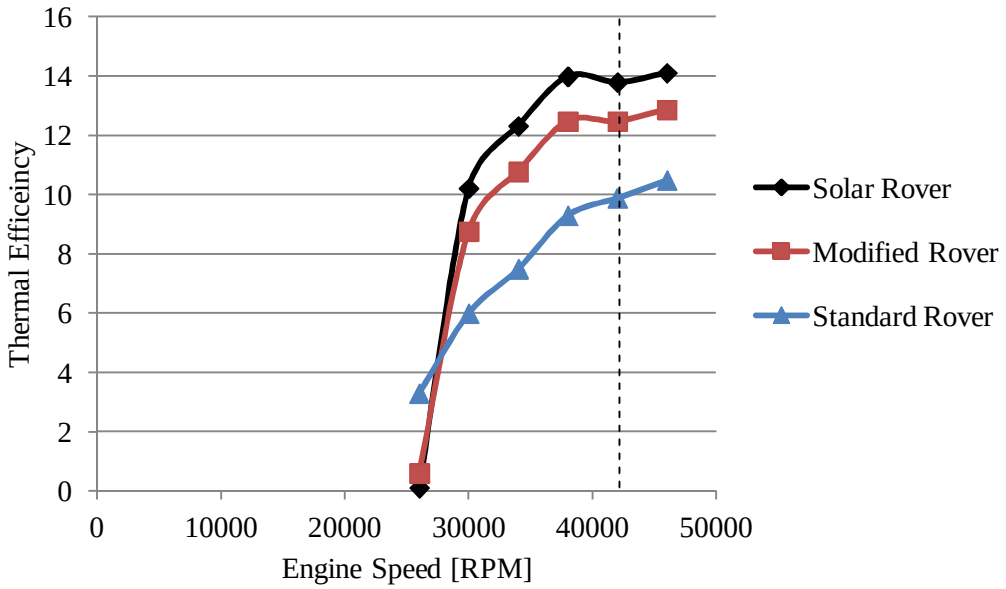

Figure 5.11: Thermal Efficiency vs. Engine Speed (Flownex)

Figure 5.12 shows the reduction in fuel mass flow rate between the solar model and the modified Rover model. As seen in the figure there is a definite reduction in fuel usage when operating the solar model.

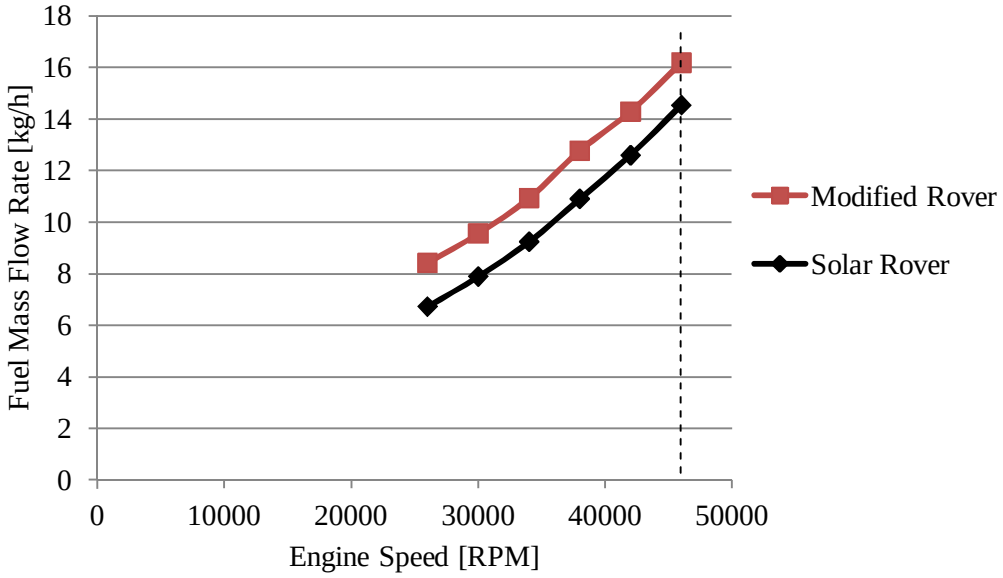

Figure 5.12: Fuel Mass Flow Rate vs. Engine Speed.

Furthermore Figure 5.13 quantifies this percentage difference in fuel usage between the modified and solar systems. Up to 20 % fuel savings are attained at lower operating speeds, reducing to around 10 % savings at the design point of 46000 revolutions per minute. This is directly linked to the efficiency with which the air is heated in the solar receiver as the air mass flow rate increases with an increase in engine speed. Figure 5.14 shows the temperature addition that the air receives when it passes through the solar receiver. As the graph shows, the most efficient or highest heating temperatures are attained at slower engine speeds, with the lowest solar heating occurring at the higher engine speeds. This is because there is a *constant* heat input of 18 kW into the solar receiver, thus as the air mass flow rate through the receiver increases, the temperature of the air exiting the receiver does *not* increase. However the solar receiver component is modelled only with basic geometries and thus losses in the receiver are small. The ideal solar receiver, currently the PhD topic of Roos (2008), should allow for the air to be circulated in a manner so that maximum heating time is attained while at the same time minimising the pressure loss through the receiver unit. This would increase the solar heating efficiency, thus further decreasing the fuel usage, hence increasing the overall thermal efficiency of the system.

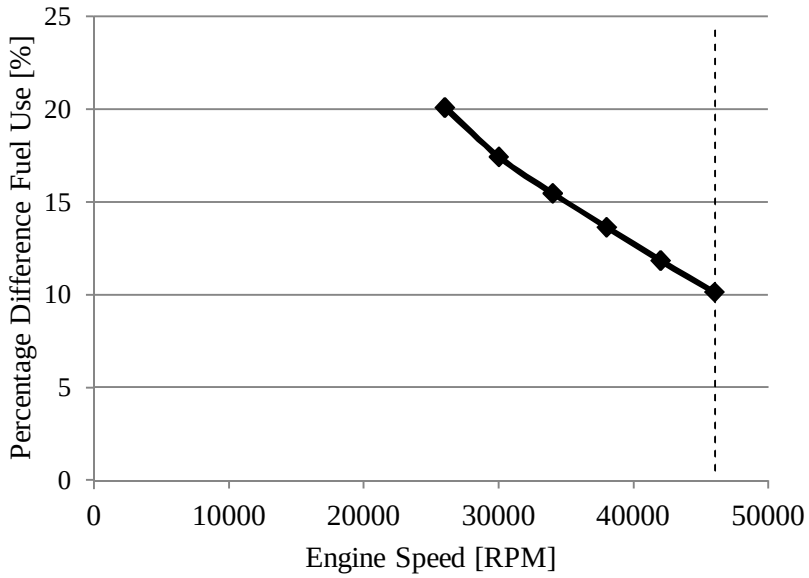

Figure 5.13: Percentage Difference in Fuel Usage vs. Engine Speed.

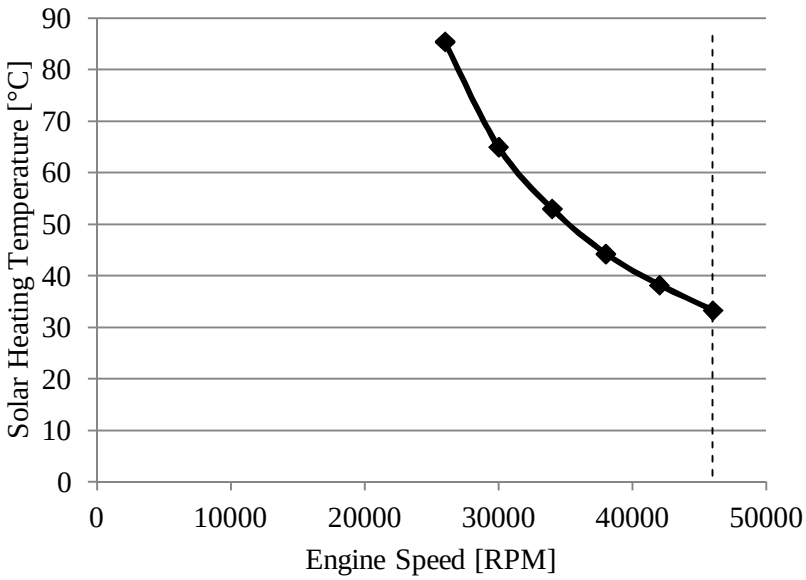

Figure 5.14: Solar Heating Temperature Rise vs. Engine Speed.

Finally the heat exchanger effectiveness for the solar model is shown in Figure 5.15. As expected there is no apparent difference in the heat exchanger's performance from the modified Rover model. This was used purely as a check to ensure the addition of the solar receiver did not change other results within the simulation model.

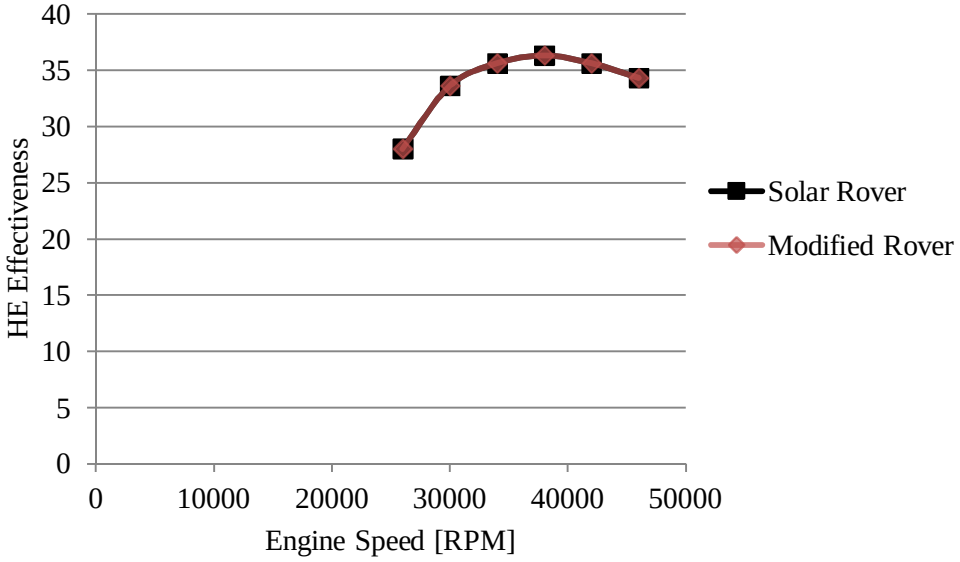

Figure 5.15: Heat Exchanger Effectiveness vs. Engine Speed.

5.1.4 Solar Rover 1S/60 Model – Varying Solar Heat Input

For this section the engine speed was kept constant at 46000 revolutions per minute while the incoming solar energy was varied. This was done in order to analyse the system behaviour during daytime operating conditions when the solar resource becomes intermittent. The solar energy was varied from 5 kW to 18 kW, and then further increased to a maximum of 100 kW in order to see how the system would behave in a larger heliostat field with a greater solar share.

Figure 5.16 shows the change in fuel mass flow rate in kg/h and the percentage saving in fuel as the solar energy share varies. As expected the greater the solar share the less fuel is used in the system which confirms that the model performs accurately if more heliostats were to be introduced into the system. Similarly for the percentage saving in fuel the graph is linear with more fuel being saved at higher solar energy inputs. For each increase in solar kW a 0.5 % fuel saving is realised.

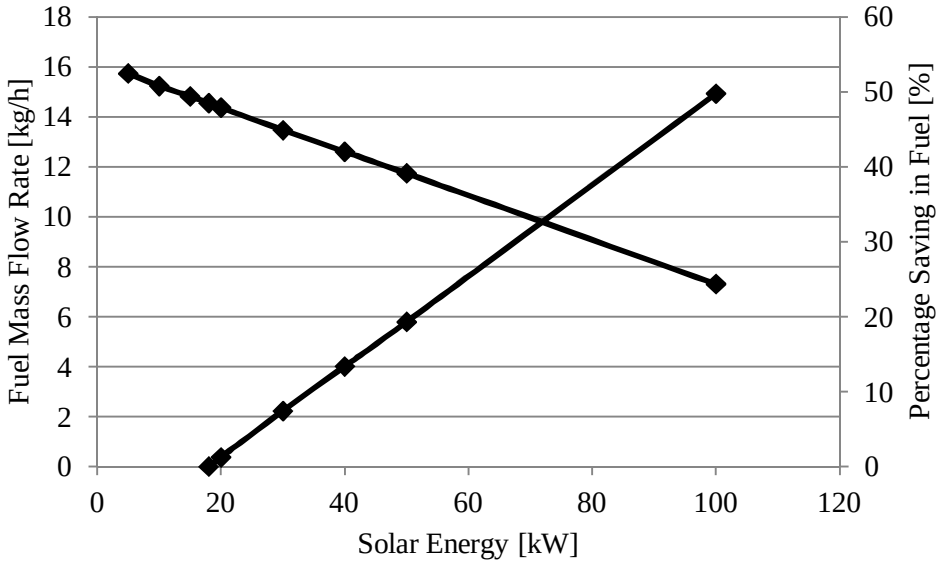

Figure 5.16: Fuel Mass Flow Rate vs. Solar Energy.

Figure 5.17 shows the rise in thermal efficiency with an increase in solar share. Each kW increase in solar power gives a 0.09 % increase in thermal efficiency. A final case was tested to find at what solar share the system would require no supplementary fuel input in order to

meet the turbine inlet temperature on solar heating alone. This was found to be at approximately 185 kW.

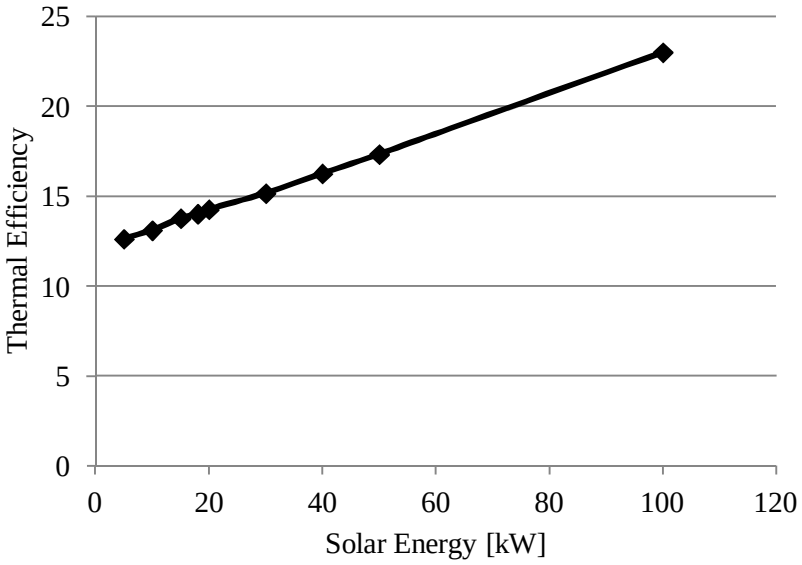

Figure 5.17: Thermal Efficiency vs. Solar Energy.

Figure 5.18 shows the increase in solar heating temperature with an increase in solar energy. The relationship is linear with the solar heating temperature increasing at approximately 2 °C for each increase in solar kW. It must be noted that the rate of heating is dependent on the geometry and configuration of the volumetric receiver, being designed by Roos (2011) at the time of this research report. This particular model serves as an example to demonstrate how the air would be heated in a generic receiver tower.

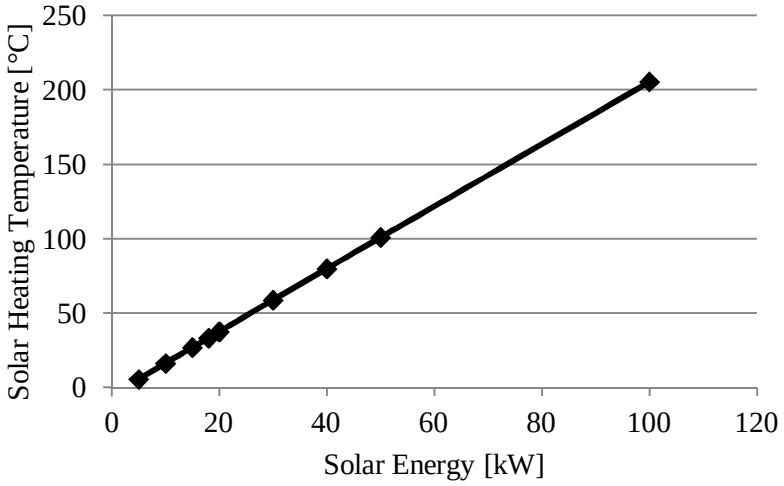

Figure 5.18: Solar Heating Temperature vs. Solar Energy

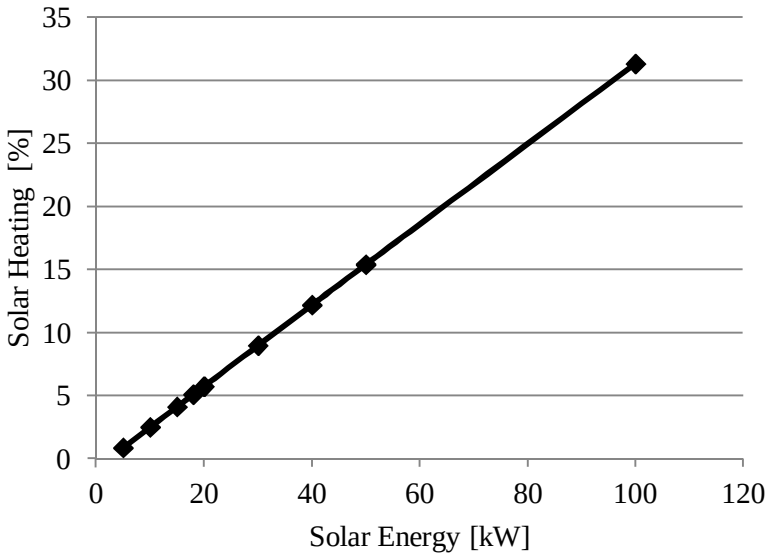

Figure 5.19: Solar Heating Percentage vs. Solar Energy.

Finally Figure 5.19 quantifies the solar heating temperature as a percentage of the maximum system temperature. For the current operating conditions with a solar energy input of 18 kW, only a 5 % solar heating percentage is realised for the system. However with a 100 kW solar energy input up to 30 % of the maximum system temperature is attained from solar heating alone. This then leads to increased thermal efficiency and fuel saving as discussed in the previous figures in this section.

5.1.5 Thermal Storage Model – Charging / Discharging

For the thermal storage analysis, comparisons were made to compare simulation results to experimental results from Klein (2011), seen in Appendix L. The two cases analysed included the charging (heating) and discharging (cooling) of the pebbles. Figure 5.20 and Figure 5.21 depict the two cases respectively. For both cases a further scenario was tested at 18 kW as this is the maximum solar energy that is generated by the heliostat mirror at the CSIR. For all simulations the air mass flow rates were set identical to those used by Klein (2011) for result comparison purposes. The data set used from Klein (2011) was for thermocouple measurements at the centre of the pebble bed and at the halfway point of the length of the test rig at 0.4m, see Figure 4.22. Performance characteristics of the thermal storage unit can be seen in Figure 5.22 and Figure 5.23 which describe the pebble

temperature and discharge time as a function of fuel usage respectively. In order to calibrate the Flownex model to attain the correct charging and discharging times the heat transfer coefficient (*h*) was varied iteratively until the model yielded adequate results.

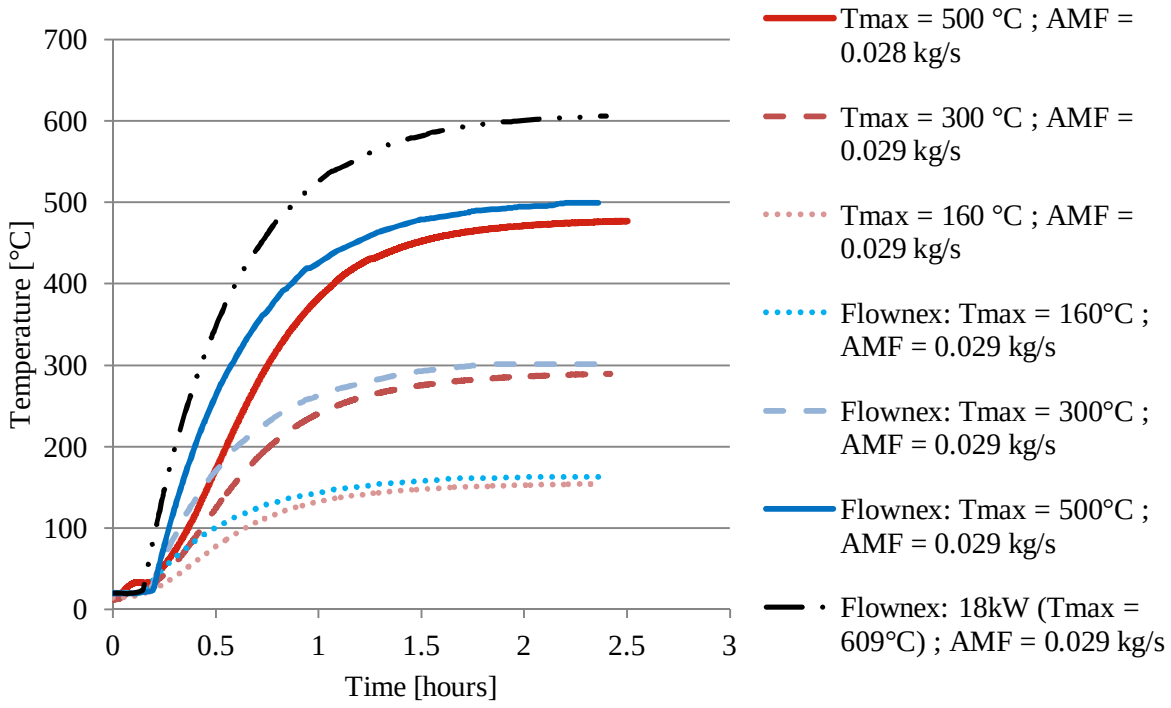

Figure 5.20: Thermal Storage Charging Results, Flownex vs. Experimental

In Figure 5.20 the simulation results are denoted by the blue curves while the experimental results of Klein (2011) are shown by the red ones. The black line represents an 18kW scenario which was run separately. For all three cases (160 °C, 300 °C and 500 °C) the Flownex results closely represent the experimental ones. For each of the temperature results a time difference on the x-axis is apparent between the testing results and the Flownex results. The Flownex results (blue curves) show an increase in temperature slightly before the testing results. This sudden increase in temperature which the Flownex curve (blue) shows is evidence of the discrepancy in the thermal storage resistance characteristic in the model, whereas the experimental results, more clearly visible in Appendix L, show a more gradual temperature rise, as is expected in reality. Initially the colder pebble would display a certain thermal resistance to the hot air followed by a gradual increase in temperature as the pebble starts to heat up. However after the initial temperature increase the curve closely follows the experimental findings for all three cases. Finally an 18 kW case was considered to find the maximum temperature that the pebbles would attain if the heliostat mirror were to deliver the

maximum energy input. Again the curve followed a similar pattern to the other three cases reaching a maximum temperature of 609 °C in a time of 2.1 hours. Figure 5.21 shows the discharging results.

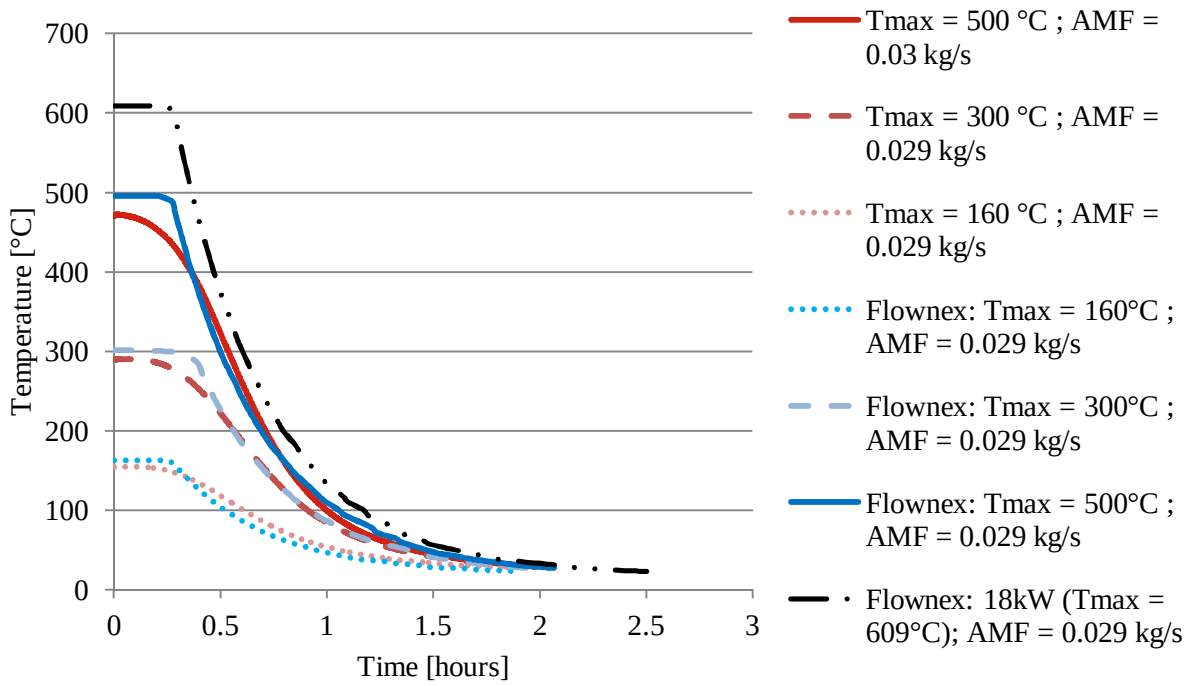

Figure 5.21: Thermal Storage Discharging Results, Flownex vs. Experimental

From Figure 5.21 a similar trend to that seen in Figure 5.20 is evident. Here the simulation results again correlate well with the experimental ones, with an even greater degree of accuracy. For all three cases a sudden drop is present, similar to the sudden rise seen in the charging results but in reverse form. However the time lag difference is not as prominent in Figure 5.21. The 18 kW case shows the discharge from the maximum temperature of 609 °C to ambient to occur within approximately 2.4 hours. This is a slightly longer discharge time than the other temperature cases, as expected, due to the higher initial “charged” temperature of 609 °C. Furthermore a noticeable point to be mentioned is that while the 18 kW case charges to a higher maximum temperature, the actual discharge time for the temperature to reduce back to ambient is very similar to that of the 500 °C case. Hence a maximum design temperature could be said to have been reached relative to the design of the current thermal storage unit. Thus in order to attain higher thermal storage temperatures and increase discharge times, design changes would be required to the thermal storage unit. This is the

current research topic of Klein (2011). Following this the discharging rate for the 18kW case was analysed with respect to the fuel flow rate in order to understand the non-daylight operation of the system. Figure 5.22 illustrates how the fuel mass flow rate of the system increases as the thermal storage unit discharges and the pebble temperature drops. As seen from the figure fuel is still required even at the higher temperatures as the turbine inlet temperature needs to be maintained. The fuel mass flow rate increases steadily as the pebble temperature drops until a critical temperature is reached. This critical temperature is the point where the pebble temperature is equal to the temperature of the air which exits the gas turbine's recuperator. At this point it is not feasible to further continue circulating the compressed air through the thermal storage circuit as it will have a cooling effect on the compressed air instead of a heating effect and hence lower the entire system's thermal efficiency. In this case, at the Rover's design operating point of 46000 revolutions per minute, the air exiting the recuperator is in the region of 260 °C, hence the critical temperature for the discharging to be discontinued is defined as 260 °C, after which point the system runs purely on fossil fuel.

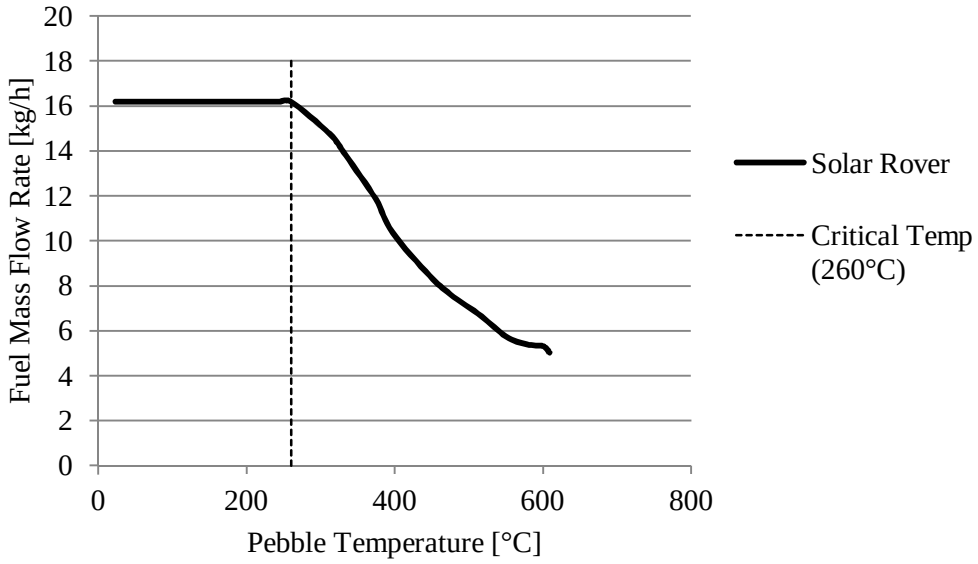

Figure 5.22: Pebble Temperature vs. Fuel Mass Flow Rate (Discharging)

Similarly Figure 5.23 depicts the change in fuel mass flow rate with discharge time. Again here a critical time is defined whereby it is no longer feasible to circulate the compressed air through the thermal storage unit. This time is seen to be at approximately 40 minutes and corresponds to the critical pebble temperature of 260 °C. Thus it could be said that the effective storage time which is gained from an initial pebble temperature of 609 °C is less

than 40 minutes as the discharging was only initiated at a time of 15 minutes. While this discharge time is very quick it must be noted that this is the effective time which it takes for the pebbles to drop in temperature from 609 °C to 260 °C. However the test rig created by Klein (2011) is only a first attempt at a design for high temperature thermal storage using air and further research is necessary in order to attain higher charging temperatures while at the same time increasing discharge times, but for the purposes of this study the thermal storage model created in Flownex has adequately simulated and replicated experimental results found by Klein (2011).

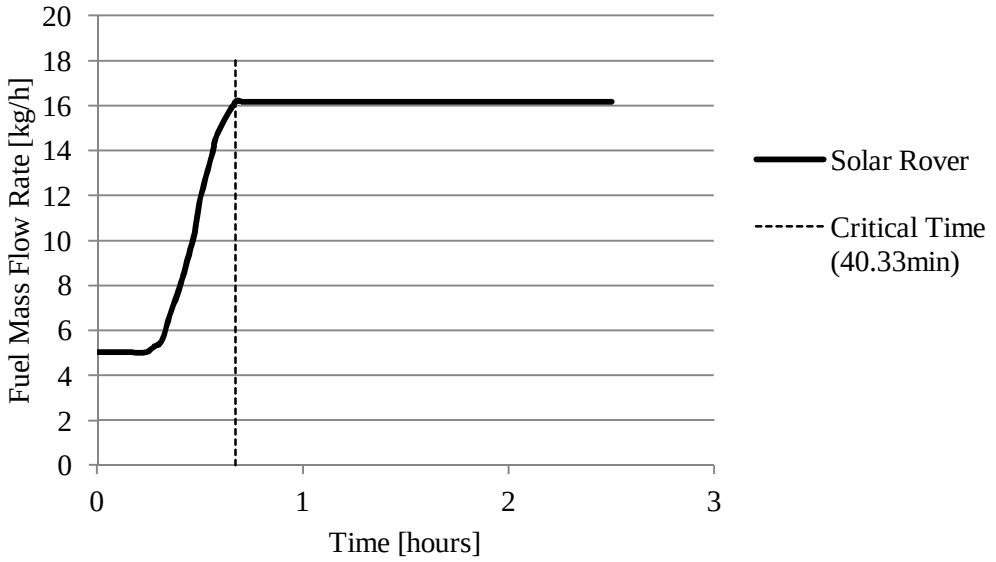

Figure 5.23: Time vs. Fuel Mass Flow Rate (Discharging)

5.2 Flownex Modelling Ability

The Flownex simulation package is a thermal – fluid network solver, as described in Section 4.1.1. From a gas turbine system simulation perspective the package is capable of modelling gas turbine systems with a reasonable degree of accuracy, however certain issues were encountered with regard to specific components and the parameters associated with these components. These concerns are discussed below.

Firstly looking at temperature results throughout the three different systems, Figure 5.8 and Figure 5.9, it was found that these correlated well with the experimental results with very little deviation. Temperature results from the heat exchanger simulations also correlated well with experimental findings as well as numerical calculations, Section 4.2.5, Table 4.3. Thus from a temperature perspective Flownex is accurate in its simulation ability provided that combustion conditions are properly modelled, refer to Section 4.2.3 which discusses the combustion modelling.

From a pressure perspective the pressures throughout the three models were found to correlate accurately with experimental results provided that exact geometries were specified and more importantly that loss coefficients were accurate for particular components. Figure 5.3 shows the air mass flow rate for the modified Rover simulation to be slightly less than the air mass flow rate of the standard Rover model. This is due to the addition of the heat exchanger in the modified Rover system which increases the flow resistance, resulting in a lower air mass flow rate for the modified system.

For the turbomachinery components it is essential that the inputs, in terms of compressor and turbine maps, are specified accurately and in a format which is compatible with the Flownex map editor. However once specified correctly, simulation of these components is accurate and yields good performance results.

When analysing the solar portion of the system which includes the solar receiver and thermal storage unit the following was found. The simulation of the solar receiver was simplified by only specifying an overall heat energy input in terms of solar kilowatts, however more detail could be specified by simulating the actual convection effect which occurs as the compressed air is heated by the sun. This would require full specifications of the volumetric receiver, which was still under design at the time of this research and furthermore possibly a solar tracking module should be incorporated into the Flownex program to allow modelling of these systems and increase accuracy. The thermal storage ability of the program was proven in Section 5.1 where simulation results correlated well with the experimental findings. While the thermal storage model created was only a basic first attempt at testing Flownex's thermal storage ability, it is felt that with further refinement and increased detail in modelling the convection effects between the pebbles a greater accuracy in the results may be obtained.

Overall the Flownex software is capable of simulating a gas turbine system with integrated thermal storage. From a solar perspective it is felt that the software requires further development in terms of adding an actual solar module option into the program which would allow users the creation of a detailed solar input with heliostat tracking options.

6 Conclusions and Recommendations

6.1 Conclusions

The simulation results conclude that it is possible to use the Flownex simulation package to develop a one-dimensional simulation model of a conventional gas turbine system modified for hybridised solar operation mode with integrated thermal storage and obtain adequate results.

From characterisation of the specific engine components, compressor (Appendix I) and turbine (Section 4.2.4) maps were generated using both empirical and computational techniques. Both methods yielded similar results with a final compressor efficiency of approximately 70 % and turbine efficiency of 85 %. Characterisation of the heat exchanger led to an effectiveness of 35 % being established. Pressure losses through the intake system as well as through both the hot and cold sides of the heat exchanger were quantified and are discussed in Chapter 5. The thermal storage model was validated against experimental data from Klein (2011). The simulation results closely represented the experimental findings. The total effective storage time was found to be approximately 40 minutes with the current thermal storage system built by Klein (2011). This links to the completion of the first and fourth objectives whereby all sub-components of the overall model were characterised and integrated into a computer simulation model that was developed using the Flownex software package.

In terms of the modelling ability of Flownex it was concluded from Section 5.2 that temperature results were found to be the most accurate performance measure, with pressures throughout the system also yielding accurate results provided loss coefficients were specified correctly. Flownex offers a combustion modelling function in the form of the adiabatic flame element, discussed in Section 4.2.3. This provided reasonable results for the temperature rise across the combustor. The comparison of the simulation model against the testing results of

Prinsloo (2008), along with the validation of the thermal storage model against the testing results of Klein (2011), mentioned earlier in this section, links to the completion of the second objective, to validate the model as far as possible.

Finally the models that were created are completely adaptable and reusable for CSP systems of this type. Geometries of specific piping components would need to be adjusted and compressor and turbine maps relative to the new system would need to be imported into the Flownex map editor, aside from these changes the gas turbine model remains unchanged, fulfilling the third objective with regard to the model being reusable as a standard model. Specific instructions with regard to the reusability of the model can be seen in Appendix M. The thermal storage model is also robust and adaptable in that if the system were to be scaled up only minor changes would be required to the model in order for it to be applicable for the larger system.

6.2 Recommendations

Given the constant release of newer versions of the Flownex package, further scope exists to increase the robustness of the model using the newer versions. Scope also exists to perform CFD modelling (possibly using the NUMECA CFD package) on the compressor geometry in order to obtain a detailed compressor chart for the Rover compressor as the methodology followed in this report serves only as a first attempt at generating performance maps for the Rover's compressor.

Furthermore for the intake model in Section 4.2.2 the General Empirical Relationship may be integrated into the model in order to obtain better accuracy for the pressure drop through the intake system at lower flow rates, although this is not paramount to the results it may again increase the robustness of the model.

Scope exists to modify and test the current simulation model against testing results from the larger 100 kW gas turbine unit at the CSIR. Thorough overhaul and re-commissioning of the Rover 1S/60 gas turbine may result in a better correlation between testing and simulation results.

With regard to the thermal storage model there is substantial scope for integrating the findings and numerical models of Klein (2011) into the Flownex thermal storage model in an attempt to further increase the accuracy of the results, and model larger thermal storage units that would support the 100 kW system.

The program allows the user to construct an interface environment which greatly simplifies the detailed network model into a manageable graphic interface to easily monitor performance parameters of the system. Finally from a solar perspective more advanced commercial software exists which allows for the sensitive modelling of the solar tracking aspect of a solar power plant while at the same time modelling the power cycle.

References

Bennet, I. (2011) *Hobby Gas Turbines*, [Online], Available: http://www.gasturbine.pwp.blueyonder.co.uk/newpage.htm.

Berenguel, M., Yebra, L., Dormido, S. and Romero, M. (2005) Modelling and Simulation of Central Receiver Solar Thermal Power Plants, 44th IEEE Conference on Descision and Control, Seville, Spain, 7410 - 7415.

Boer, M.M. (2011) *School of Mechanical, Industrial and Aeronautical Engineering, University of the Witwatersrand* , Johanessburg: Personal Communication.

Cohen, H., Rogers, G. and Saravanamuttoo, H. (2001) *Gas Turbine Theory, Fifth Edition*, 3rd edition, England: Pearson Education Limited.

Dixon, S.L. (1978) *Fluid Mechanics, Thermodynamics of Turbomachinery: 3rd Edition*, Pergamon Press.

Du Plessis, D. (2010) *Final year project: Cold Water Calorimeter Instrumentation and Testing*, School of Mechanical Engineering, University of Pretoria, Pretoria.

ESTEQ (2009) *ESTEQ Engineering*, [Online], Available: http://engineering.esteq.co.za/flownex/flownex [May 2010].

Fisher, U., Sugarmen, C., Ring, A. and Sinai, J. (2004) Gas Turbine "Solarization" - Modifications for Solar/Fuel Hybrid Operation, *ASME*, vol. 126, August, pp. 872-878.

Flownex (2010) *Flownex Simulation Environment*, [Online], Available: http://www.flownex.com/productoverview [May 2010].

Flownex (2010) Flownex Theory Help File.

Fraunhofer, I. (2009) TREE - "Transfer Renewable Energy & Efficiency", Seminar on Concentrating Solar Power (CSP), Johannesburg.

GetData (2011) *GetData Graph Digitizer*, Available: http://www.getdata-graph-digitizer.com/ [28 March 2011].

Heller, P., Pfander, M., Denk, T., Tellez, F., Valverde, A., Fernandez, J. and Ring, A. (2006) Test and Evaluation of a Solar Powered Gas Turbine System, *Solar Energy*, pp. 1225 - 1230.

IET (2010) *Institute for Energy Systems and Thermodynamics, Austria*, [Online], Available: http://www.iet.tuwien.ac.at/department_of_fluid_flow_machinery/laboratory/thermal_laboratory/EN/ [12 May 2010].

Incropera, F.P. and DeWitt, D.P. (2002) *Introduction to Heat Transfer*, 4th edition, John Wiley & Sons.

ISES (2009) *ISES: Solar World Congress 2009*, November, [Online], Available: http://25degrees.net/index.php?option=com_zine&view=article&id=832:ises-solar-world-congress-2009&Itemid=81 [May 2010].

Judge, A.W. (1960) *Small Gas Turbines and Free Piston Engines*, London: Chapman & Hall Ltd.

Kays, W.M. and London, A.L. (1984) *Compact Heat Exchangers*, 3rd edition, USA: Donnelly & Sons Company.

Klein (2011) *MSc(Eng) Dissertation (draft): High Temperature Thermal Storage*, School of Mechanical, Industrial and Aeronautical Engineering, University of the Witwatersrand, Johanessburg.

Landman, W.A. and Greyvenstein, G.P. (2004) Dynamic Systems CFD Simulation Code for the Modelling of HTGR Power Plants, 2nd International Topical Meeting on High Temperature Reactor Technology, Beijing, 1-16.

MatBase (2011) *Material Properties Database*, [Online], Available: http://www.matbase.com/material/ceramics/alumina/al2o3-90/properties [25 April 2011].

MIT (2010) *MIT Gas Turbine Laboratory*, [Online], Available: http://web.mit.edu/aeroastro/labs/gtl/early_GT_history.html#1939 [May 2010].

M-Tech Industrial (2008), [Online], Available: http://www.mtechindustrial.com/ [June 2010].

NREC (1972) *The Design and Performance Analysis of Axial Flow Turbines: Volume 1 - Theory and Practice of Design*, Cambridge, Massachusetts: Northern Research and Engineering Corporation.

Phakathi, S. (2009) *Final year project: Commissioning of a Rover 1S/60 Gas Turbine*, School of Mechanical Engineering, University of Pretoria, Pretoria.

Prinsloo, L. (2008) *Final year project: The Commissioning of the Rover 1S/60 Gas Turbine*, School of Mechanical Engineering, University of Pretoria, Pretoria.

RLQDesign (2009) *RLQ Design CC*, Pretoria: Weirda Park (012) 654-1416.

Romero, M., Marcos, M., Tellez, F., Blanco, M., Fernandez, V., Baonza, F. and Berger, S. (1999) Distributed Power from Solar Tower Systems: A MIUS Approach, *Solar Energy* , vol. 67, no. 4-6, pp. 249-264.

Roos, T.H. (2006) *Progress on the Heliostat and Renewable Energy Project for 2007/08*, Pretoria: CSIR, DPSS.

Roos, T.H. (2008) *Low-Cost High Temperature Volumetric Receiver for Solar Gas Turbine*, Pretoria: CSIR, DPSS.

Rover (1966) *Rover Gas Turbines: Engine Type IS/60 and IS/90 Maintenance Manual*, Coventry.

Schwarzbozl, P., Buck, R., Sugarmen, C., Ring, A., Crespo, M., Altwegg, P. and Enrile, J. (2006) Solar Gas Turbine Systems: Design, Cost and Perspectives, *Solar Energy*, vol. 80, pp. 1231 - 1240.

Siemens (2010) *Siemens power generation*, [Online], Available: http://images.google.co.za/imgres?imgurl=http://www.powergeneration.siemens.com/NR/rdonlyres/5A084C56-2B56-4D82-B85F-86466BB06930/0/Gas_Turbine15_002266_72dpi.jpg&imgrefurl=http://autoracing.virgula.uol.com.br/forum/index.php%3Fshowtopic%3D48900%26mode%3D [March 2010].

Solar Thermal Energy (2010), [Online], Available: http://www.solar-thermal.com/solar-thermal.pdf [17 April 2010].

SOLGATE (2002) *SOLGATE: Solar Hybrid Gas Turbine Electric Power System*, European Commission.

Stine, W.B. and Geyer, M. (2001) *Power From the Sun*, [Online], Available: http://www.powerfromthesun.net [March 2010].

TRNSYS (2011) *TESS - Thermal Energy Systems Specialists*, [Online], Available: http://www.trnsys.com/ [29 Jan 2011].

Wakao, N. and Kaguei, S. (1982) *Heat and Mass Transfer in Packed Beds*, Yokohama, Japan: Gordon and Breach Science Publishers.

Walsh, P.P. and Fletcher, P. (1998) *Gas Turbine Performance*, Oxford, England: Blackwell Science Ltd.

Appendix A – Rover 1S/60 Testing Results, Prinsloo (2008)

The following pages depict results attained by Prinsloo (2008) for the running of the Rover 1S/60 engine. Measurements were taken for various speeds of the engine, ranging from 9500 – 40000 rev/min. Results shown here were only documented up to 10 seconds.

Mass Flow Rates and Pressure Drops:

Figure A.1 and Figure A.2 illustrate the Air mass flow rate through the system while Figure A.3 and Figure A.4 show the pressure drop across the intake.

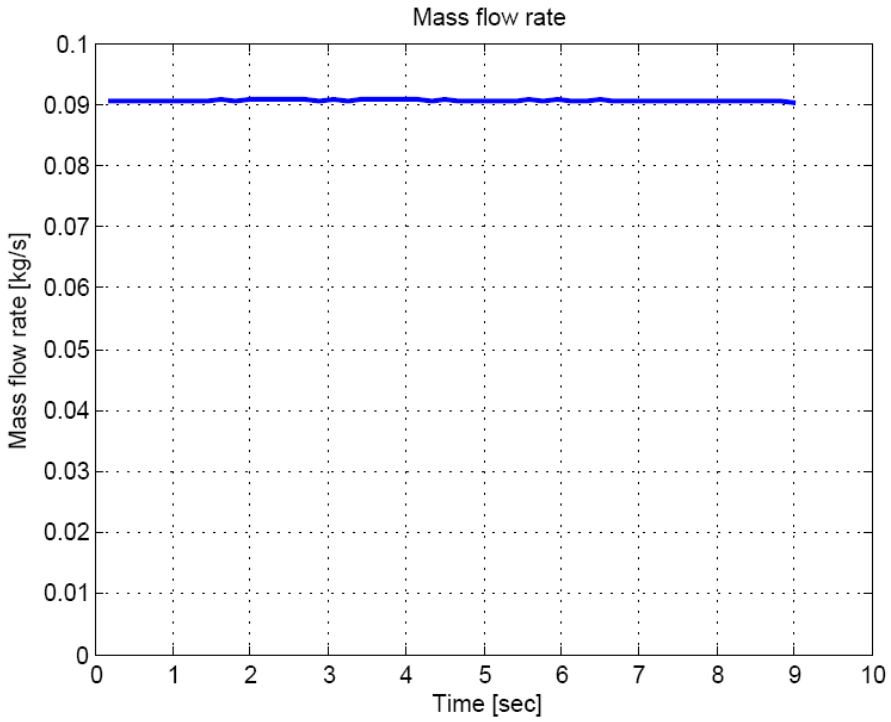

Figure A.1: Air Mass Flow Rate vs. Time at 9500 rev/min

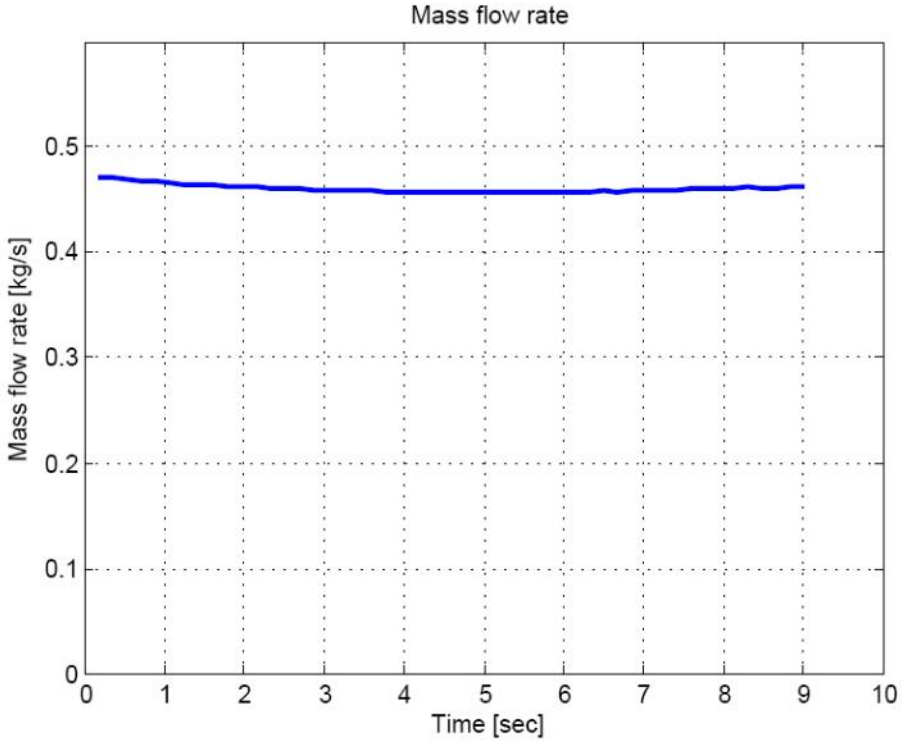

Figure A.2: Air Mass Flow Rate vs. Time at 40000 rev/min

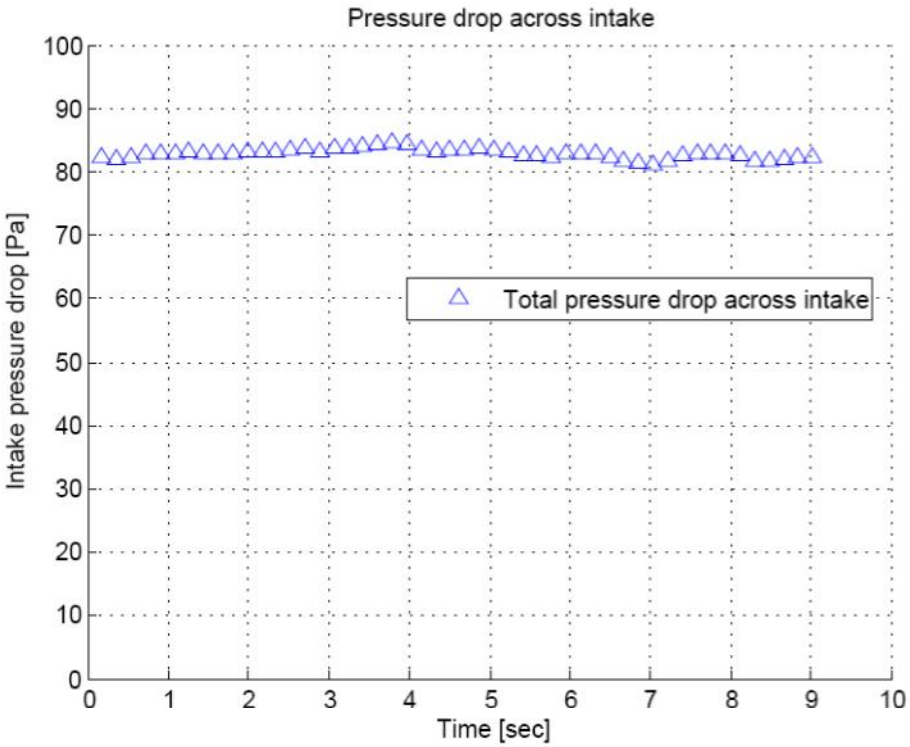

Figure A.3: Intake Pressure Drop vs. Time at 9500 rev/min

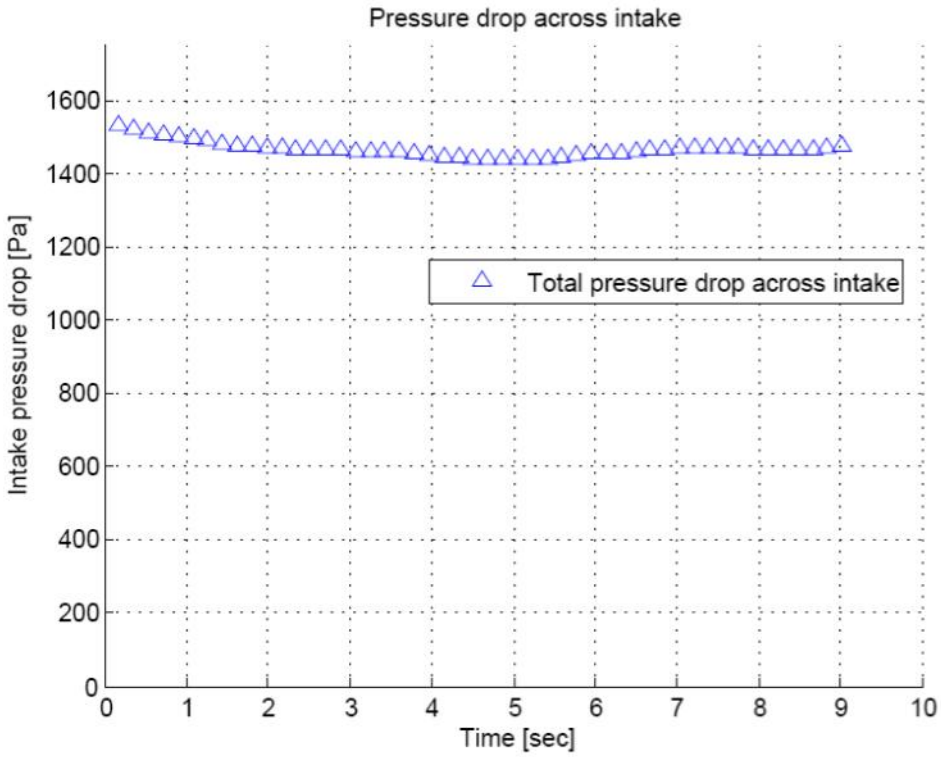

Figure A.4: Intake Pressure Drop vs. Time at 40000 rev/min

Figure A.5 shows a plot of the pressure drop across the intake vs. mass flow rate through the intake.

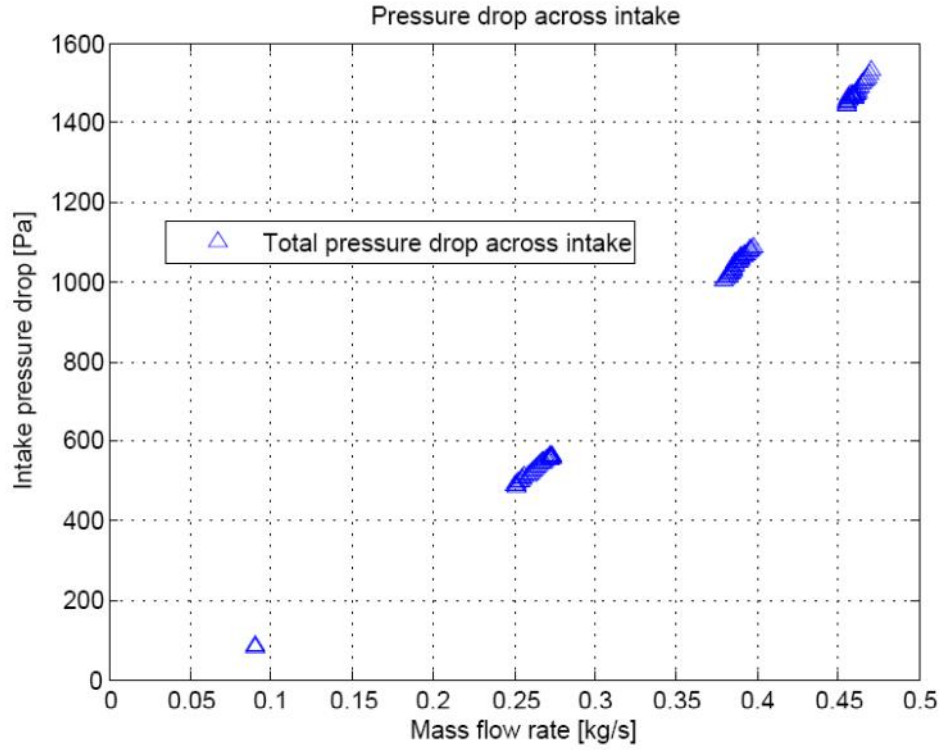

Figure A.5: Intake Pressure Drop vs. Mass Flow Rate

Compressor Efficiencies:

Results for the compressor efficiency and pressure ratio vs. non-dimensional mass flow rate can be seen in Figure A.6 and Figure A.7 which follow. Both graphs are in standard compressor map format with the *x*-axis being non-dimensional mass flow rate plotted against *y* axes of efficiency and pressure ratio respectively.

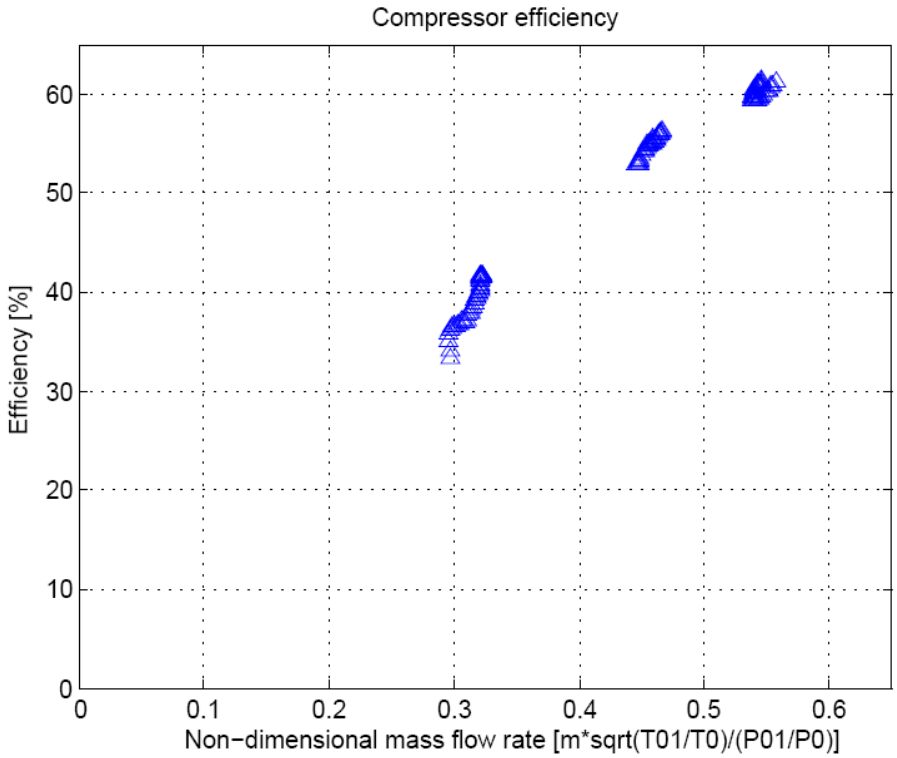

Figure A.6: Isentropic Efficiency vs. Non-dimensional Mass Flow Rate

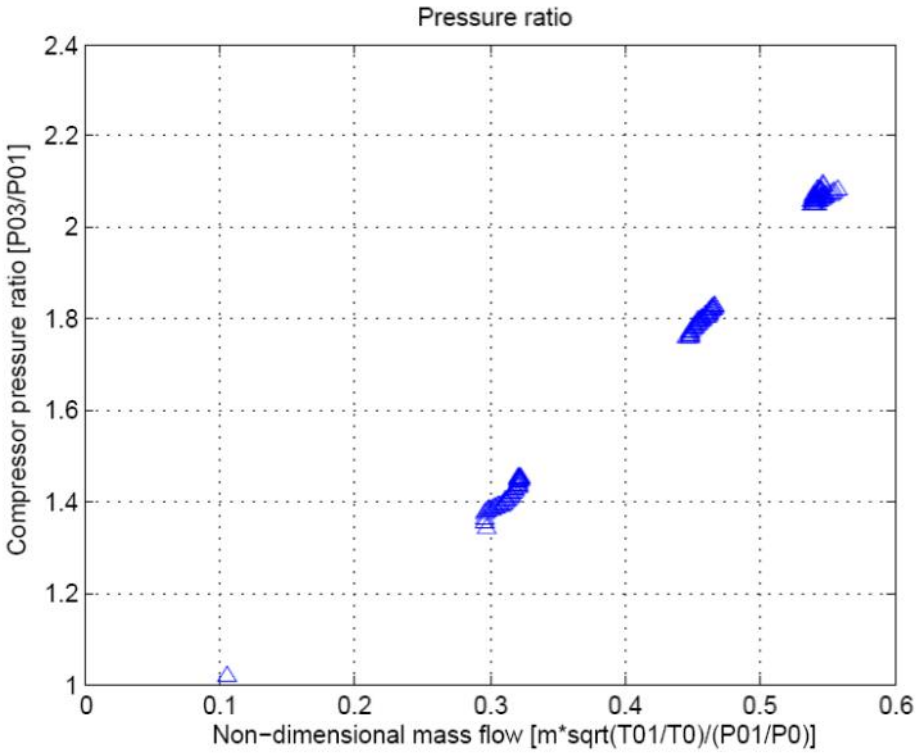

Figure A.7: Pressure Ratio vs. Non-dimensional Mass Flow Rate

Heat Exchanger Results:

The following four graphs show the pressure drop across the heat exchanger for both the hot cold and hot sides respectively, while Figure A.9 and Figure A.11 represent the percentage pressure drop across either side of the heat exchanger.

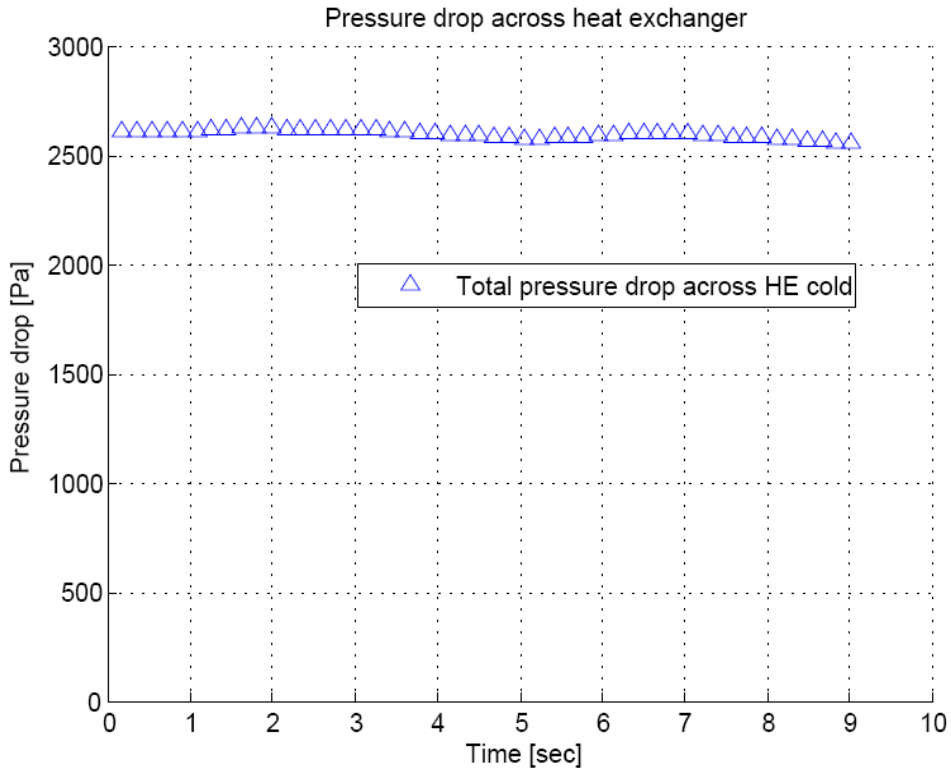

Figure A.8: Cold Side Pressure Drop vs. Time at 40000 rev/min

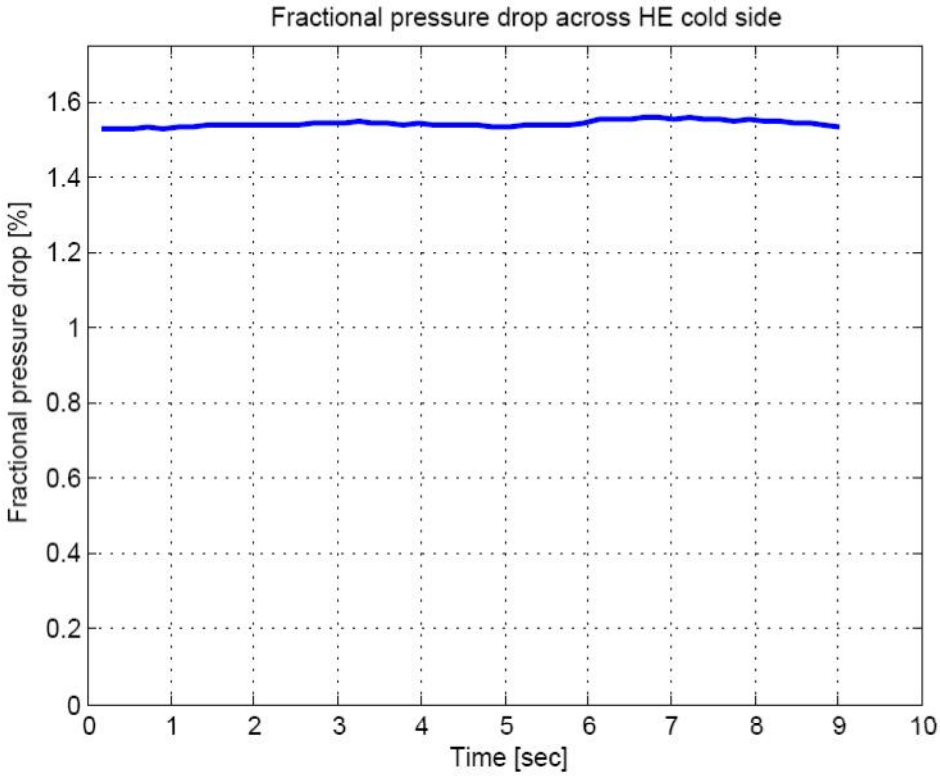

Figure A.9: Cold Side Percentage Pressure Drop vs. Time at 40000 rev/min

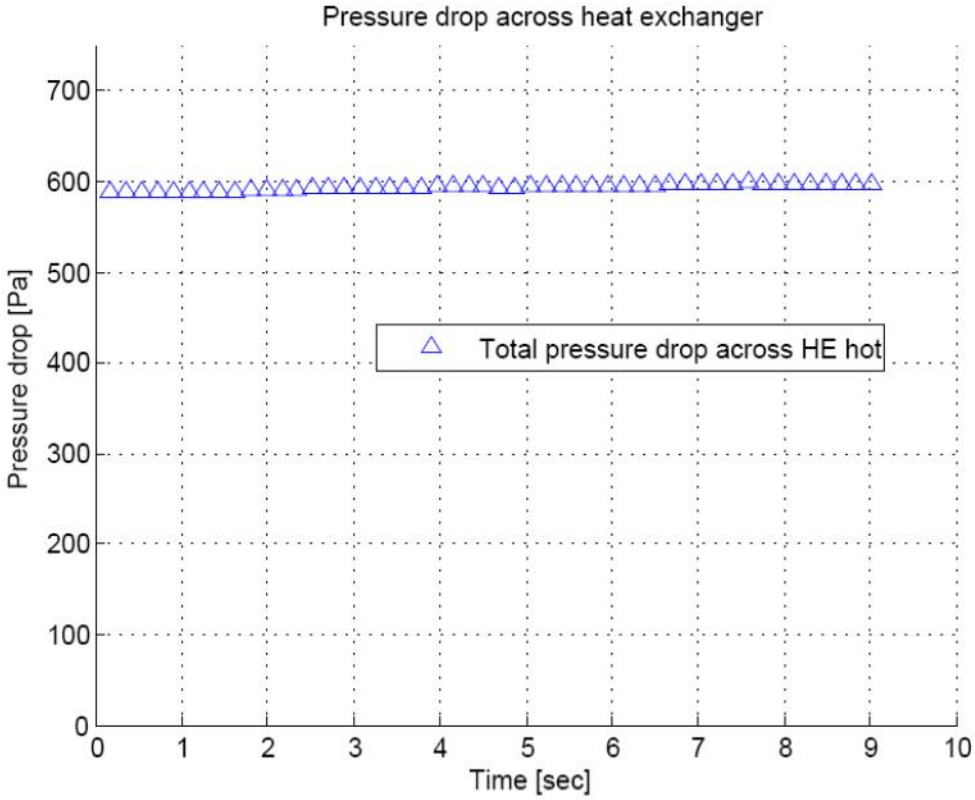

Figure A.10: Hot Side Pressure Drop vs. Time at 40000 rev/min

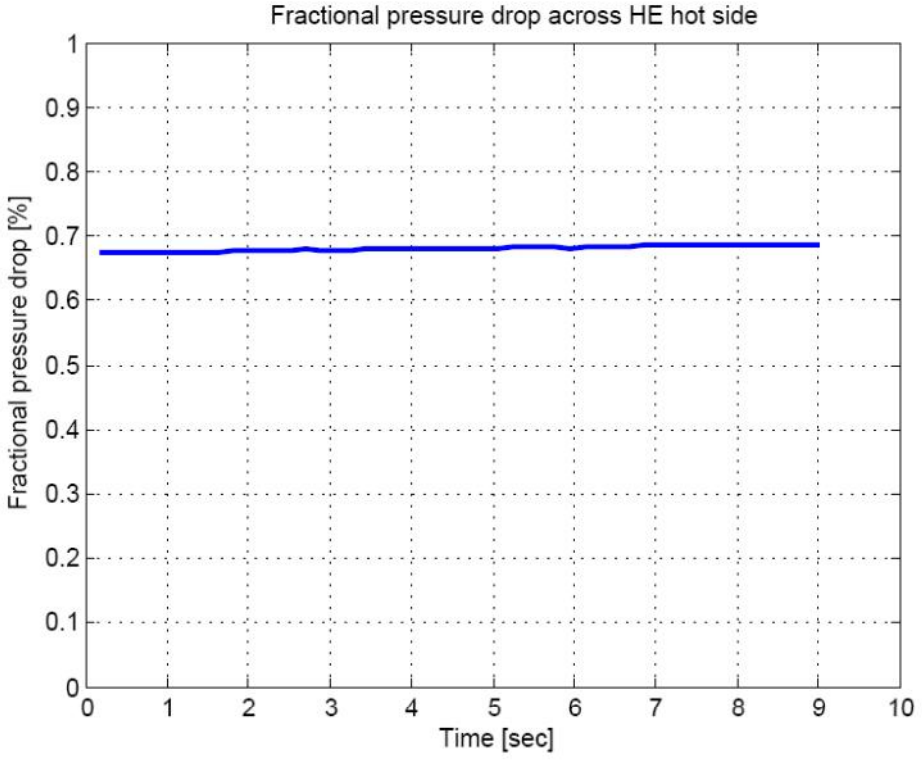

Figure A.11: Hot Side Percentage Pressure Drop vs. Time at 40000 rev/min

A plot was also produced which illustrated the heat exchanger effectiveness. This is shown in Figure A.12.

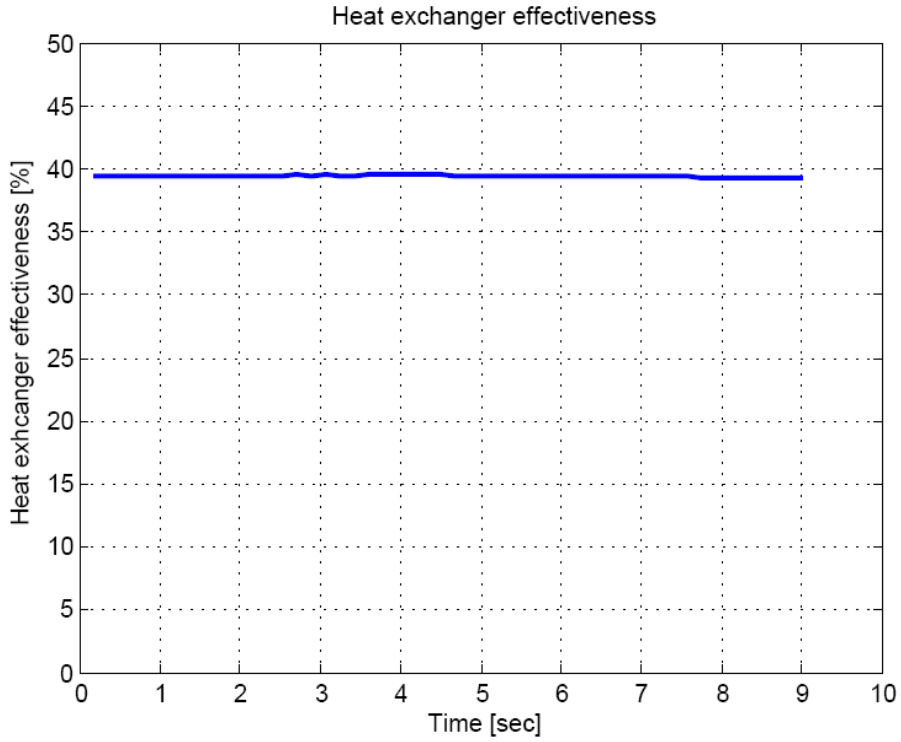

Figure A.12: Heat Exchanger Effectiveness at Stable Conditions (40000 rev/min)

Tests were run for as long as possible before fuel problems (discussed in Section 3.4) and overspeeding left the engine inoperable. Finally Figure A.13 shows all heat exchanger inlet and outlet temperatures for both hot and cold sides of the heat exchanger as well as the compressor's intake temperature at 40000 rev/min.

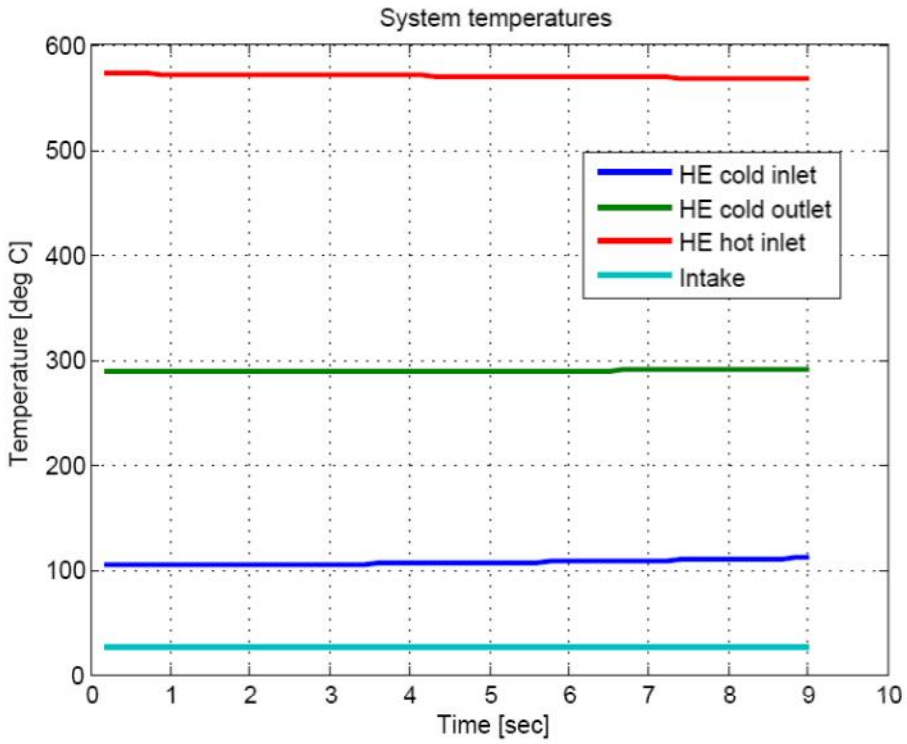

Figure A.13: System Temperatures at 40000 rev/min

Appendix B – Intake System Dimensions

Table B.1: Measurement Data Table for Intake Ducting System

MEASUREMENT DATA TABLE											
		Circular Properties		**Non-Circular Properties**							
		Inlet	**Exit**	**Inlet**		**Exit**					
Section	**Section Type**	**Diameter [mm]**	**Diameter [mm]**	**Base [mm]**	**Height [mm]**	**Base [mm]**	**Height [mm]**	**Elevation Angle [°]**	**Total Length [mm]**	**Mean Bend Radius [mm]**	**Bend Angle [°]**
1-2	Circular	110	110	-	-	-	-	0	147.5	-	-
2-3	Circular	110	201.5	-	-	-	-	+5	518	-	-
3-4	Mixed	201.5	-	-	-	166	201.5	0	207.5	-	-
4-5	Non-circular	-	-	166	201.5	83	201.5	0	Arclength (224.38)	142.85	90
5-6	Non-circular	-	-	83	201.5	166	201.5	+15.1	313.2	-	-
6-7	Non-circular	-	-	166	201.5	166	201.5	0	201.5	-	-
7-8	Non-circular	-	-	166	201.5	166	201.5	0	358.5	-	-
8-9	Non-circular	-	-	166	201.5	166	201.5	0	Arclength (316.75)	201.65	90
9-10	Non-circular	-	-	166	201.5	75	201.5	-18.48	180	-	-
Universal Wall Thickness: 0.9mm											
Universal Surface Roughness: 40μm											

Appendix C – Turbine Exit Diffuser Dimensions

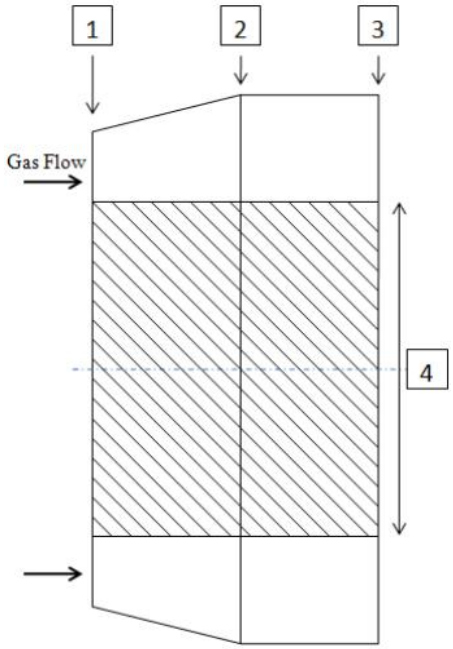

Figure C.1: Standard Exit Diffuser Geometry

Exit Diffuser Geometry (Standard)				
Geometry	Point 1	Point 2	Point 3	Point 4
Diam. [m]	0.1896	0.2162	0.2162	0.1520
Radius [m]	0.0948	0.1081	0.1081	0.0760
Area [m^2]	0.0101	0.0367	0.0367	0.0181
Length (Point 2 – Point 3): 0.06 m				

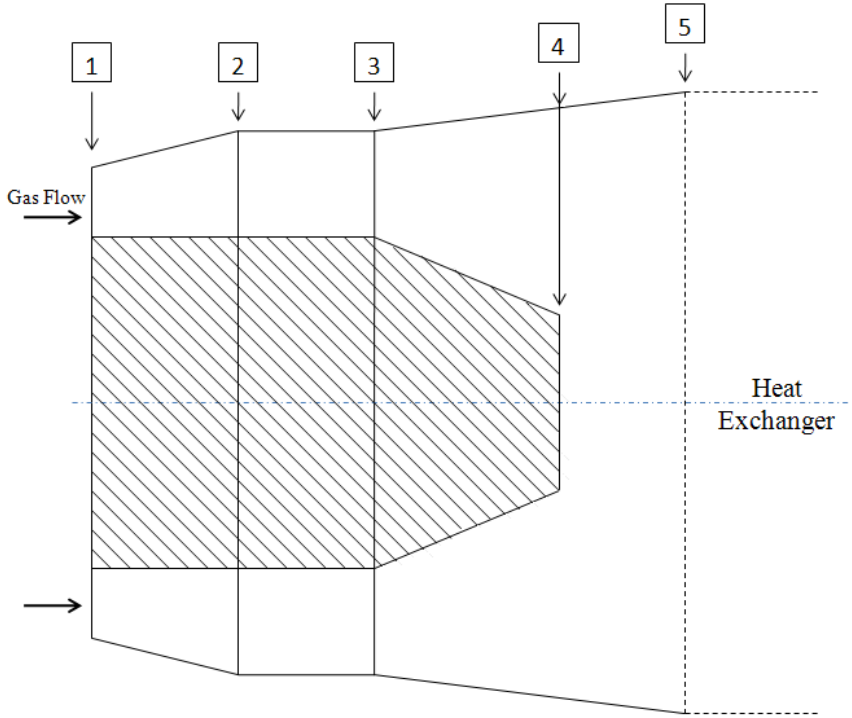

Figure C.2: Modified Exit Diffuser Geometry

Exit Diffuser Geometry (Modified)						
Geometry	Point 1	Point 2	Point 3	Point 4_o	Point 4_i	Point 5
Diam. [m]	0.1896	0.2162	0.2162	0.2592	0.076	0.29
Radius [m]	0.0948	0.1081	0.1081	0.1296	0.038	0.145
Area [m^2]	0.0101	0.0367	0.0367	0.0527	0.0045	0.0661

Appendix D – Heat Exchanger Dimensions

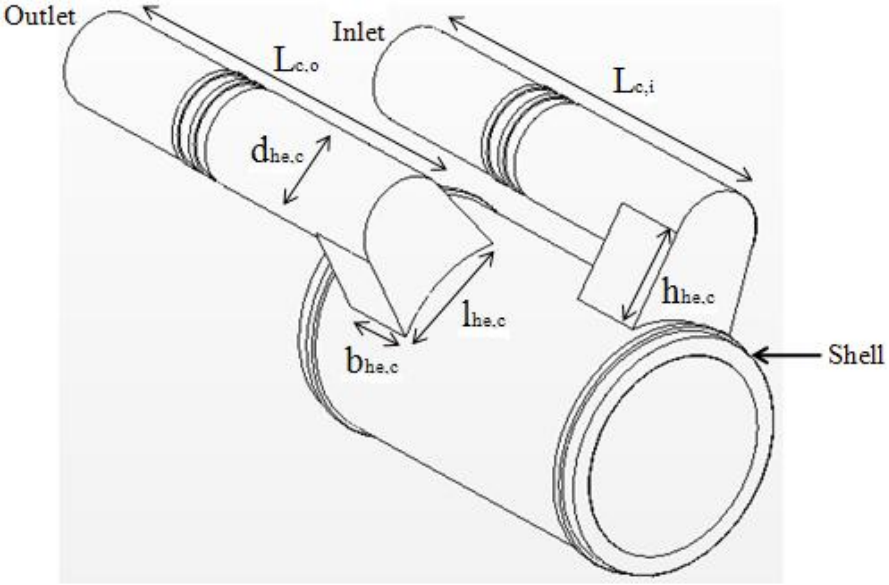

Figure D.1: Shell Side Geometry

Heat Exchanger Shell Side Geometry		
Geometry	Symbol	Value
Inlet Pipe Length [mm]	$L_{c,i}$	885
Outlet Pipe Length [mm]	$L_{c,o}$	832
General Pipe Diameter [mm]	$d_{he,c}$	128
Entrance Base [mm]	$b_{he,c}$	142
Entrance Length [mm]	$l_{he,c}$	150
Entrance Height [mm]	$h_{he,c}$	28

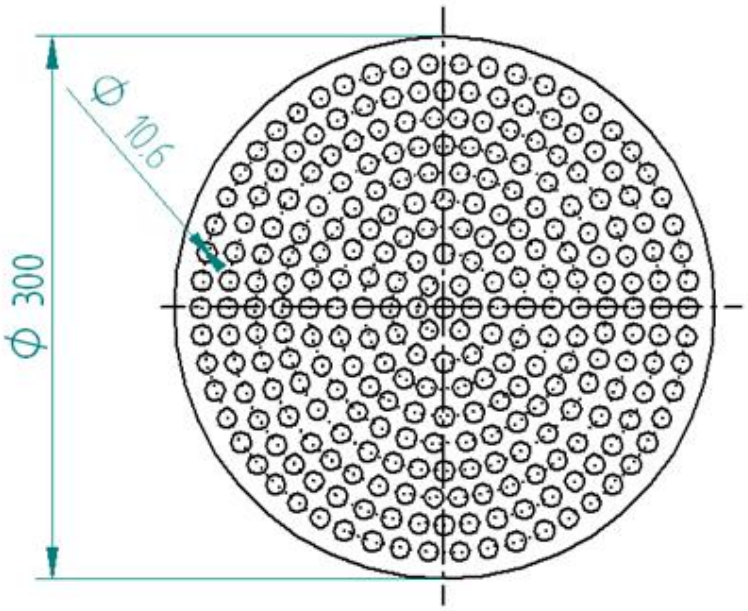

Figure D.2: Tube Bank Layout

Geometric Scaling Measurements	
Frontal Area (No Tubes) [m^2]	0.071
Total Tube Area [m^2]	0.024
Void Area [m^2]	0.047
Area Ratio	33.83 %
Percentage Free Area	66.17 %
Tube Density [No. Tubes/m^2]	3833.87
Mean line Spacing [mm]	10.2

Table D.1: Kays and London (1984) Tube Bank Properties

Kays and London (1984) Tube Bank Geometric Properties							
Tube set	**No. tubes**	**Tube ID** [m x 10^{-3}]	**Meanline Spacing** [m x 10^{-3}]	**Tube Area** [m x 10^{-5}]	**Local Area** [m^2 x 10^{-3}]	**Area Ratio**	**Density** [Tubes/m^2]
s1.5 – 1.25	13	9.525	13.88	7.125	3.175	29.18%	4094.5
s1.5 – 1.0	13	9.525	11.91	7.125	3.022	33.97%	3775.90
s2.0 – 1.0	13	9.525	13.47	7.125	3.266	28.36%	3980.4
i1.5 – 1.25	16	9.525	18.61	7.125	3.394	33.59%	4714.2
s1.25 – 1.25	18	9.525	13.31	7.125	3.652	35.12%	492 8.81
s1.5 – 1.5	18	9.525	10.1	7.125	4.718	27.19%	3815.18
s2.5 0.75	18	9.525	24.86	7.125	4.128	31.07%	4360.47
i1.25 – 1.25	16	9.525	16.85	7.125	3.002	37.98%	5329.78
s1.5 – 1.25(s)	13	9.525	12.4	7.125	1.935	47.87%	6718.35
i1.5 – 1.25(s)	20	9.525	12.4	7.125	2.419	58.91%	8267.88

Appendix E – Operating Point Estimates (Section 4.2)

Table E.1: Operating Point Estimates for Standard Rover 1S/60.

Station	P_o [kPa]	T_o[°C]	T [K]	Work [kW]
Ambient	87.6	20	293.15	
1	87.6	20	293.15	
2	245.28	162.4	435.55	74.02 (Comp.)
3	245.28	162.4	435.55	
4	230.32	756.85	1030	
5	230.32	756.85	1030	
6	89.35	572.53	845.68	111.24 (Turb.)

Table E.2: Operating Point Estimates for Modified Rover Engine.

Station	P_o [kPa]	T_o[°C]	T [K]	Work [kW]
Ambient	87.6	20	293.15	
1	87.6	20	293.15	
2	245.28	162.4	435.55	74.02 (Comp.)
3	245.28	162.4	435.55	
4	240.37	286.51	559.66	
5	240.37	286.51	559.66	
6	225.71	756.85	1030	
7	225.71	756.85	1030	
8	89.38	576.1	849.25	108.67 (Turb.)
9	89.38	576.1	849.25	
10	87.6	461.54	734.69	

Appendix F – Intake System Supplementary Results Tables

Table F.1: Filter Pressure Drop and High Re Number Pressure Drop with % Error

Mass Flow Rate [kg/s]	Pressure Drop [Pa] (For Filter)	Pressure Drop [Pa] (High Reynolds No.)	Percentage Error [%]
0.091	59.74	30.603	48.77
0.249	271.221	228.999	15.57
0.254	289.032	238.000	17.66
0.262	301.815	252.642	16.29
0.269	315.871	267.722	15.24
0.278	331.287	285.868	13.71
0.379	548.242	531.899	2.98
0.387	564.67	553.681	1.95
0.395	585.781	575.900	1.69
0.403	601.315	598.557	0.46
0.455	775.704	765.073	1.37
0.463	792.88	791.153	0.22
0.469	815.703	813.220	0.30
0.474	831.093	831.093	0.00

Table F.2: Intake System Data for the No Filter Flownex Model

Mass Flow Rate [kg/s]	Pressure Drop [Pa] (Measured)	Pressure Drop [Pa] (Flownex No Filter)	Pressure Drop [Pa] (For Filter)
0.091	87.179	27.439	59.74
0.249	466.667	195.446	271.221
0.254	492.308	203.276	289.032
0.262	517.949	216.134	301.815
0.269	543.589	227.718	315.871
0.278	574.359	243.072	331.287
0.379	1000	451.758	548.242
0.387	1035.897	471.227	564.67
0.395	1076.923	491.142	585.781
0.403	1112.821	511.506	601.315
0.455	1430.769	655.065	775.704

0.463	1471.795	678.915	792.88
0.469	1512.821	697.118	815.703
0.474	1543.59	712.497	831.093

Table F.3: Flownex Pressure Drop and Original Pressure Drop with % Error

Mass Flow Rate [kg/s]	**Pressure Drop [Pa] (Measured)**	**Pressure Drop [Pa] (Flownex k=19.83)**	**Percentage Error [%]**
0.091	87.179	58.54	32.85
0.249	466.667	427.33	8.43
0.254	492.308	444.6	9.69
0.262	517.949	472.96	8.69
0.269	543.589	498.5	8.29
0.278	574.359	532.35	7.31
0.379	1000	991.35	0.86
0.387	1035.897	1034.03	0.18
0.395	1076.923	1077.65	0.07
0.403	1112.821	1122.22	0.84
0.455	1430.769	1435.47	0.33
0.463	1471.795	1487.33	1.06
0.469	1512.821	1526.88	0.93
0.474	1543.59	1560.3	1.08

Appendix G – Turbine Efficiency Calculation – Cohen, et al (2001)

Known data:

Known data from Table 3.3 and Table 3.4.

Stator Opening (o) = 0.0076m Rotor Opening (o) = 0.005m

Inlet Stator Angle (α_1) = 0° Inlet Rotor Angle (β_2) = 14.06°

From velocity triangles seen in Figure G.1 the following parameters were found using an excel spreadsheet: V_2 = 451.3 m/s and V_3 = 482.2 m/s, T_{02} = 1030K, T_{03} = 948.2K.

Figure G.1 below provides a reference to understand the variable notation used in determining the theoretical isentropic efficiency of the turbine. All figures for Appendix G come from Cohen, et al (2001).

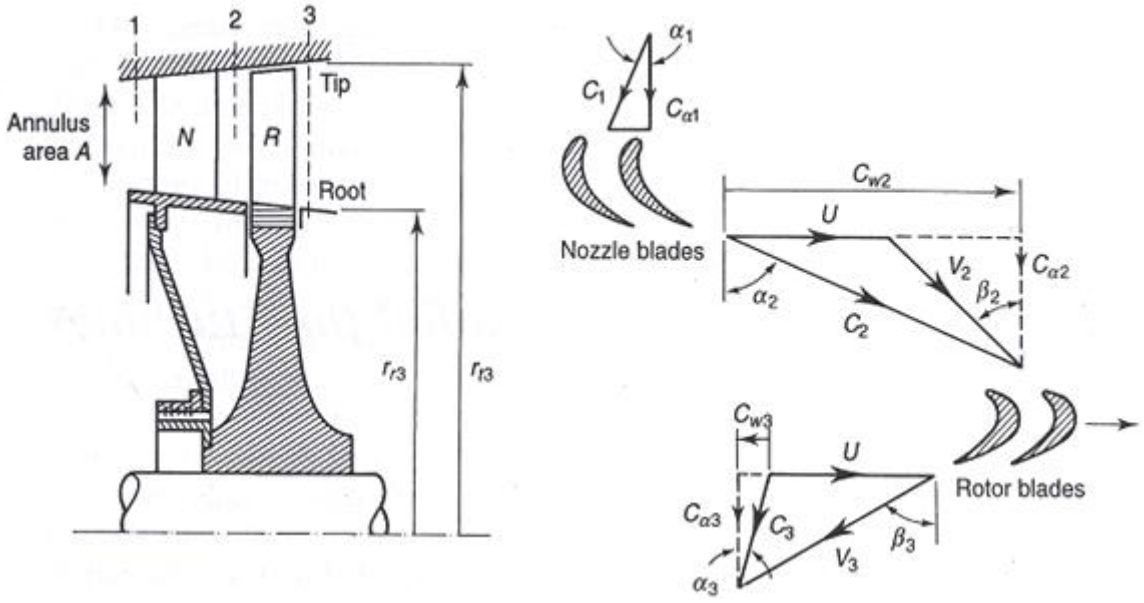

Figure G.1: Variable Reference for Turbine Blade Geometries

Step 1 – Estimating loss coefficients.

- Firstly, using the cosine rule, the outlet gas angles for the stator and the rotor were attained.
- Stator: $\cos^{-1}(o/s)$ = 72.03° Rotor: $\cos^{-1}(o/s)$ = 73.02°
- Using these angles with Figure G.2 and performing linear interpolation the inlet and exit gas angles for the rotor were determined, α_2 and β_3.

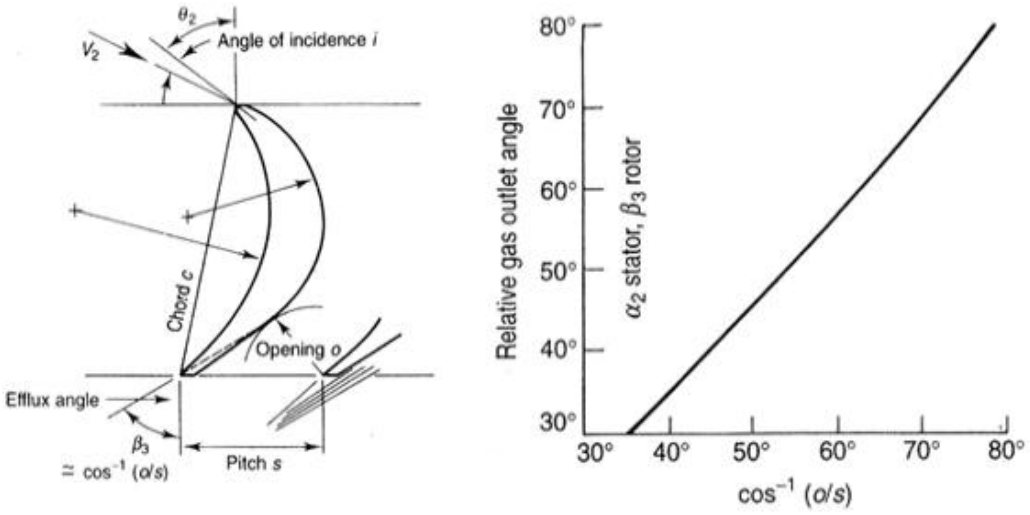

Figure G.2: Relative Gas Outlet Angles

- Stator (α_2): = 72.56° Rotor (β_3): = 73.69°
- These angles were then used with the profile loss coefficient curves seen in Figure G.3 in conjunction with the pitch to chord ratio calculated from Table 3.3 to attain the profile loss coefficients for the stator (blue) and rotor (red).

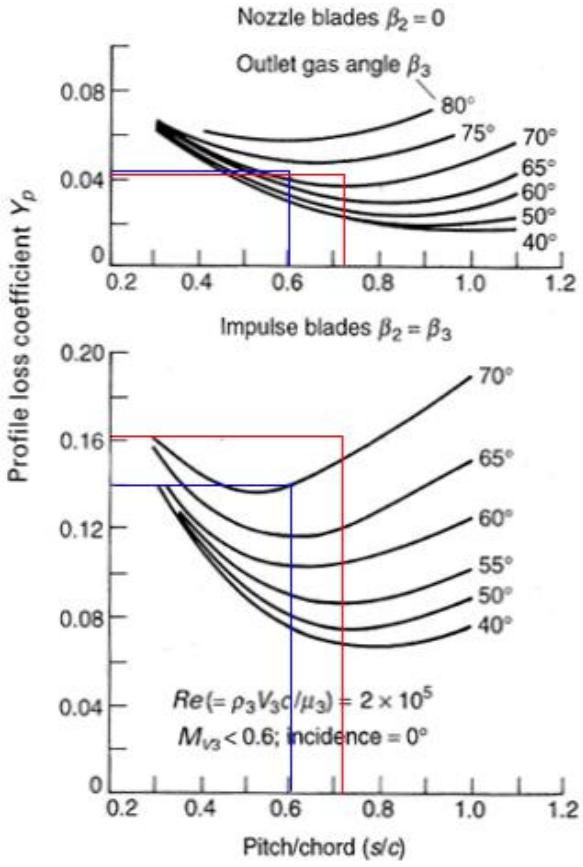

Figure G.3: Profile Loss Coefficient Curves

- Finally using equation (G.1) below the overall profile loss coefficients were found for the stator and rotor.

$$Y_p = \left\{Y_{p(\beta_2=0)} + \left(\frac{\beta_2}{\beta_3}\right)^2 \left[Y_{p(\beta_2=\beta_3)} - Y_{p(\beta_2=0)}\right]\right\}\left(\frac{t/c}{0.2}\right)^{\beta_2/\beta_3} \quad \text{(G.1)}$$

- $(Y_p)_S = 0.0405$ $(Y_p)_R = 0.0308$

Step 2 – Finding secondary (Y_s) and tip (Y_k) clearance losses.

- The secondary and tip losses are given equation (G.2).

$$Y_s + Y_k = \left[\lambda + B\left(\frac{k}{h}\right)\right]\left[\frac{C_L}{s/c}\right]\left[\frac{cos^2\beta_3}{cos^3\beta_m}\right] \quad \text{(G.2)}$$

- Firstly a coefficient of lift was calculated from equation (G.3)

$$C_L = 2(s/c)(tan\beta_2 + tan\beta_3)cos\beta_m \quad \text{(G.3)}$$

Where:

$$\beta_m = tan^{-1}[(tan\beta_3 - tan\beta_2)/2] \quad \text{(G.4)}$$

- Stator: β_m [rad] = 0.996, Rotor: β_m [rad] = 1.061.
- Stator: $C_L = 2.022$, Rotor: $C_L = 2.55$.
- B is taken as 0.25 for a shrouded edge and 0.5 for un-shrouded edge, hence $B_{stator} = 0$ and $B_{Rotor} = 0.5$.
- k refers to the tip clearance, and h is the mean blade height, see Table 3.4.
- Finally in order to calculate λ, equation (G.5) was used in conjunction with Figure G.4.

$$\lambda = f\left\{\frac{\left(\frac{A_3 cos\beta_3}{A_2 cos\beta_2}\right)^2}{\left(1+\frac{r_r}{r_t}\right)}\right\} \quad \text{(G.5)}$$

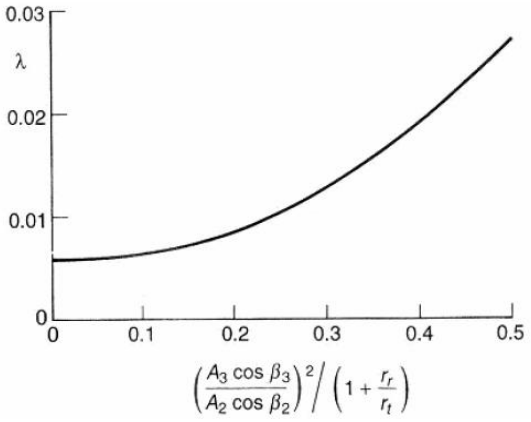

Figure G.4: Secondary Loss Parameter

- Where r_r/r_t refers to the root to tip diameter ratio and A_3 and A_2 refer to the annular area at the inlet and exit of the blade row.
- This then yielded $[Y_S + Y_K]_S = 0.0462$ and $[Y_S + Y_K]_R = 0.2033$.

Step 3 – Calculating the total loss coefficients.

- Here the total loss coefficients are calculated by adding the loss coefficients from step 1 to the secondary and tip loss coefficients of step 2. See equation G.6 and G.7.

$$Y_s = \left[\left(Y_p\right)_S + \left(Y_s + Y_k\right)_s\right] cf \tag{G.6}$$

$$Y_R = \left[\left(Y_p\right)_R + \left(Y_s + Y_k\right)_R\right] cf \tag{G.7}$$

- As seen from the equations a correction factor is required. The correction factor only plays a role if the ratio of trailing edge thickness/blade pitch differs from 0.02. This is illustrated in Figure G.5.

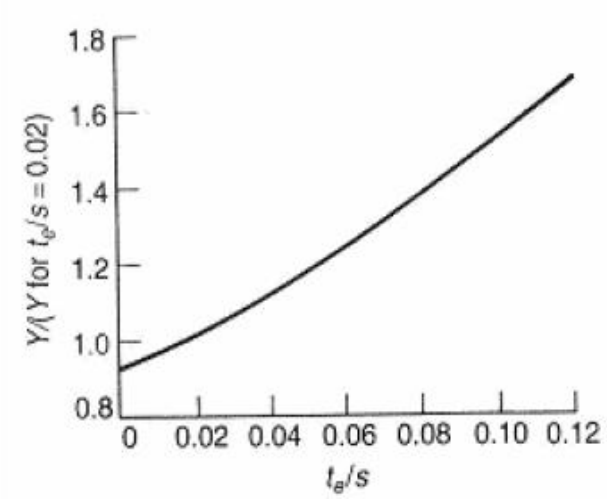

Figure G.5: Correction Factor for Trailing Edge Thickness

- Once multiplied by the correction factor the overall loss coefficients were found. $Y_S = 0.090$ and $Y_R = 0.090$

Step 4 – Calculating the stage efficiencies.

- The final step involves calculating the stage efficiencies. See equation (G.8) which follows.

$$\eta_s = \frac{1}{\left\{\frac{\left[\left(\lambda_R\left(\frac{V_3{}^2}{2C_p}\right)\right)+\left(\frac{T_3}{T_{02}}\right)\lambda_S\left(\frac{V_2{}^2}{2C_p}\right)\right]}{(T_{01}-T_{03})}\right\}} \quad \text{(G.8)}$$

λ_N and λ_R are defined as follows:

$$\lambda_S = \frac{Y_S}{T_{02}/T_2{}'}$$

$$\lambda_R = \frac{Y_R}{T_{03}/T_3{}''}$$

Where all subscripts are defined as they are in Cohen, et al (2001).

This yields a stage efficiency of 85.7 % for the turbine.

Appendix H – TPERF and TDML Program Data

TPERF		
DATA Inputs		
	Value	**Unit**
Preliminary Study	Yes	1
Loss Correlation	Small	0
Exit Diffuser	Yes	1
Plain Clearance	Yes	1
Single Stage	Yes	1
Speed Lines	1-8	
Gas Constant	287	J/kgK
Inlet Temperature	1023.15	K
Inlet Pressure	280	kPa
Mach No. tolerance	0.001	

Station 1 - Turbine Inlet		
Parameter	**Value**	**Notes**
Hub Radius (mm)	76	
Tip Radius (mm)	88.1	
Cp (J/kgK)	1148	
Inlet Flow Angle (°)	0	

Station 2 - Blade row 1 - Stator		
Parameter	**Value**	**Notes**
Hub Radius (mm)	76	
Tip Radius (mm)	88.7	
Cp (J/kgK)	1148	
Inlet Blade Angle (°)	0	
Outlet Flow Angle (°)	72.21	
Trailing Edge Thickness (mm)	0.8	
Tip Clearance (mm)	0	
Spacing at Mean (mm)	24.6	
Additional Loss Factor	0	

Station 3 - Blade row 2 - Rotor		
Parameter	**Value**	**Notes**
Hub Radius (mm)	76	
Tip Radius (mm)	94.3	
Cp (J/kgK)	1148	
Inlet Blade Angle (°)	25.857	
Outlet Flow Angle (°)	-73.02	
Trailing Edge Thickness (mm)	0.8	
Tip Clearance (mm)	0.5	
Spacing at Mean (mm)	17.3	
Additional Loss Factor	0	

Turbine Exit		
Parameter	**Value**	**Notes**
Hub Radius of Diffuser (mm)	76	
Tip Radius of Diffuser (mm)	108.1	
Diffuser Loss Co-Eff.	0.4	

Data For Speed Line		
Parameter	**Value**	**Notes**
First Stator exit Mach No. (Initial)	0.1	
First Stator exit Mach No. (Final)	1	
Mach No. Increment	0.042	
Range of Pressure Ratios (Choke)	0	
Max. Allowable total Pressure ratio	0	
Rotational Speed (rpm)	0-50000	

Figure H.1: Input Data for TPERF Program

TDML		
DATA Inputs		
	Value	**Unit**
Turbine inlet configuration	Neither	0
Turbine outlet configuration	Diffuser	1
Loss correlation	small	0
Plain Clearance	Yes	1
Number of stages	-	1
Speed Lines	1-8	
Gas Constant	287	J/kgK
Inlet Temperature	1023.1	K
Inlet Pressure	280	kPa
Mass Flow Rate	0.603	kg/s
Inlet swirl velocity	0	m/s
Critical reynolds number	5.05E+05	
Rotor metal density	8000	kg/m3

Station 1 - Turbine Inlet		
Parameter	**Value**	**Notes**
Hub Radius (mm)	76	
Tip Radius (mm)	88.1	
Cp (J/kgK)	1148	
Viscosity (Ns/m2)	3.74E-05	

Blade row 1 - Stator		
Parameter	**Value**	**Notes**
Number of blades	21	
Trailing Edge Thickness (mm)	0.8	
Swirl Velocity (m/s)	395	
Tip Clearance (mm)	0	

Station 2 - Rotor		
Parameter	**Value**	**Notes**
Hub Radius (mm)	76	
Tip Radius (mm)	88.7	
Cp (J/kgK)	1148	
Viscosity (Ns/m2)	3.74E-05	

Blade row 2 - Rotor		
Parameter	**Value**	**Notes**
Number of blades	31	
Stage Power required (kW)	83	
Rotor Rotational speed (RPM)	47000	
Trailing Edge Thickness (mm)	0.8	
Rotor hub to tip area ratio	1.5	
Tip Clearance (mm)	0.5	

Station 3		
Parameter	**Value**	**Notes**
Hub Radius (mm)	76	
Tip Radius (mm)	94.3	
Cp (J/kgK)	1148	
Viscosity (Ns/m2)	3.74E-05	

Exit configuration - Diffuser		
Parameter	**Value**	**Notes**
Hub Radius of Diffuser (mm)	77	
Tip Radius of Diffuser (mm)	108.1	
Effectiveness of exit Diffuser	0.4	

Figure H.2: Input Data for TDML Program

Appendix I – Compressor Maps

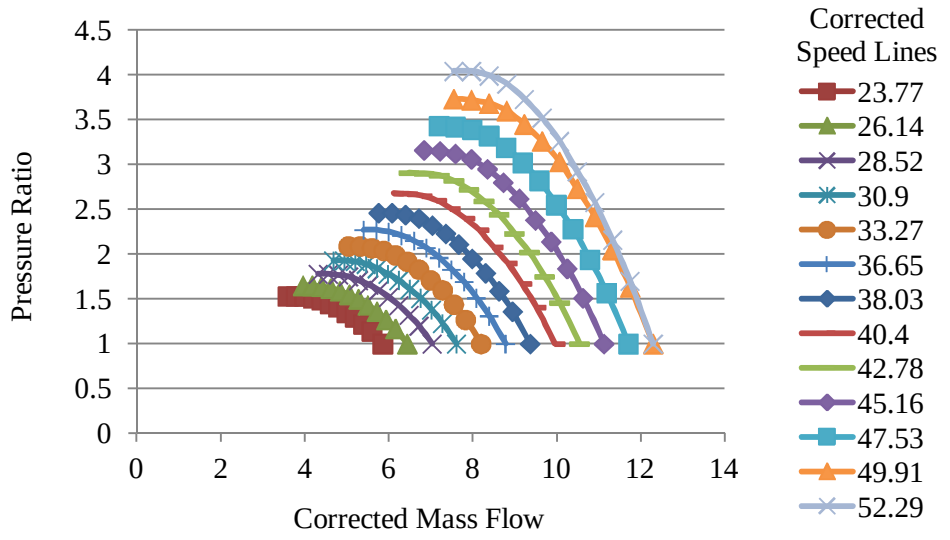

Figure I.1: Corrected Mass Flow Vs. Pressure Ratio

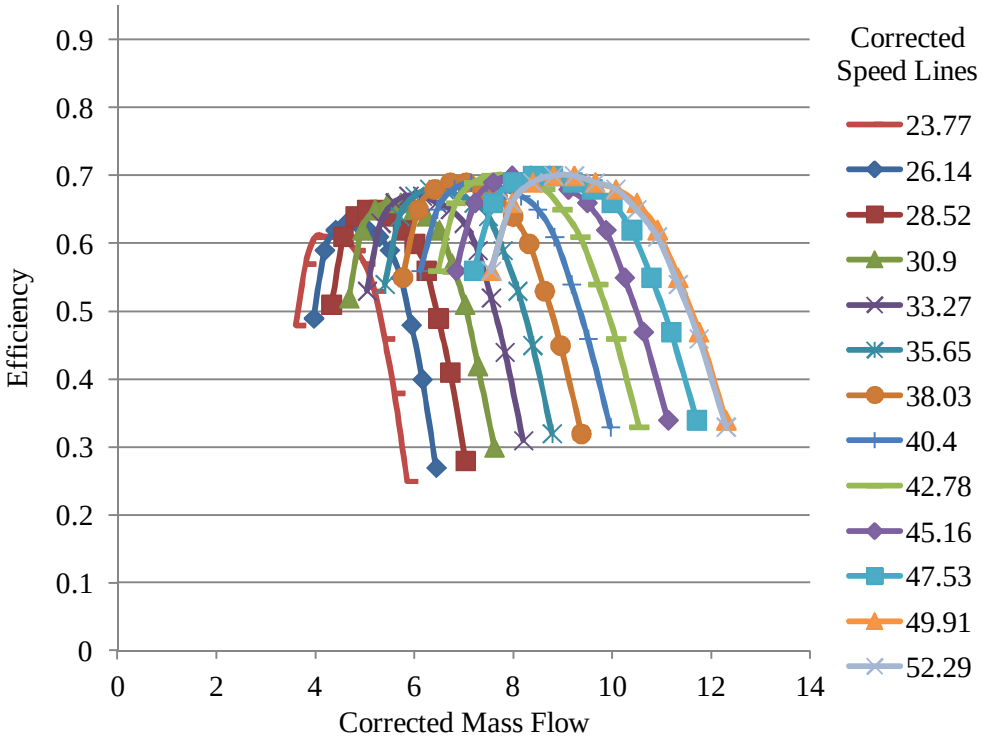

Figure I.2: Corrected Mass Flow Vs. Efficiency

Appendix J – Heat Exchanger NTU Calculations

Known data:

$\dot{m}_{cold}$ = 0.518 kg/s	Cp_{cold} = 1017 J/kgK	D_{tube} = 0.0105 m
$\dot{m}_{hot}$ = 0.518 kg/s	Cp_{hot} = 1047 J/kgK	N = 271
k_g = 5.51 x 10^{-2} W/mK	k_a = 4.10 x 10^{-2} W/mK	k_{steel} = 43 W/mK
Cold side:	T_{in} = ± 432.15 K	T_{out} = ± 533 K
Hot side:	T_{in} = ± 850 K	T_{out} = ± 720 K
μ_{Gas} = 337 x 10^{-7} Ns/m^2	μ_{Air} = 243.284 x 10^{-7} Ns/m^2	
Pr_{Air} = 0.6835	Pr_{Gas} = 0.716	

Assumptions:

Negligible heat loss to surroundings.

Constant properties.

Fully developed flow for both air and the exhaust gas.

Using formulae and methodologies from Incropera and DeWitt (2002) the following analysis was performed and results attained.

Schematic:

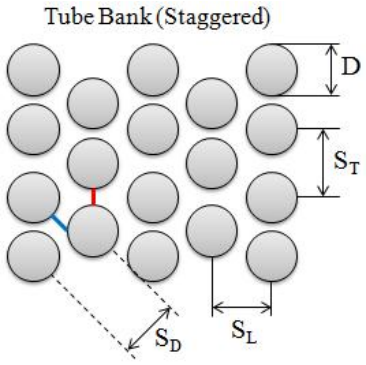

Step 1 – Finding C_{min} and C_{max}:

$C_{cold} = \dot{m}_{cold} \times Cp_{cold}$ = 526.80 J/sK ≈ C_{min}

$C_{hot} = \dot{m}_{hot} \times Cp_{hot} = 542.35$ J/sK ≈ C_{max}

Step 2 – Attaining C:

$C = C_{min} / C_{max} = 0.97135$

Step 3 – Finding heat transfer area:

$A = \Pi \times D \times L \times N = \Pi \times 0.0105 \times 0.5 \times 271 = 4.4697$ m^2

Step 4 – Getting overall heat transfer co-efficient:

$$U = \frac{1}{\frac{1}{h_i} + \frac{r_o \ln\left(r_o / r_i\right)}{k} + \frac{1}{h_o}}$$

Calculating the heat transfer coefficient for internal flow within the tubes:

$$\mathrm{Re}_i = \frac{4\dot{m}}{\pi D \mu} = 1846307.83$$

Therefore using the Dittus Boelter correlation for turbulent internal flow in pipes:

$$Nu_i = 0.023 \times \mathrm{Re}_i^{0.8} \times \mathrm{Pr}^{0.4} = 2073.65$$

Thus: $h_i = \frac{Nu_i k_g}{D_i} = 10881.75$ W/m^{2}K

Calculating the heat transfer coefficient for external flow over tube banks:

$$Re_{D_{max}} = \frac{\rho D V_{max}}{\mu}$$

Where: $V_{max} = \frac{S_T}{2(S_D - D)} \times V$ and $V = \frac{\dot{m}}{\rho A}$

Hence from the Schematic:

$V_{max} = 5.42$ m/s

Thus:

$Re_{D_{max}} = 1983.15$

The Nusselt number correlation from Incopera and DeWitt (2002) for 10 or more rows in a tube bundle:

$$Nu_D = C_1 Re_{D,max}^m$$

Obtaining C_1 and m from Table 7.5, Incopera and DeWitt (2002):

C_1 = 0.518 and m = 0.556

This leads to a Nusselt number:

Nu_D = 35.29

Thus calculating the heat transfer coefficient:

$$h_o = Nu_D \frac{k}{D}$$

h_o = 115.625 W/m^{2}K

Finally this yields an Overall heat transfer coefficient U = 114.225 W/m^{2}K

Step 5 – Calculating number transfer units (NTU):

$$NTU = \frac{A \times U}{C_{\min}} = 0.969$$

Step 6 – Calculating the effectiveness and heat transfer:

$$\varepsilon = 2\left\{\left(1 + C + \sqrt{1+C^2}\right) \times \frac{1+\exp\left(-NTU\sqrt{1+C^2}\right)}{1-\exp\left(-NTU\sqrt{1+C^2}\right)}\right\}^{-1} = 0.3497 = 34.97\ \%$$

$$q_{\max} = C_{\min}(T_{h,i} - T_{c,i}) = 220.12 \text{ kW}$$

Thus $q = q_{\max} \times \varepsilon$ = 76.99 kW

Appendix K – Thermal Storage Heat Transfer Coefficient

Known data:

$\dot{m}_{air}$ = 0.518 kg/s D_{Drum} = 0.25 m D_{Pebble} = 0.019 m

Number of Pebbbles = 100 (1 Layer) Number of Pebbbles = 3000 (Total)

ΔT = 475 °C, μ_{pebble} = 415.2 Ns/m^2 x 10^{-7}

Table A.4: (Incopera and DeWitt, 2002): Air (T_∞ = 573K): μ = 296.404 Ns/m^2 x 10^{-7}, υ = 48.8452 x 10^{-6} m^2/s, ρ = 0.60875 kg/m^3, k = 0.04528 W/mK, Pr_{Air} = 0.6835, μ_s = 181.1 Ns/m^2 x 10^{-7}.

Assumptions:

Negligible heat loss to surroundings.

Constant properties.

Step 1 – Finding air velocity through pebble gaps:

$$V = \frac{\dot{m}}{\rho A} = 2.316 \text{ m/s}$$

Where A represents the actual air flow cross sectional area for 1 layer of pebbles.

Step 2 – Finding Re for a single pebble:

$$\text{Re} = \frac{\rho V D}{\mu} = 1338.98 \text{ (Laminar)}$$

Where D represents the diameter of a single pebble.

Step 3 – Calculating the Nusselt number from Wakao and Kaguei (1982) correlations for packed beds:

$$Nu = 2 + 1.1 \text{Pr}^{0.3} \text{Re}^{0.6} = 75.76$$

Step 4 – Calculating the heat transfer coefficient for conduction:

$$h_{pebble} = \frac{Nu\mu}{D} = 0.157 \text{ W/m}^2\text{K} \qquad h_{Layer} = \frac{Nu\mu}{D} = 15.73 \text{ W/m}^2\text{K}$$

$$q = h_{pebble} A_{total} \Delta T = 70.42 \text{ kW}$$

Step 5 – Calculating the heat transfer coefficient for convection:

$$h_{Air} = Nu_D \frac{k}{D_{pebble}}$$

Where: (From, flow over sphere, Incopera and DeWitt, 2002):

$$Nu_D = 2 + \left(0.4Re_D^{1/2} + 0.06Re_D^{2/3}\right) Pr^{0.4} \left(\frac{\mu}{\mu_s}\right)^{1/4}$$

Nu_D= 69.44

Thus:

h_{Air}= 165.49 W/m^{2}K

Appendix L – Klein (2011) - Thermal Storage Graphs

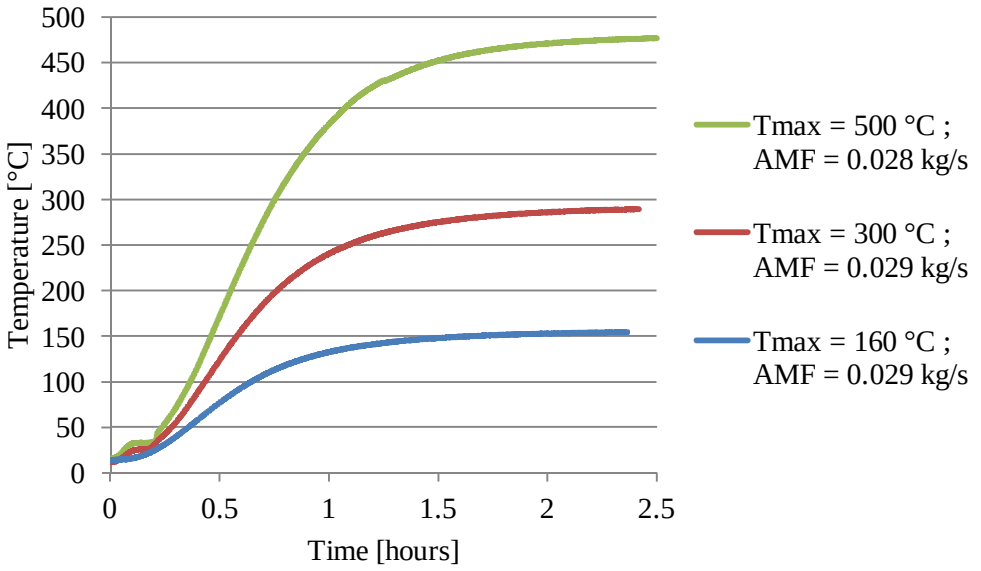

Figure L.1: Thermal Storage Heating, Pebble Temperature Vs. Time

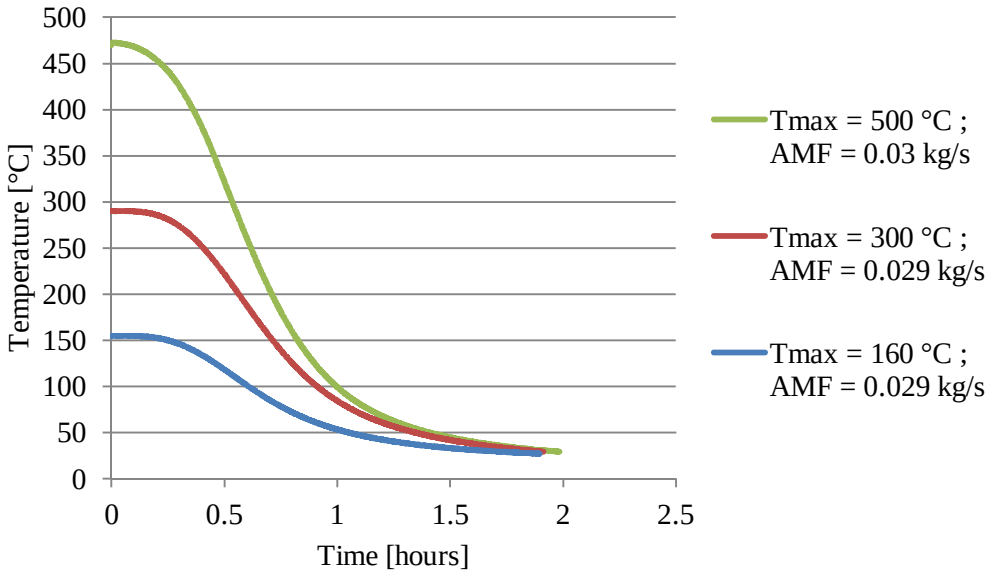

Figure L.2: Thermal Storage Cooling, Pebble Temperature Vs. Time

Appendix M – Model Reusability

In order for the model to be reusable to model other systems of this type certain parameters would need to be changed by the user. These are outlined and discussed below. From a network structure perspective few changes are required as the basic operation of the Brayton cycle remains the same for systems of this type. It must be noted that this model applies only to gas turbine cycles or Brayton cycles.

1. The user will need the Flownex SE software package in order to open the each of the respective models (Standard, Modified and Solar) available on the attached CD.
2. Once opened the following needs to be clearly specified with regard to the boundary conditions within the system.
    i. Pressure and temperature boundary conditions must be specified at all inlet exit points to the system.
    ii. Fuel conditions on the fuel flow rate boundary condition must be specified.
3. Next each of the system specific components must be defined; this includes the compressor, heat exchanger, turbine and piping components).
    i. The compressor and turbine maps which describe the gas turbine that the user wants to model must be imported into Flownex using each of the respective map editors. The maps need to be in the correct format as required by Flownex, outlined in Section 4.2.3.
    ii. For the heat exchanger / recuperator component the correct orientation must be chosen from the options available. Following this specific geometries and materials pertaining to the heat exchanger must be entered so that the effectiveness and other parameters can be calculated by the software.
    iii. All piping components, valves and filters must have exact geometries specified. This may involve adding additional piping components should the current ones in the model not be sufficient.
4. Finally the solar heat input (in the case of the solar model) needs to be specified as well as the shaft RPM in the case of a steady state simulation at design point.
5. Run the simulation and refer to the interface tab to monitor results such as pressure, temperature, mass flow rate, system power and system efficiency.